Measurement of the Neutron Magnetic Form Factor from Inclusive Quasielastic Scattering of Polarized Electrons from Polarized ^{3}He

Thesis by
Haiyan Gao

In Partial Fulfillment of the Requirements
for the Degree of
Doctor of Philosophy

California Institute of Technology
Pasadena, California

1994
(May 16, 1994)

Acknowledgements

Many people have contributed significantly to this experiment. I would like to take this opportunity to thank them all for their enthusiasm and efforts in carrying out this experiment. Several of them deserve special mention.

The co-spokespersons of this experiment, Bob McKeown and Richard Milner, provided necessary leadership and many creative ideas. I am especially indebted to my advisor Bob McKeown for giving me this opportunity to work on the polarized ^{3}He experiment from which I enjoyed a great deal both the physics involved and polarizing the ^{3}He atoms. I thank him for all the support, advice, and encouragement I have received from him during my stay at Caltech. He has been patient and wise. It has been a pleasure to have such a great mentor whose physics intuition and wisdom are always fascinating. This work would never have been possible without his insight and guidance.

I have had the pleasure of working with Wolfgang Lorenzon, who was the first person I met in Kellogg, working in front of a computer with laser goggles on in the dark room 100. I learned a lot from him both in hardware and software. I thank him for making the NMR calibration of the optical measurement of ^{3}He nuclear polarization possible. Tom Gentile has contributed tremendously to this experiment. I thank him for developing the reliable LNA laser system for the ^{3}He target, significant efforts in carrying out the NMR calibration, and numerous discussions, sage advice, and help on the target. He has taught me valuable lessons of being an experimentalist, and being neat in the lab, though I think I failed in that part of the lesson

of being neat in the lab by his standard. I also thank him for reviewing Chapter 3 of this thesis and many comments and suggestions. Betsy Beise has been a mentor all these years whose encouragement and advice keep me going all the time. I have learned a lot from her both as a physicist and as a person. I would like to thank her for her continuous interest and efforts in this work. Without her expertise on Q and many other aspects of this experiment, the analysis would take a lot longer. I thank her for making me believe that measuring G_M^n is also interesting in the first place. Cathleen Jones has never been hesitant to answer all the questions I have on the target, to share with me her experience from the previous ^{3}He experiment, and has always been there listening with a smile to my frustrations of working on the target. She has helped in many ways to make this experiment a success. Especially, I thank her for reviewing the manuscript of this thesis and many helpful comments and suggestions. Bob Carr has always been helpful whether it was in Kellogg or at Bates. In particular, I thank him for teaching me how to drive on a snowy road at Bates.

Mark Pitt deserves recognition for his efforts in making the Wien filter work for this experiment. I would also like to thank him for all his work on the B-line Møller measurements and the analysis of the beam polarization data. I would like to thank Brad Filippone, Allison Lung, and John Arrington for their work and efforts in improving the beam polarization measurement, Manouch Farkhondeh, George Dodson, and Wolfgang Korsch for their hard work in providing the polarized electrons, Dan Tieger, Karen Dow, Pat Welch, Leird Kramer, and Bryon Mueller for their assistance in realizing this experiment, and Kevin Lee for his help working on the laser and watching the target during the experiment.

I would also like to acknowledge Ole Hansen for his contributions on many aspects of the experiment, in particular for setting up the Pockels cell for the laser polarizing optics, preparing the bright dip acid for me, and for making the whole experiment work. Chris Tripp and Bogdan Wojtsekhowski have worked very hard in getting the MEPS spectrometer ready for the experiment and their contributions are greatly

acknowledged. I would like to thank Andrea Dvoredsky for analyzing the beam polarization data.

I would like to take this opportunity to thank Dr. Giovanni Salmè and Ralf-Wolfgang Schulze for providing their calculations, helpful discussions, and their patience with me.

I thank the staff of the Bates Linear Accelerator Center for their significant efforts in realizing this experiment. I acknowledge all the technical assistance I have received from Jim Pendley, Jack Richards, and Al Massey. I also thank Pat Huber for his computer resources. I would like to thank all the members of the Kellogg family for making me feel at home.

I would like to thank my friends Wen, Mei, Zhen, Yu, Guang, Bing, Delilah and Bao-lin for their friendships and encouragement all these years. I would also like to thank my fellow student Bryon Mueller for being a friend right from the beginning, and my office-mates, former and present, for their endurance and kindness.

Finally, I would like to thank my parents for their support and love through my life, for introducing physics to me ever since I was a little girl, my husband Jianzhong for his love, support, and understanding, my in-laws for their support, and my son Calvin for adding colors and new dimensions to my life.

Abstract

The results of a measurement of the spin-dependent asymmetry in quasielastic scattering of longitudinally polarized electron from polarized ^{3}He target are reported. The neutron magnetic form factor at $Q^2 = 0.19$ (GeV/c)^2 has been extracted from the measured asymmetry and is reported in this thesis work. The experiment was performed at the MIT-Bates Linear Accelerator Center with an incident electron beam energy of 370 MeV. Two magnetic spectrometers, MEPS and OHIPS, were used to detect the scattered electrons independently, with MEPS at the kinematics maximally sensitive to the spin-dependent transverse response function, $R_{T'}$, at $Q^2 = 0.19$ (GeV/c)^2 and OHIPS at the kinematics maximally sensitive to the spin-dependent transverse-longitudinal response function, $R_{TL'}$, at $Q^2 = 0.14$ (GeV/c)^2. The elastic asymmetry and the quasielastic asymmetry $A_{TL'}$ in the threshold region for three-body breakup have also been measured in OHIPS and reported. A cryogenic polarized ^{3}He gas target using a metastability-exchange optical pumping technique was employed in this experiment. The target was operated at 13K during the experiment with an average target thickness of 3.3×10^{18}cm^{-2} (MEPS) and 1.6×10^{19}cm^{-2} (OHIPS). The average target polarization with 25 μA average beam current was over 38%. A GaAs source produced the polarized electrons and a Wien spin rotator was employed to rotate the spin to give longitudinally polarized electrons at the ^{3}He target. The average beam polarization for the experiment was 36.5%.

The measured ^{3}He elastic asymmetry agrees very well with the calculated val-

ues using the ^{3}He form factors measured by Rosenbluth separation. The measured spin-dependent transverse asymmetry, $A_{T'}$, which is expected to be sensitive to the neutron magnetic form factor is in good agreement with recent PWIA calculations using a spin-dependent spectral function. The neutron magnetic form factor at $Q^2 = 0.19$ (GeV/c)^2 has been extracted from the measured asymmetry based on the recent PWIA calculations. The extracted G_M^n value agrees very well with the standard dipole parametrization at this Q^2. This experiment represents the first measurement of the neutron magnetic form factor using spin-dependent electron scattering. The uncertainty of the extracted ${G_M^n}^2$ is dominated by the statistical uncertainty and the uncertainty due to model dependence is found to be comparatively small. The measured $A_{TL'}$ in the threshold region has shown very large positive asymmetry close to the three-body breakup threshold. To interpret the $A_{TL'}$ data, a complete calculation of the ^{3}He asymmetry $A_{TL'}$ in the elastic-threshold region using a spin-dependent spectral function with final state interactions (FSI) and meson exchange currents (MEC) taken into account is probably necessary.

Contents

List of Figures

List of Tables

Chapter 1

Physics Motivation

1.1 Introduction

Electromagnetic form factors are of fundamental importance for an understanding of the underlying structure of nucleons. Knowledge of the distribution of charge and magnetization within the nucleons provides a sensitive test of models based on QCD, as well as a basis for calculations of processes involving the electromagnetic interactions with complex nuclei. Due to the lack of a free neutron target, the neutron electromagnetic form factors are known with less precision than the proton electric and magnetic form factors. They have been deduced in the past from elastic or quasielastic electron-deuteron scattering. This procedure involves considerable model dependence. The development of polarized targets and beams has allowed more complete studies of electromagnetic structure than has been possible with unpolarized reactions. In quasielastic scattering, the spin degrees of freedom introduce new response functions into the inclusive cross section, thus providing additional information on nuclear structure [1].

^{3}He is an interesting nucleus for polarization studies because its ground state wave functions is predominantly a spatially symmetric S state in which the spin of the nucleus is carried mainly by the unpaired neutron. Therefore, inelastic scatter-

ing of polarized electrons from polarized ^{3}He in the vicinity of the quasielastic peak should be useful for studying the neutron electromagnetic form factors. This idea was first investigated by Blankleider and Woloshyn within the closure approximation [2]. Friar *et al.* [3] have studied the model dependence in the spin structure of the ^{3}He ground state wave function and its effect on the quasielastic asymmetry. Recently the plane wave impulse approximation (PWIA) calculations performed independently by two groups [4,5] using a spin-dependent spectral function show that the spin-dependent asymmetry is very sensitive to the neutron electric or magnetic form factors at certain kinematics near the top of the quasielastic peak. Two previous experiments [6,7] measured the spin-dependent asymmetry in quasielastic scattering of polarized electrons from polarized ^{3}He, and demonstrated that this new experimental procedure is feasible for studying the neutron electromagnetic structure. As a result, new experimental programs utilizing polarized electrons and polarized ^{3}He targets to study the neutron electromagnetic structure and the nucleon spin structure are under way at several electron accelerator laboratories (SLAC, MIT-Bates, CEBAF, MAMI, DESY HERA).

This thesis reports the measurement of the transverse asymmetry, $A_{T'}$, in spin-dependent quasielastic scattering of longitudinally polarized electrons from a polarized ^{3}He target. The experiment was performed at the MIT-Bates linear accelerator center in the spring of 1993. Five institutes, Argonne, Caltech, MIT, RPI, and TRIUMF, collaborated on this experiment. The neutron magnetic form factor at $Q^2 = 0.19$ (GeV/c)^2 has been extracted from the measured asymmetry based on recent PWIA calculations using a spin-dependent spectral function. For this measurement, the uncertainty in the extracted neutron magnetic form factor is dominated by the statistical error and the systematic uncertainty is mainly from the uncertainties in the determination of the beam and target polarizations. The uncertainty from model dependence has been studied carefully using various proton electromagnetic form factor parametrizations and different ^{3}He wave functions and is found to be comparatively small. The work presented here is the first measurement of the

neutron magnetic form factor using spin-dependent electron scattering.

The remainder of this chapter contains a discussion of the existing data on G_M^n in the low Q^2 region from the electron-deuteron scattering experiments, recent PWIA calculations for the ^{3}He quasielastic asymmetry using a spin-dependent spectral function, and extraction of the neutron magnetic form factor from the ^{3}He quasielastic asymmetry. In the second chapter, we discuss the experimental apparatus. In the third chapter, we describe the polarized ^{3}He target employed in this work as it was a very important part of this thesis work. The data analysis is described in Chapter 4 and a discussion of the systematic uncertainties in the asymmetry measurement is given in Chapter 5. In Chapter 6, the asymmetry results are presented and the neutron magnetic form factor determined from the measured asymmetry. Lastly, in Chapter 7 the conclusions are given.

1.2 Existing Data

Due to the lack of a free neutron target, all previous data on the neutron magnetic form factors are almost exclusively from either elastic or quasielastic electron-deuteron scattering experiments. Here only the data in the low Q^2 region will be discussed as they are relevant to the present work. The electron-deuteron data can be further divided into the following three main categories: the inclusive, coincidence, and the anti-coincidence measurements. The standard dipole parametrization [8] of the nucleon electromagnetic form factors gives

$$\frac{G_M^n}{\mu_n} = \frac{G_M^p}{\mu_p} = G_E^p = G_D = \left[1 + \frac{Q^2}{0.71}\right]^{-2}, \tag{1.1}$$

where Q^2 is in $(\mathrm{GeV/c})^2$. Fig. 1.1 shows the world data of ${G_M^n}^2$, in units of $\mu_n {G_D}^2$, in the low Q^2 region including the recent Bates [9], NIKHEF [10], and the Bonn [11] measurements. Except for the recent Bates, NIKHEF, and Bonn data, all the previous data have large error bars $(20-30\%)$. In general, the existing world's data

set is internally inconsistent, as successive measurements at the same value of Q^2 disagree outside of the error bars. The error bars associated with each measurement are interesting and it is worthwhile to discuss them individually.

The work of Hughes *et al.* [12] (shown as hollow squares with error bars due only to the statistical uncertainties and a global 5% theoretical uncertainty), the reanalyzed data of Grossetête *et al.* [14] by Kramer *et al.* [13] (shown as hollow diamonds with error bars essentially just due to the statistical uncertainties), all used inclusive measurements of quasielastic scattering of electrons from deuterium where the proton cross-section is subtracted from the deuteron cross-section to extract the neutron form factors, except for part of the data from Hughes *et al.* where the measurements of the ratio of the total quasielastic electron-deuteron cross-section to the elastic electron-proton cross-section were taken and the neutron form factors were extracted from the data using the "area method" [12].

The subtraction technique which involves a separation of the longitudinal and the transverse cross section (Rosenbluth separation) to yield the magnetic contribution first, and further subtraction of the dominant proton magnetic contribution is questionable. There is the well-known "blow-up" of experimental error bars for the small contribution, which for low Q^2 is the magnetic one, associated with the Rosenbluth separation, and also the enhancement of the systematic error on the extracted G_M^n arising from subtraction of the proton contribution. There are also considerable theoretical uncertainties from the final state interactions (FSI), meson exchange currents (MEC), and the deuteron wave function associated with this experimental technique.

In fact, Hughes *et al.* extracted negative values of ${G_E^n}^2$. No additional error was added to the extracted G_M^n due to this extraction of a nonphysical values of ${G_E^n}^2$, nor was any error due to the FSI or N-N potential taken into account. Braess *et al.* [13] have reanalyzed the measurements of Hughes *et al.* [12] at momentum transfers below 5 fm^{-2} by including a realistic description of the deuteron structure and the effect of interactions between the outgoing nucleons (shown as asterisks with

error bars due to both the systematic and statistical uncertainties). Their extracted values of the neutron magnetic form factors come out still larger than but closer to the values predicted by the dipole parametrization as compared to the former analysis. However, their analysis also yields negative values for ${G_E^n}^2$.

It was noted by Hanson *et al.* [15] that the measurements from Hughes *et al.* [12] of the ratios of the neutron to proton cross-sections decrease more rapidly than the other measurements, as the scattering angle θ goes to zero, which leads to the extraction of the negative values of ${G_E^n}^2$ mentioned previously.

Budnitz *et al.* [16] (shown as hollow circles with the error bars being the statistical uncertainties only) and Hanson *et al.* [15] (shown as crosses with the statistical error bars), both used the "anti-coincidence" technique where one attempts to detect (e,e'p) and if the proton is not detected (i.e., d(e,e'$\bar{p}$)), the scattered electron is associated with scattering from a neutron. The idea is that if a proton is not observed at the correct kinematics calculated from ω and $\vec{q}$, assuming no recoil, then the scattering is from a neutron. This method relies on the detailed knowledge of the deuteron wave function and detector efficiencies to understand all the processes by which a proton might not have been detected. Budnitz *et al.* [16] have varied the electron-proton cross-section by $\pm 5\%$ to examine the systematic uncertainty on the extracted neutron magnetic form factor and the uncertainty was found to be of the same size as the statistical uncertainty of their measurements.

The work of Stein *et al.* [18] (shown as hollow triangle with statistical error bar), and Bartel *et al.* [17] (shown as hollow stars with essentially statistical error bars), both used the coincidence method of d(e,e'n), although they relied on measuring protons and taking the ratio of the proton to neutron cross sections. The advantage of an electron-neutron coincidence measurement is that it eliminates the large quasifree scattering contribution from the proton. The main difficulty associated with this method is obtaining an absolute calibration of the neutron detector efficiency. The extracted value of G_M^n depends on the deuteron wave function assumed and on MEC depending on whether the top or the full quasielastic peak is used. The

two coincidence measurements mentioned above determined the neutron detection efficiency by the associated particle technique with the reaction $\gamma + p \rightarrow \pi^+ + n$.

The recent Bates data by Markowitz *et al.* [9] (shown as the solid diamonds with the inner (outer) error bars being the statistical and the (total) uncertainties) again used the coincidence method of d(e,e'n). The neutron detection efficiency was determined using the associated particle technique with the ^{2}H(γ, pn) reaction. The total uncertainties of the extracted G_M^n were determined by the quadrature sum of the statistical, systematic, and the theoretical uncertainties.

The recent NIKHEF experiment by Jourdan *et al.* [10] (shown as a solid triangle with the total error bar determined by the quadrature sum of the experimental and theoretical uncertainties) measured the ratio of the $d(e, e'n)$ cross-section to that of $d(e, e'p)$ (ratio method). The absolute neutron detection efficiency was determined with high accuracy using the tagged neutrons produced by $H(n, p)n$ scattering of a high intensity neutron beam. The total uncertainty from this measurement is much smaller than all other G_M^n measurements in the low Q^2 region, though the data point lies much lower compared with the rest of the data in the same Q^2 region.

The recent Bonn data [11] (shown as a hollow star with the total error bar) also used the ratio method to extract the neutron magnetic form factor. The neutron detection efficiency was determined by the associated particle method using the $p(\gamma, \pi^+ n)$ reaction. This measurement shows marginal agreement with the recent Bates measurement, given the size of the uncertainties in the two measurements. The Gari-Krümpelmann [20] and Höhler [19] form factor parametrizations are also shown in Fig. 1.1.

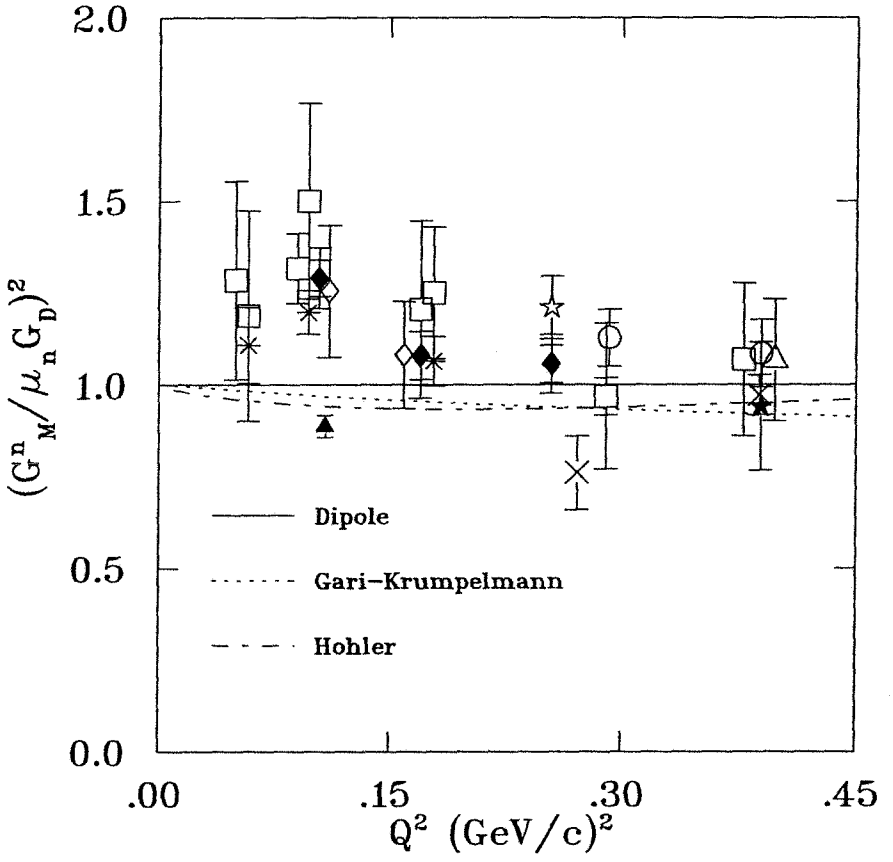

Figure 1.1: The square of the neutron magnetic form factor ${G_M^n}^2$, in units of the standard dipole parametrization, $(\mu_n G_D)^2$, in the low Q^2 region. The hollow squares are from Hughes *et al.* [12], the hollow diamonds are from the analysis by Kramer *et al.* [13] of the data from Grossetête *et al.* [14], the asterisks are from Braess *et al.* [13], the crosses are from Hanson *et al.* [15], the hollow circles are from Budnitz *et al.* [16], the solid star is from Bartel *et al.* [17], the hollow triangle is from Stein *et al.* [18], the solid diamonds are from Markowitz *et al.* [9] with the inner (outer) error bars being the statistical (total) uncertainties, the solid triangle is the NIKHEF data [10], and the hollow star is the Bonn data [11]. The data of Markowitz *et al.*, Hughes *et al.*, and Stein *et al.* have been displaced slightly to improve readability.

1.3 Calculations of the ^{3}He Quasielastic Asymmetry

The PWIA calculation of the spin-dependent asymmetry for longitudinally polarized electrons scattering quasielastically from a polarized ^{3}He nucleus was first performed about 10 years ago by Blankleider and Woloshyn [2] within the closure approximation, where a spin-dependent momentum distribution was employed to describe the nuclear effects. It was only recently that the calculation of the spin-dependent ^{3}He quasielastic asymmetry using a spin-dependent spectral function became available [4] [5]. In this section, we will describe the formalism developed by Schulze *et al.* [5] for calculating the ^{3}He quasielastic spin-dependent asymmetry using a spin-dependent spectral function.

1.3.1 The Nuclear Current Tensor

The nuclear current tensor $W_A^{\mu\nu}(q, P_A)$ of a spin-$\frac{1}{2}$ nuclear target A with mass M_A, four-momentum P_A, and polarization n_A, is required for the description of the inclusive processes. The current tensor is Hermitian and conserved. It preserves parity, gauge, and time-reversal invariance and its Lorentz structure is built from the three four-vectors q, P_A, and n_A which satisfy $P_A^2 = M_A^2$, $n_A^2 = -1$, and $(P_A \cdot n_A) = 0$. The current tensor has the general form

$$\begin{aligned} < n_A \mid W_A^{\mu\nu}(q, P_A) \mid n_A > \; = \; & -\left[\frac{q^\mu q^\nu}{Q^2} + g^{\mu\nu}\right] W_1^A \; + \; \tilde{P}_A^\mu \tilde{P}_A^\nu \frac{W_2^A}{M_A^2} \; + \\ & i\epsilon^{\mu\nu\alpha\beta} q_\alpha \left[n_{A\beta} \frac{G_1^A}{M_A} \; + \; [(q \cdot P_A) n_{A\beta} \right. \\ & \left. -(q \cdot n_A) P_{a\beta}] \frac{G_2^A}{M_A^3} \right], \end{aligned} \tag{1.2}$$

$$\tilde{P}_A \; = \; P_A \; + \; \frac{q \cdot P_A}{Q^2} q, \tag{1.3}$$

where $q = (q^0,\ \mathbf{q})$ is the four-momentum transferred from the electron to the target nucleus ($Q^2 = -q^2$ being positive), $g^{\mu\nu}$ is the metric tensor with $g^{00} = -g^{11} = -g^{22} = -g^{33} = 1$, and $\epsilon^{\mu\nu\alpha\beta}$ is the total antisymmetric tensor in four dimensions. W_1^A and W_2^A are the spin-averaged structure functions, and G_1^A and G_2^A are the spin structure functions. The structure functions are real-valued Lorentz scalars and therefore depend on the scalars Q^2 and $(q \cdot P_A)$.

By exploiting the identity $\epsilon_{\mu\nu\alpha\beta}\epsilon^{\mu\nu\gamma\rho} = -2(g_\alpha^\gamma g_\beta^\rho - g_\alpha^\rho g_\beta^\gamma)$, the structure functions can be obtained from a given current tensor by contraction with other tensors as follows:

$$W_1^A(Q^2, q\cdot P_A/M_A) \;=\; \frac{1}{2}\left[\frac{\tilde{P}_{A\mu}\tilde{P}_{A\nu}}{\tilde{P}_A^2} \;-\; g_{\mu\nu}\right] \;<\; n_A \mid\; W_A^{\mu\nu}(q,P_A) \;\mid n_A \;> \qquad (1.4)$$

$$W_2^A(Q^2, q\cdot P_A/M_A) \;=\; \frac{1}{2}\frac{M_A^2}{\tilde{P}_A^2}\left[3\frac{\tilde{P}_{A\mu}\tilde{P}_{A\nu}}{\tilde{P}_A^2} \;-\; g_{\mu\nu}\right] \;<\; n_A \mid\; W_A^{\mu\nu}(q,P_A) \;\mid n_A \;> \qquad (1.5)$$

$$\begin{aligned} G_1^A(Q^2, q\cdot P_A/M_A) \;=\; & -\frac{i}{2}\frac{M_A}{q\cdot n_A}\left[(q\cdot n_A)P_A^2 q^\alpha n_A^\beta - (q\cdot P_A)q^\alpha P_A^\beta\right] \\ & \times\frac{\epsilon_{\mu\nu\alpha\beta} < n_A \mid W_A^{\mu\nu}(q,P_A) \mid n_A >}{P_A^2\,(-Q^2 + (q\cdot n_A)^2) - (q\cdot P_A)^2} \end{aligned} \qquad (1.6)$$

$$\begin{aligned} G_2^A(Q^2, q\cdot P_A/M_A) \;=\; & -\frac{i}{2}\frac{M_A^3}{Q^2\,(q\cdot N_A)}\left\{(q\cdot n_A)(q\cdot P_A)q^\alpha n_A^\beta + \left[Q^2 - (q\cdot n_A)^2\right] q^\alpha P_A^\beta\right\} \\ & \times\frac{\epsilon_{\mu\nu\alpha\beta} < n_A \mid W_A^{\mu\nu}(q,P_A) \mid n_A >}{P_A^2\,(-Q^2 + (q\cdot n_A)^2) - (q\cdot P_A)^2} \end{aligned} \qquad (1.7)$$

Choosing the nuclear center-of-mass (c.m.) frame without loss of generality, the three four-vectors which build up the Lorentz structure of the nuclear current tensor become: $P_A = (M_A, 0)$, $n_A = (0, n_A^1, 0, n_A^3)$, and $q = (q^0, 0, 0, |\mathbf{q}|)$. The c.m. frame is defined by the following three unit vectors: $\hat{\mathbf{e}}_3 = \hat{\mathbf{q}}$, $\hat{\mathbf{e}}_2 = (\hat{\mathbf{e}}_3 \times \hat{\mathbf{n}}_A)/\mid \hat{\mathbf{e}}_3 \times \hat{\mathbf{n}}_A \mid$, and $\hat{\mathbf{e}}_1 = \hat{\mathbf{e}}_2 \times \hat{\mathbf{e}}_3$. In that nuclear c.m. system the structure functions of Eqs. 1.4 - 1.7

take the particular forms

$$W_1^A(Q^2, q\cdot P_A/M_A) = \frac{1}{2} \ < n_A \mid W_A^{11}(q,P_A) + W_A^{22}(q,P_A) \mid n_A \ >, \tag{1.8}$$

$$\begin{aligned} W_2^A(Q^2, q\cdot P_A/M_A) \ &= \ \frac{Q^4}{\mathbf{q}^4} \ < n_A \mid W_A^{00}(q,P_A) \mid n_A \ > + \\ &\frac{1}{2}\frac{Q^2}{\mathbf{q}^2} \ < n_A \mid W_A^{11}(q,P_A) + W_A^{22}(q,P_A) \mid n_A \ >, \end{aligned} \tag{1.9}$$

$$\begin{aligned} G_1^A(Q^2, q\cdot P_A/M_A) \ &= \ \frac{i}{2}\frac{M_A^2}{\mathbf{q}^2}\left[\frac{1}{n_A^1}\frac{Q^2}{M_A|\mathbf{q}|} \ < n_A \mid W_A^{02}(q,P_A) - W_A^{20}(q,P_A) \mid \ n_A > \right. \\ &\left. -\frac{1}{n_A^3}\frac{q^0}{M_A} < n_A \mid W_A^{12}(q,P_A) - W_A^{21}(q,P_A) \mid n_A > \right], \end{aligned} \tag{1.10}$$

and

$$\begin{aligned} G_2^A(Q^2, q\cdot P_A/M_A) \ &= \ \frac{i}{2}\frac{M_A^2}{\mathbf{q}^2}\left[\frac{1}{n_A^1}\frac{q^0}{|\mathbf{q}|} \ < n_A \mid W_A^{02}(q,P_A) - W_A^{20}(q,P_A) \mid \ n_A > \right. \\ &\left. +\frac{1}{n_A^3} < n_A \mid W_A^{12}(q,P_A) - W_A^{21}(q,P_A) \mid n_A > \right], \end{aligned} \tag{1.11}$$

where all nuclear tensor matrix elements involving the third component of the current are eliminated in favor of matrix elements involving the charge density by current conservation, i.e., by $q_\mu W_A^{\mu\nu}(q,P_A) = W_A^{\mu\nu}(q,P_A)q_\nu = 0$.

In the c.m. frame the structure functions are related to the frame-dependent nuclear response functions by the following relations:

$$W_1^A(Q^2, q\cdot P_A/M_A) = \frac{1}{2}R_T(Q^2,q^0), \tag{1.12}$$

$$W_2^A(Q^2, q\cdot P_A/M_A) = \frac{Q^4}{\mathbf{q}^4}R_L(Q^2,q^0) + \frac{1}{2}\frac{Q^2}{\mathbf{q}^2}R_T(Q^2,q^0), \tag{1.13}$$

$$G_1^A(Q^2, q\cdot P_A/M_A) = -\frac{1}{2}\frac{M_A^2}{\mathbf{q}^2}\left[\frac{Q^2}{M_A|\mathbf{q}|}\sqrt{\frac{1}{2}}R_{TL'}(Q^2,q^0) \; - \; \frac{q^0}{M_A}R_{T'}(Q^2,q^0)\right], \quad (1.14)$$

$$G_2^A(Q^2, q\cdot P_A/M_A) = -\frac{1}{2}\frac{M_A^2}{\mathbf{q}^2}\left[\frac{q^0}{|\mathbf{q}|}\sqrt{\frac{1}{2}}R_{TL'}(Q^2,q^0) \; + \; R_{T'}(Q^2,q^0)\right], \quad (1.15)$$

where R_T, R_L are the spin-averaged nuclear response function, and $R_{TL'}$ and $R_{T'}$ are the spin-dependent response function [1]. They can be calculated from the structure functions by inverting Eq. 1.12 - 1.15 or directly computed from the nuclear current tensor according to

$$R_T(Q^2,q^0) = < n_A \mid W_A^{11}(q,P_A) + W_A^{22}(q,P_A) \mid n_A >, \quad (1.16)$$

$$R_L(Q^2,q^0) = < n_A \mid W_A^{00}(q,P_A) \mid n_A >, \quad (1.17)$$

$$R_{T'}(Q^2,q^0) = -i\frac{1}{n_A^3} < n_A \mid W_A^{12}(q,P_A) - W_A^{21}(q,P_A) \mid n_A >, \quad (1.18)$$

$$R_{TL'}(Q^2,q^0) = -i\sqrt{2}\frac{1}{n_A^1} < n_A \mid W_A^{02}(q,P_A) - W_A^{20}(q,P_A) \mid n_A > . \quad (1.19)$$

1.3.2 The Nuclear Current Tensor in PWIA

The nuclear current tensor is calculated in PWIA as an operator in nuclear spin space, i.e.,

$$\begin{aligned} < s'_A \mid W_A^{\mu\nu}(q,P_A) \mid s_A > \; = \; & \sum_{t_N}\sum_{s_N s_{N'}} \int d^3p_N \frac{M_N}{p_N^0} \int dE < s_{N'} \mid W_{N(t_N)}^{\mu\nu}(q_N,p_N) \mid s_N > \\ & \times < s_N s'_A \mid S(\mathbf{p}_N, E, t_N) \mid s'_N s_A >, \end{aligned} \quad (1.20)$$

where $p_N = (\sqrt{M_N^2 + \mathbf{p}_N^2}, \mathbf{p}_N)$ is the four-momentum of the struck nucleon, q_N ($Q_N^2 = -q_N^2$ being positive) is the momentum transfer to the nucleon by the electron, $s_N(t_N)$ is the nucleonic spin (isospin) projection, and E is the so-called separation energy. $W_{N(t_N)}^{\mu\nu}(q_N,p_N)$ is the nucleonic current tensor and $S(\mathbf{p}_N,E,t_N)$ is the spectral function which contains the nuclear structure information. The spin-independent

part of $S(\mathbf{p}_N, E, t_N)$ is identical to the usual spectral function as described in [21] and is interpreted as the probability for finding a nucleon of isospin t_N and of momentum $\mathbf{p}_N$ in the target nucleus A, the residual $(A-1)$ nucleus having a specified excitation energy, which is related to the separation energy E. Both the nucleonic current tensor $W^{\mu\nu}_{N(t_N)}(q_N, p_N)$ and the spectral function $S(\mathbf{p}_N, E, t_N)$ are considered operators in spin space. The quantization axes of the nuclear spin σ_A and of the nucleonic spin σ_N are chosen along the z direction for the matrix elements of Eq. 1.20. The derivation for the above formula carried out in the nuclear c.m. frame is contained in appendix A in [5] where the procedure in [22] is followed.

The nucleonic current tensor derived in appendix B in [5] has the following form

$$\begin{aligned} W^{\mu\nu}_{N(t_N)}(q_N, p_N) &= -\left[\frac{q^\mu_N q^\nu_N}{Q^2_N} + g^{\mu\nu}\right] W_1^{N(t_N)}(Q^2_N, q_N \cdot p_N/M_N) + \\ & \tilde{p}^\mu_N \tilde{p}^\nu_N \frac{W_2^{N(t_N)}(Q^2_N, q_N \cdot p_N/M_N)}{M^2_N} \\ & + i\epsilon^{\mu\nu\alpha\beta} q_{N\alpha} \left[s_\beta(\sigma_\mathbf{N}) \frac{G_1^{N(t_N)}(Q^2_N, q_N \cdot p_N/M_N)}{M_N} + \{(q_N \cdot p_N) s_\beta(\sigma_\mathbf{N}) \right. \\ & \left. - [q_N \cdot s(\sigma_\mathbf{N})] p_{N\beta} \} \frac{G_2^{N(t_N)}(Q^2_N, q_N \cdot p_N/M_N)}{M^3_N} \right], \end{aligned} \tag{1.21}$$

with

$$\tilde{p}_N = p_N + \frac{q_N \cdot p_N}{Q^2_N} q_N, \tag{1.22}$$

$$s(\sigma_\mathbf{N}) = \left[\frac{\mathbf{p}_N \cdot \sigma_\mathbf{N}}{M_N}, \sigma_\mathbf{N} + \frac{\mathbf{p}_N \cdot \sigma_\mathbf{N}}{M_N(M_N + p^0_N)} \mathbf{p}_N \right], \tag{1.23}$$

where $W_1^{N(t_N)}$ and $W_2^{N(t_N)}$ are the spin-averaged nucleonic structure functions, and $G_1^{N(t_N)}$ and $G_2^{N(t_N)}$ are the spin-dependent nucleonic structure functions. For elastic scattering from the nucleon, the nucleonic structure functions are determined by the elastic Sachs form factors $G_E^{N(t_N)}$ and $G_M^{N(t_N)}$ as follows:

$$W_1^{N(t_N)}(Q^2_N, q_N \cdot p_N/M_N) = \tau [G_M^{N(t_N)}(Q^2_N)]^2 2M_N \delta(2q_N \cdot p_N - Q^2_N), \tag{1.24}$$

$$W_2^{N(t_N)}(Q_N^2, q_N \cdot p_N/M_N) = \frac{[G_E^{N(t_N)}(Q_N^2)]^2 + \tau[G_M^{N(t_N)}(Q_N^2)]^2}{(1+\tau)} \times 2M_N\delta(2q_N \cdot p_N - Q_N^2), \quad (1.25)$$

$$G_1^{N(t_N)}(Q_N^2, q_N \cdot p_N/M_N) = -\frac{G_M^{N(t_N)}(Q_N^2)}{2}\frac{G_E^{N(t_N)}(Q_N^2) + \tau G_M^{N(t_N)}(Q_N^2)}{1+\tau} \times 2M_N\delta(2q_N \cdot p_N - Q_N^2), \quad (1.26)$$

and

$$G_2^{N(t_N)}(Q_N^2, q_N \cdot p_N/M_N) = \frac{G_M^{N(t_N)}(Q_N^2)}{4}\frac{G_M^{N(t_N)}(Q_N^2) - \tau G_E^{N(t_N)}(Q_N^2)}{1+\tau} \times 2M_N\delta(2q_N \cdot p_N - Q_N^2), \quad (1.27)$$

with $\tau = Q_N^2/4M_N^2$ being non-negative.

1.3.3 ^{3}He Spin-Dependent Spectral Function

The spin-dependent matrix elements of the nuclear spectral function are defined by

$$< s_N s'_A \mid S(\mathbf{p}_N, E, t_N) \mid s'_N s_A > = A \sum_{s_{A-1} f_{A-1}} \delta(E + E_A - e_{A-1}(f_{A-1})) \times < \mathbf{P}_A s'_A \mid \mathbf{p}_N s'_N t_N (\mathbf{P}_A - \mathbf{p}_N) s_{A-1} f_{A-1} > \times < \mathbf{p}_N s_N t_N (\mathbf{P}_A - \mathbf{p}_N) s_{A-1} f_{A-1} \mid \mathbf{P}_A s_A > \quad (1.28)$$

The on-mass-shell energies of the $(A-1)$- and A-nucleon systems are approximated such that the respective four-momenta are

$$P_{A-1} \simeq (\sqrt{(A-1)^2 M_N^2 + (\mathbf{P}_A - \mathbf{p}_N)^2} + e_{A-1}(f_{A-1}),\ \mathbf{P}_A - \mathbf{p}_N), \quad (1.29)$$

and

$$P_A \simeq (\sqrt{A^2 M_N^2 + \mathbf{P}_A^2} + E_A,\ \mathbf{P}_A), \quad (1.30)$$

where E_A is the ^{3}He binding energy, f_{A-1} are quantum numbers of excitation in the residual $A-1$ nucleus, and $e_{A-1}(f_{A-1})$ is the excitation energy of the residual $A-1$ nucleon system. The spectral function is an operator in the nucleonic and nuclear spin space. Furthermore, it is a Lorentz scalar with respect to rotations and parity in the nuclear c.m. frame ($\mathbf{P}_A = 0$), due to the fact that the tensor structure of the nuclear current tensor is carried by the nucleonic current tensor. Therefore, the spectral function has the following general operator form in spin space in the case of spin-$\frac{1}{2}$ particles (^{3}He and electron):

$$\begin{aligned} S(\mathbf{p}_N, E, t_N) &= \frac{1}{2}\{f_0(|\mathbf{p}_N|, E, t_N) + f_1(|\mathbf{p}_N|, E, t_N)\sigma_N \cdot \sigma_A \\ &\quad + f_2(|\mathbf{p}_N|, E, t_N)[(\sigma_\mathbf{N} \cdot \hat{\mathbf{p}}_N)(\sigma_\mathbf{A} \cdot \hat{\mathbf{p}}_N) - \frac{1}{3}\sigma_\mathbf{N} \cdot \sigma_\mathbf{A}]\}, \quad (1.31) \end{aligned}$$

Where $f_0(|\mathbf{p}_N|, E, t_N)$ is the spin-averaged part of the spectral function. $f_1(|\mathbf{p}_N|, E, t_N)$ and $f_2(|\mathbf{p}_N|, E, t_N)$ contribute to the spin-dependent part of the spectral function. The spectral function obtained above allows us to differentiate between two-body and three-body final states [5], while previously the PWIA calculation [2] within closure approximation used the spin-dependent momentum distribution which could not distinguish between two-body and three-body final states.

We will describe the convolution formulas for structure functions next using the favorable extraction scheme A of Schulze *et al.* [5]. Discussion of different extraction schemes can be found in appendix D in [5]. In the c.m. frame the spin-$\frac{1}{2}$ target nucleus is characterized by the general polarization vector $\hat{\mathbf{n}}_A$:

$$\sigma_\mathbf{A} \cdot \hat{\mathbf{n}}_A |n_A> = |n_A>, \quad (1.32)$$

$$\rho_A(\hat{\mathbf{n}}_A) = \frac{1}{2}(1 + \hat{\mathbf{n}}_A \cdot \sigma_\mathbf{A}), \quad (1.33)$$

where the operator ρ_A is the corresponding density operator and $|n_A>$ denotes polarization state, which can be expanded in terms of spin states with the z axis

being the quantization axis, $|s_A>$ as $|n_A>=\sum_{s_A}|s_A><s_A|n_A>$. Therefore, the nuclear current tensor derived from Eq. 1.20 using the nucleonic current tensor (Eq. 1.21) and the spectral function (Eq. 1.31) takes the following form

$$< n_A|W_A^{\mu\nu}(q,P_A)|n_A >= Tr[W_A^{\mu\nu}(q,P_A)\rho_A(\hat{\mathbf{n}}_A)], \tag{1.34}$$

$$\begin{aligned} < n_A|W_A^{\mu\nu}(q,P_A)|n_A > \;=\; & -\sum_{t_N}\int d^3p_N\frac{M_N}{p_N^0}\int dE\left\{\left[\left[\frac{q_N^\mu q_N^\nu}{Q_N^2}+g^{\mu\nu}\right]W_1^{N(t_N)}\right.\right. \\ & \left.\left.-\frac{\tilde{p}_N^\mu\tilde{p}_N^\nu}{M_N^2}W_2^{N(t_N)}\right]f_0(|\mathbf{p}_N|,E,t_N)\right. \\ & -i\epsilon^{\mu\nu\alpha\beta}q_{N\alpha}\left[\mathcal{S}_\beta(\mathbf{p}_N,E,t_N,\hat{\mathbf{n}}_A)\frac{G_1^{N(t_N)}}{M_N}\right. \\ & +\{(q_N\cdot p_N)\mathcal{S}_\beta(\mathbf{p}_N,E,t_N,\hat{\mathbf{n}}_A) \\ & \left.\left.-[q_N\cdot\mathcal{S}(\mathbf{p}_N,E,t_N,\hat{\mathbf{n}}_A)]p_{N\beta}\}\frac{G_2^{N(t_N)}}{M_N^3}\right]\right\}. \end{aligned} \tag{1.35}$$

The four-vector $\mathcal{S}(\mathbf{p}_N,E,t_N,\hat{\mathbf{n}}_A)$, which contains all spin-dependent structure information, is determined by

$$\mathcal{S}(\mathbf{p}_N,E,t_N,\hat{\mathbf{n}}_A)=Tr[s(\sigma_\mathbf{N})S(\mathbf{p}_N,E,t_N)\rho_A(\hat{\mathbf{n}}_A)] \tag{1.36}$$

$$\begin{aligned} \mathcal{S}(\mathbf{p}_N,E,t_N,\hat{\mathbf{n}}_A) \;=\; & s(\hat{\mathbf{n}}_A)[f_1(|\mathbf{p}_N|,E,t_N)-\frac{1}{3}f_2(|\mathbf{p}_N|,E,t_N)] \\ & +s(\hat{\mathbf{p}}_N)(\hat{\mathbf{n}}_A\cdot\hat{\mathbf{p}}_N)f_2(|\mathbf{p}_N|,E,t_N), \end{aligned} \tag{1.37}$$

where the vectors $\hat{\mathbf{n}}_A$ and $\hat{\mathbf{p}}_N$ are boosted by the nucleon momentum $\mathbf{p}_N$

$$s(\hat{\mathbf{n}}_A)=\left[\frac{\mathbf{p}_N\cdot\hat{\mathbf{n}}_A}{M_N},\ \hat{\mathbf{n}}_A+\frac{\mathbf{p}_N\cdot\hat{\mathbf{n}}_A}{M_N(M_N+p_N^0)}\mathbf{p}_N\right], \tag{1.38}$$

$$s(\hat{\mathbf{p}}_N)=\left[\frac{|\mathbf{p}_N|}{M_N},\ \hat{\mathbf{p}}_N\frac{p_N^0}{M_N}\right]. \tag{1.39}$$

The nuclear current tensor $W_A^{\mu\nu}(q, P_A)$ in PWIA does not satisfy current conversation. Schulze *et al.* [5] took the approach of using the PWIA nuclear current tensor of Eq. 1.35 only for those longitudinal matrix elements needed in Eq. 1.4 - Eq. 1.7 after current conservation is already exploited (so-called scheme A). The resulted convolution formulas for the structure functions in scheme A are:

$$W_1^A = \sum_{t_N} \int d^3p_N \frac{M_N}{p_N^0} \int dE \left[W_1^{N(t_N)} + \frac{W_2^{N(t_N)}}{2M_N^2} |\hat{\mathbf{q}} \times \mathbf{p}_N|^2 \right] f_0(|\mathbf{p}_N|, E, t_N), \quad (1.40)$$

$$\begin{aligned} W_2^A &= \sum_{t_N} \int d^3p_N \frac{M_N}{p_N^0} \int dE \left\{ \frac{W_2^{N(t_N)}}{M_N^2} \left[\frac{Q^4}{\mathbf{q}^4} \left[p_N^0 + q_N^0 \frac{q_N \cdot p_N}{Q_N^2} \right]^2 + \frac{1}{2} \frac{Q^2}{\mathbf{q}^2} |\hat{\mathbf{q}} \times \mathbf{p}_N|^2 \right] \right. \\ &\left. + W_1^{N(t_N)} \frac{Q^2}{\mathbf{q}^2} \left[1 - \frac{Q^2}{Q_N^2} \right] \right\} f_0(|\mathbf{p}_N|, E, t_N), \end{aligned} \quad (1.41)$$

$$\begin{aligned} G_1^A &= \frac{M_A^2}{\mathbf{q}^2} \sum_{t_N} \int d^3p_N \frac{M_N}{p_N^0} \int dE \left[\frac{Q^2}{M_A} \frac{1}{n_A^1} g^{1\alpha} + \frac{q^0}{M_A} \frac{1}{n_A^3} (q_N^0 g^{3\alpha} - |\mathbf{q}| g^{0\alpha}) \right] \\ &\times \left[\mathcal{S}_\alpha(\mathbf{p}_N, E, t_N, \hat{\mathbf{n}}_A) \frac{G_1^N}{M_N} + \{ (q_N \cdot p_N) \mathcal{S}_\alpha(\mathbf{p}_N, E, t_N, \hat{\mathbf{n}}_A) \right. \\ &\left. - [q_N \cdot \mathcal{S}(\mathbf{p}_N, E, t_N, \hat{\mathbf{n}}_A)] p_{N\alpha} \} \frac{G_2^N}{M_N^3} \right], \end{aligned} \quad (1.42)$$

$$\begin{aligned} G_2^A &= -\frac{M_A^2}{\mathbf{q}^2} \sum_{t_N} \int d^3p_N \frac{M_N}{p_N^0} \int dE \left[q^0 \frac{1}{n_A^1} g^{1\alpha} + \frac{1}{n_A^3} (q_N^0 g^{3\alpha} - |\mathbf{q}| g^{0\alpha}) \right] \\ &\times \left[\mathcal{S}_\alpha(\mathbf{p}_N, E, t_N, \hat{\mathbf{n}}_A) \frac{G_1^N}{M_N} + \{ (q_N \cdot p_N) \mathcal{S}_\alpha(\mathbf{p}_N, E, t_N, \hat{\mathbf{n}}_A) \right. \\ &\left. - [q_N \cdot \mathcal{S}(\mathbf{p}_N, E, t_N, \hat{\mathbf{n}}_A)] p_{N\alpha} \} \frac{G_2^N}{M_N^3} \right]. \end{aligned} \quad (1.43)$$

Fig 1.2 shows the calculated structure functions [23] for the kinematics of the present work with electron incident energy of 370 MeV and scattering angle of 91.4°.

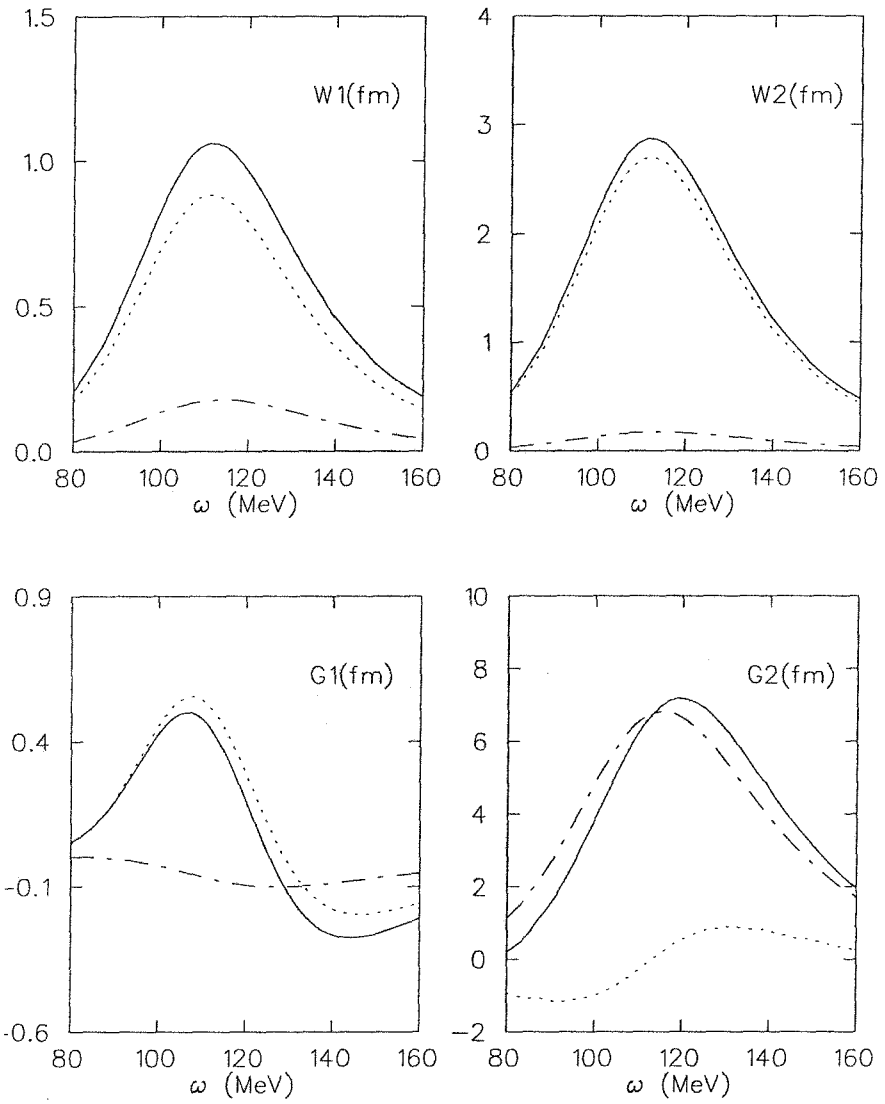

Figure 1.2: Structure functions calculated for the present work, MEPS kinematics with electron incident energy of 370 MeV and scattering angle of 91.4°. All four structure functions are in units of fermi with the dotted line being the proton contribution, the dash-dotted line being the neutron contribution, and the solid line being the total (^{3}He).

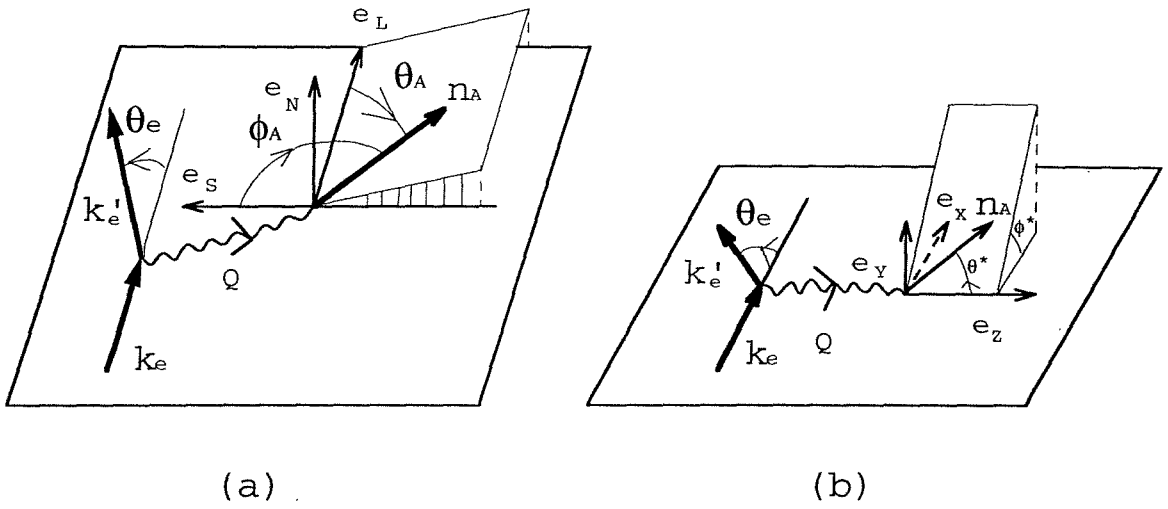

Figure 1.3: Definitions of the target spin angles. (a) The target spin angles are defined w.r.t the three-momentum vector of the incident electron; (b) the target spin angles are defined w.r.t the three-momentum transfer vector.

1.3.4 ^{3}He Quasielastic Asymmetry

Before discussing the inclusive scattering formalism with polarization and the formalism for quasielastic scattering of polarized electrons from polarized ^{3}He nuclei, we will define the kinematic variables relevant to the rest of this chapter.

The cross-section is calculated in the laboratory frame, i.e., in the nuclear c.m. frame with $\mathbf{p}_A = 0$. The four-momentum transfer from the electron to the target is $q = (\omega, \mathbf{q})$ with ω being the energy loss and $Q^2 = -q^2$ being positive; $K = (E, \mathbf{k})$ is the incident electron four-momentum; $K' = (E', \mathbf{k}')$ is the four-momentum of the outgoing electron; the electron scattering angle is θ; $\sigma_{Mott} = (e^2/8\pi E)^2 \cos^2\frac{\theta}{2}/\sin^4\frac{\theta}{2}$ is the Mott cross section, and h is the incident electron helicity $+1(-1)$ for spin parallel (antiparallel) to $\mathbf{k}$. The target polarization $n_A = (0, \hat{\mathbf{n}}_A)$ is parametrized by the two sets of angles (θ_A, ϕ_A) with the spin angles being defined with respect to the three-momentum of the incident electron, or by (θ^*, ϕ^*) with respect to the three-momentum transfer vector $\mathbf{q}$ as shown in Fig. 1.3.

The inclusive cross-section for longitudinally polarized electrons scattered quasielastically from polarized ^{3}He target can be written [5] in terms of the structure

functions $(W_1^A, W_2^A, G_1^A, G_2^A)$ described previously as

$$\begin{aligned}\frac{d^2\sigma}{dE'd\Omega} &= \sigma_{Mott}\Bigg\{W_2^A(Q^2,\omega) + 2\tan^2\frac{\theta}{2}W_1^A(Q^2,\omega) \\ &+2h\tan^2\frac{\theta}{2}\left[\frac{G_1^A(Q^2,\omega)}{M_A}[E\cos\theta_A + E'(\cos\theta\cos\theta_A + \sin\theta\sin\theta_A\cos\phi_A)]\right. \\ &\left.-2\frac{G_2^A(Q^2,\omega)}{M_A^2}EE'[\cos\theta_A - (\cos\theta\cos\theta_A + \sin\theta\sin\theta_A\cos\phi_A)]\right]\Bigg\}, \quad (1.44)\end{aligned}$$

or, equivalently [1],

$$\begin{aligned}\frac{d^2\sigma}{dE'd\Omega} &= \sigma_{Mott}\Big\{[v_L R_L(Q^2,\omega) + v_T R_T(Q^2,\omega)] \\ &-h[v_{T'}\cos\theta^* R_{T'}(Q^2,\omega) + 2v_{TL'}\sin\theta^*\cos\phi^* R_{TL'}(Q^2,\omega)]\Big\}, \quad (1.45)\end{aligned}$$

where v_k are kinematic variables [1] defined as following

$$v_L = \frac{Q^4}{|\mathbf{q}|^4}, \quad (1.46)$$

$$v_T = \frac{1}{2}\frac{Q^2}{|\mathbf{q}|^2} + \tan^2\frac{\theta}{2}, \quad (1.47)$$

$$v_{T'} = \tan\frac{\theta}{2}\sqrt{(\frac{Q^2}{|\mathbf{q}|^2}) + \tan^2\frac{\theta}{2}}, \quad (1.48)$$

$$v_{TL'} = -\frac{1}{\sqrt{2}}\frac{Q^2}{|\mathbf{q}|^2}\tan\frac{\theta}{2}. \quad (1.49)$$

The spin-dependent quasielastic asymmetry is defined as

$$A = \frac{\frac{d^2\sigma}{dE'd\Omega}_+ - \frac{d^2\sigma}{dE'd\Omega}_-}{\frac{d^2\sigma}{dE'd\Omega}_+ + \frac{d^2\sigma}{dE'd\Omega}_-}, \quad (1.50)$$

where $+$ $(-)$ denotes positive (negative) electron helicity. The quasielastic asymme-

try takes the following explicit form

$$\begin{aligned} A &= 2\tan^2\frac{\theta}{2}\left\{\frac{G_1^A(Q^2,\omega)}{M_A}[E\cos\theta_A + E'(\cos\theta\cos\theta_A + \sin\theta\sin\theta_A\cos\phi_A)]\right. \\ &\quad \left. -2\frac{G_2^A(Q^2,\omega)}{M_A}EE'[\cos\theta_A - (\cos\theta\cos\theta_A + \sin\theta\sin\theta_A\cos\phi_A)]\right\} \\ &\quad [W_2^A(Q^2,\omega) + 2\tan^2\frac{\theta}{2}W_1^A(Q^2,\omega)]^{-1}, \end{aligned} \tag{1.51}$$

or equivalently [1]

$$A = -\frac{\cos\theta^* v_{T'}R_{T'}(Q^2,\omega) + 2\sin\theta^*\cos\phi^* v_{TL'}R_{TL'}(Q^2,\omega)}{v_L R_L(Q^2,\omega) + v_T R_T(Q^2,\omega)}. \tag{1.52}$$

As can be seen from the above equation in θ^* kinematics, by orienting the target spin at $\theta^* = 0°$ or $\theta^* = 90°$, corresponding to the target spin direction either along the 3-momentum transfer vector $\mathbf{q}$ or normal to it, one can select the transverse asymmetry $A_{T'}$ (proportional to $R_{T'}$) or the transverse-longitudinal asymmetry $A_{TL'}$ (proportional to $R_{TL'}$). The experimentally measured asymmetry A_{exp} is the physics asymmetry A diluted by the product of the target polarization (P_t) and the beam polarization (P_b).

$$A_{exp} = P_t P_b A \tag{1.53}$$

1.4 Extraction of G_M^n from a Measurement of ^{3}He $A_{T'}$

1.4.1 Nucleon Form Factors

Before discussing the extraction of information about the neutron electromagnetic properties from the ^{3}He data, it is useful to present the expressions for the cross section and asymmetry in elastic electron scattering from a free nucleon. Using the notation of Donnelly and Raskin [1], the expression for the unpolarized cross section

is written in terms of the longitudinal and transverse elastic form factors, F_L and F_T, where

$$F^2(Q^2) = v_L F_L^2(Q^2) + v_T F_T^2(Q^2). \tag{1.54}$$

The longitudinal and transverse form factors are related to the Sach's form factors, $G_E(Q^2)$, the electric (or more correctly, charge) nucleon form factor, and $G_M(Q^2)$, the magnetic nucleon form factor, by

$$\sqrt{4\pi} F_L = (1+\tau) G_E \tag{1.55}$$

$$\sqrt{4\pi} F_T = -\sqrt{2\tau(1+\tau)} G_M, \tag{1.56}$$

where $\tau \equiv Q^2/4M_N^2$.

The Sach's form factors have a simple, intuitive interpretation. In the nonrelativistic limit, they are related to the Fourier transform of the charge and current distribution within the nucleon, and in the $Q^2 = 0$ limits reduce to

$$G_E(Q^2 = 0) = q_N \tag{1.57}$$

$$G_M(Q^2 = 0) = \mu_N, \tag{1.58}$$

where q_N is the nucleon charge and μ_N is the magnetic moment of the nucleon. The unpolarized cross section is written in terms of G_E and G_M as

$$\frac{d\sigma}{d\Omega} = \sigma_{Mott} f_{recoil}^{-1} \left((1+\tau)^2 v_L G_E^2 + 2\tau(1+\tau) v_T G_M^2 \right), \tag{1.59}$$

where f_{recoil}^{-1} is the recoil factor

$$f_{recoil}^{-1} = 1 + \frac{|\mathbf{k}|' E - |\mathbf{k}| E' \cos\theta}{|\mathbf{k}|' M_N}. \tag{1.60}$$

For the neutron, it is clear from this relationship that at low Q^2 the magnetic form factor dominates over the electric form factor. For this reason, it is difficult to extract

the neutron electric form factor from unpolarized scattering data. If the neutron is polarized, then the spin-dependent part of the cross section, written as

$$\begin{aligned}\Delta &= -\sigma_{Mott} f_{recoil}^{-1} \Big[2\tau(1+\tau) v_{T'} \cos\theta^* {G_M^n}^2(Q^2) \\ &\quad + 2(1+\tau)\sqrt{2\tau(1+\tau)} v_{TL'} \sin\theta^* \cos\phi^* G_M^n(Q^2) G_E^n(Q^2) \Big], \end{aligned} \tag{1.61}$$

contains an interference term proportional to $G_E^n G_M^n$, as well as a term proportional to ${G_M^n}^2$, so the spin-dependent part of the cross section is more sensitive than the unpolarized cross section to the electric form factor of the neutron.

The spin-dependent asymmetry for the nucleon,

$$A = \frac{(\frac{d\sigma}{d\Omega})_+ - (\frac{d\sigma}{d\Omega})_-}{(\frac{d\sigma}{d\Omega})_+ + (\frac{d\sigma}{d\Omega})_-}, \tag{1.62}$$

is expressible in terms of the electric and magnetic form factors as

$$A_{\vec{e}\vec{N}} = -\frac{2\tau v_{T'} \cos\theta^* G_M^2(Q^2) + 2\sqrt{2\tau(1+\tau)} v_{TL'} \sin\theta^* \cos\phi^* G_M(Q^2) G_E(Q^2)}{(1+\tau) v_L G_E^2 + 2\tau v_T G_M^2}. \tag{1.63}$$

1.4.2 Extraction of G_M^n from a Measurement of $A_{T'}$

As was mentioned earlier, due to the lack of a free neutron target, our current knowledge of G_M^n at low Q^2 region is derived almost exclusively from electron-deuteron scattering data, a process which in general is model-dependent. Though G_M^n is known much better than G_E^n in the low Q^2 region, it is known with much less precision than the proton electromagnetic form factors.

Polarized ^{3}He is a good approximation of a polarized neutron target because for its nuclear ground state about 90% of the time it is in the spatially symmetric S state in which the spins of the two protons pair off, leaving the neutron carrying the nuclear spin. As discussed in Sec 1.4.1, in $^3\vec{\text{He}}(\vec{e}, e')$ quasielastic scattering, by orienting the ^{3}He target spin direction at certain angles, one can maximize the

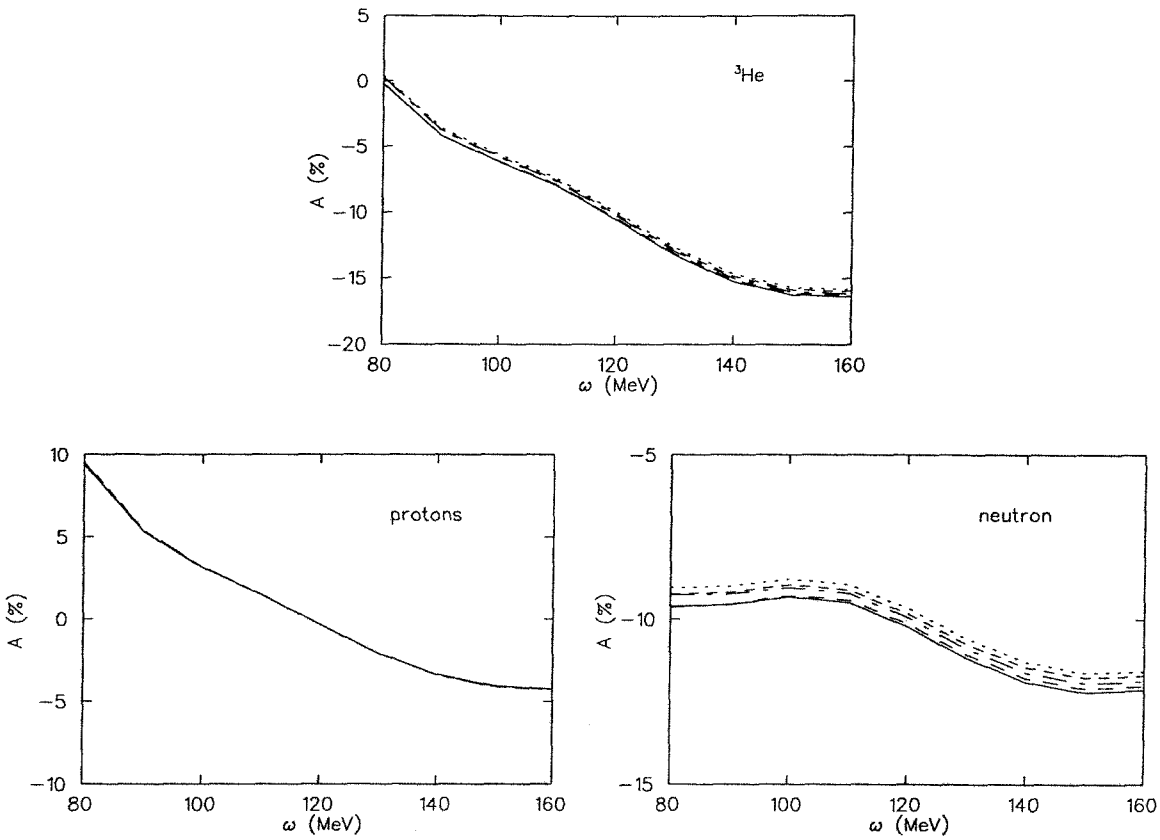

Figure 1.4: Calculations of $A_{T'}$ by Salmè *et al.* at the kinematics of the present work with $E = 370$ MeV, $\theta = -91.4°$ and $\beta = 42.5°$, versus different form factor parametrizations. Plotted are the neutron, proton, and total contributions to $A_{T'}$. The solid line is for the Galster parametrization, the long dashed line is for Galster [8] with $G_E^n = 0$, the dash-dotted line is for Gari-Krümpelmann [20], the short-dashed line is for Höhler [19], and the dotted line is for Blatnik-Zovko [26] form factor parametrizations. The ^{3}He quasielastic peak is around $\omega = 120$ MeV where the proton contribution is almost zero.

sensitivity of the asymmetry to either the neutron electric form factor or magnetic form factor.

The recent PWIA calculations [4-5] using a spin-dependent spectral function, which neglect FSI and MEC, have shown that due to the small size of the neutron electric form factor, the ^{3}He transverse-longitudinal asymmetry $A_{TL'}$ is dominated by the proton contribution. Unfortunately, this makes the idea of extracting G_E^n from a measurement of $A_{TL'}$ in inclusive quasielastic scattering of longitudinally polarized electrons from a polarized ^{3}He target questionable. Nevertheless, the calculations

have demonstrated that $A_{T'}$ is dominated by the neutron contribution in the vicinity of ^{3}He quasielastic peak and $A_{T'}$ is also very sensitive to G_M^{n2}. The asymmetry calculation of Laget [24] shows that the effect of MEC and FSI on the transverse asymmetry for the exclusive process $^3\vec{\mathrm{He}}(\vec{e},e'n)pp$ at the Q^2 of the present work is negligible. Thus one can experimentally extract the neutron magnetic form factor from a measurement of the transverse asymmetry $A_{T'}$. Fig. 1.4 shows the $A_{T'}$ calculations at the kinematics of the present work (electron incident energy $E = 370$ MeV, $\theta = 91.4°$ to the left of the electron beam, and spin angle $\beta = 42.5°$ to the right of the beam corresponding to $\theta^* = 8.9°$) performed by Salmè *et al.* [25] versus different form factor parametrizations, with the neutron and the proton contributions plotted separately. As is clear from the plot, $A_{T'}$ is very sensitive to the neutron magnetic form factor.

The theoretical uncertainty (so-called model dependence) associated with this technique of extracting G_M^n arises both from the uncertainties in the ^{3}He wave function and the uncertainties in the proton electromagnetic form factors. The effect from the neutron electric form factor is negligible as G_E^n is very small compared with G_E^p and G_M^p at the Q^2 of this work. The model dependence will be discussed in detail later in Chapter 6 when we present the asymmetry results and the extracted G_M^{n2} value from this thesis work. Fig. 1.5 shows the calculations of $A_{T'}$ by Salmè *et al.* [25] and Schulze *et al.* [23] for the MEPS kinematics, with $E = 370$ MeV, $\theta = 91.4°$ and $\theta^* = 8.9°$. The small difference between the two calculations probably arises from the different ^{3}He wave functions and form factor parametrizations used in the calculations, although this has not yet been verified. The calculation of Salmè *et al.* used a variational wave function for the Reid soft-core interaction and the Gari-Krümpelmann [20] form factor parametrization. Schulze *et al.* used the Faddeev wave function for the Paris potential and the Galster form factor parametrizations [8] in their calculation.

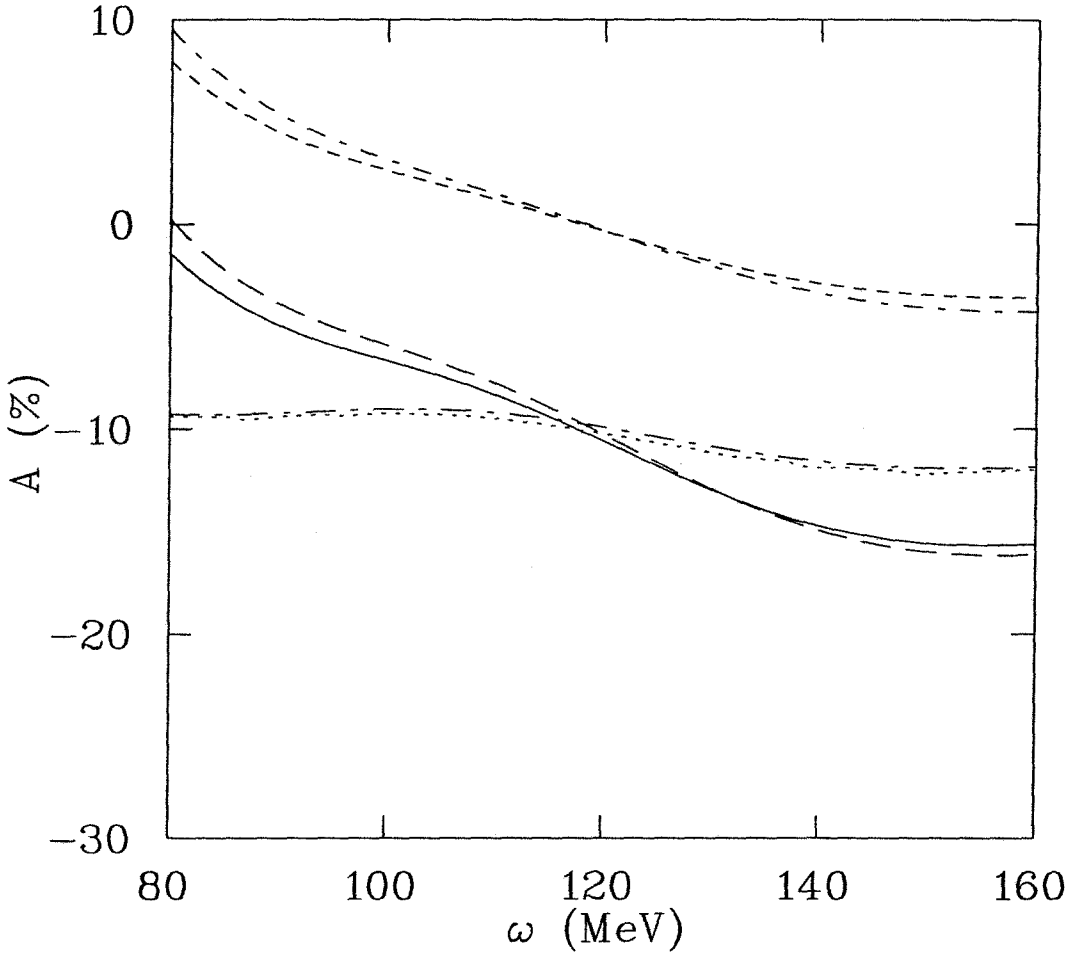

Figure 1.5: Calculations of $A_{T'}$ by Salmè *et al.* and Schulze *et al.* for the MEPS kinematics, with $E = 370$ MeV, $\theta = -91.4°$ and $\beta = 42.5°$. For the calculations of Schulze *et al.*, the solid line is the ^{3}He asymmetry $A_{T'}$, the dashed line is the proton contribution, and the dotted line is the neutron contribution. For the calculations of Salmè *et al.*, the long-dashed line is the ^{3}He asymmetry $A_{T'}$, the dash-dotted line is the proton contribution, and the long dash-dotted line is the neutron contribution.

Chapter 2

The Experimental Apparatus

2.1 Overview

The experiment to measure the quasielastic spin-dependent asymmetry (MIT-Bates 88-25) was a collaboration among five institutes: Argonne National Lab, Caltech, MIT, RPI, and TRIUMF. The experiment was performed at the MIT-Bates Linear Accelerator Center in May and June of 1993 on beamline B in the South Experimental Hall. Longitudinally polarized electrons were scattered quasielastically from a polarized ^{3}He target, which was developed at Caltech. Because of the importance of the target in the experiment, it will be described in a separate chapter. This chapter describes other aspects of the experiment.

A single-pass electron beam of an energy of 370 MeV was obtained from the polarized injector, which will be discussed in more detail in Section 2.2. A Wien spin rotator was employed to produce longitudinally polarized electrons at the target. The linac operated at 600 pulses per second with a pulse width of 15 μsec and a typical peak current of 2-3 mA on the target.

The scattered electrons were detected in singles mode in two spectrometers, the One Hundred Inch Proton Spectrometer (OHIPS), and the Medium Energy Pion Spectrometer (MEPS). The OHIPS spectrometer was configured at an angle of 70.1°

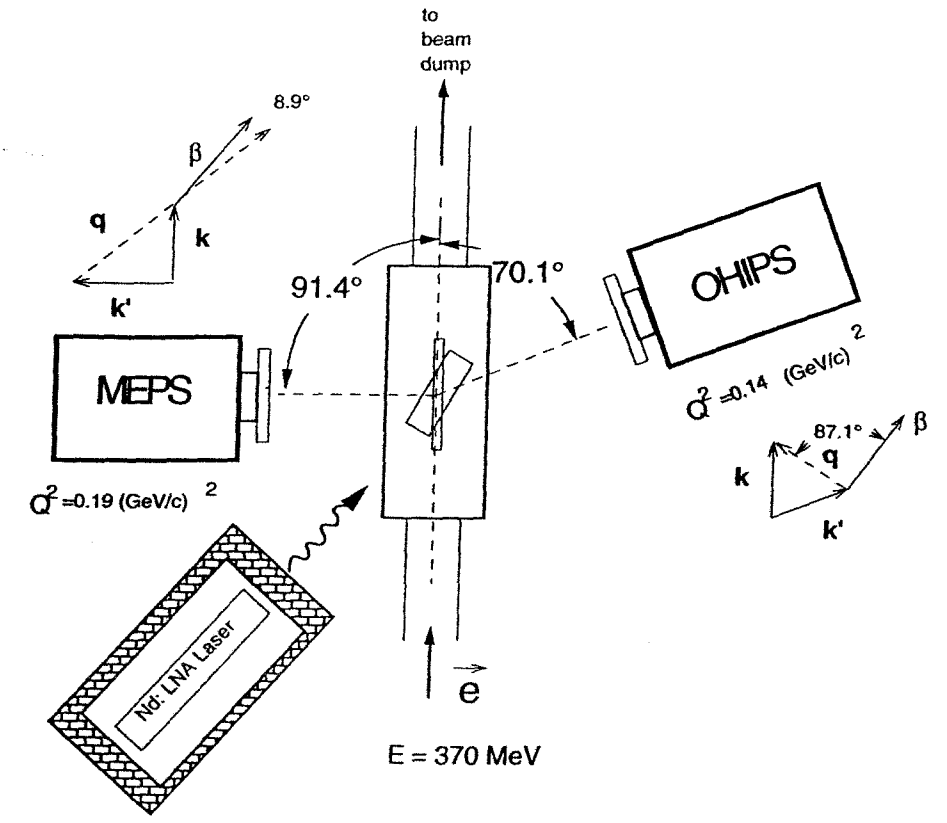

Figure 2.1: Experimental layout for the spectrometers and the laser system.

to the right of the beam line. It was used to measure both the ^{3}He asymmetry in the elastic-threshold region, and the ^{3}He quasielastic asymmetry around the top of the quasielastic peak so several different central momentum settings were used. The MEPS spectrometer was located to the left of the beam line at an angle of 91.4°. The central momentum of the spectrometer was set to correspond to the center of the quasielastic peak. Both spectrometers will be described in more detail in Section 2.4. Fig. 2.1 is a schematic layout of the spectrometers and the target laser system for the experiment. Table 2.1 lists the kinematics for the measurements.

High voltage on a Pockels cell in the laser polarizing optics was varied to change the helicity state of the optical pumping laser light, thus reversing the target spin direction. The target spin direction was flipped several times a day during the experiment to minimize systematic uncertainties. The two target spin directions

Spectrometer Setting	θ (deg)	Q^2 $(\mathrm{GeV/c})^2$	$\vec{q}$ (MeV/c)	θ^* (deg)	ϕ^* (deg)
MEPS quasielastic	-91.4	0.19	455	8.9	180
OHIPS quasielastic	70.1	0.14	383	87.1	0
OHIPS elastic	70.1	0.166	409	94.0	0

Table 2.1: Kinematics for MEPS and OHIPS quasielastic and elastic measurements. Positive scattering angle was defined with respect to the beam right direction. θ^* was listed only for the positive target spin angle (beam right). The target spin was also reversed and for the negative target spin angle, θ^* is equal to the difference between 180° and the θ^* value for the positive target spin direction.

were $\theta^* = 8.9,\ 171.1°$, where θ^* is the spin polar angle defined with respect to the 3-momentum transfer vector $\mathbf{q}$, for the MEPS spectrometer, which was configured at the kinematics sensitive to the transverse asymmetry $A_{T'}$. The target spin directions were $\theta^* = 87.1,\ 92.9°$ for OHIPS quasielastic setting, which was located at the kinematics sensitive to the transverse-longitudinal asymmetry $A_{TL'}$.

2.2 Polarized Electron Beam

The polarized electron source at Bates is a GaAs sourced based on the design from SLAC [27]. Polarized electrons can be produced by various techniques [28]. Photoemission from GaAs has several advantages: high peak current achieved, helicity reversal by optical means, and the feasibility of building a GaAs source with small transverse phase space or emittance, an important requirement for the Bates machine.

The GaAs polarized electron source works through photoemission of electrons that have been polarized through optical pumping. An electron in the valence band of GaAs, a direct band gap crystal, absorbs the circularly polarized laser light with a wavelength between 750 and 800 nm, and is excited to the conduction band. The electron diffuses to the crystal surface, which has been treated with cesium to create

a negative electron affinity, and then escapes to the beam line vacuum.

The optical pumping light for the source is provided by a Ti:sapphire laser driven by an Ar-ion laser. A linear polarizer and a Pockels cell, acting as a quarter-wave plate, are used in the laser optics system to convert the linearly polarized laser light into circularly polarized light. High voltage on the Pockels cell was varied to change the helicity state of the laser light, thus changing the helicity of the polarized electrons. The electron helicity was selected randomly on a pulse by pulse basis. For operating the accelerator with the polarized electron source, the accelerator is phase-locked to the line frequency of 60 Hz. For the experiment Bates 88-25, the accelerator was operated at a rep rate of 600 Hz. The helicity of the beam pulse was selected randomly in each of the first 10 pulses, then chosen to be the opposite helicity of those values for the next 10 pulses. Varying the electron helicity in this fashion allows pulse-pair asymmetry analysis of the data, which is much less sensitive to the noise problem associated with any asymmetry measurement. This feature is especially important for parity-violation experiments because of the small physics asymmetries involved. The data of the present work were not analyzed in the pulse-pair fashion as the quasielastic and elastic asymmetries are relatively large compared to the false asymmetry from this effect.

The electrons from the polarized source were longitudinally polarized with an energy of 380 KeV. The electron beam was then accelerated in the linac and went through the 90° bend of the switching magnet that directed the beam into the B line of the South Hall. The electrons were no longer longitudinally polarized after the 90° bend because of the g-2 effect. The precessing angle with respect to the electron momentum for a given bend angle, θ_{bend}, is given by

$$\theta = \frac{g-2}{2}\gamma\theta_{bend}, \tag{2.1}$$

where γ is the relativistic factor, $\frac{E}{m_e}$, and g is the Landé g factor for the electron magnetic dipole moment. So the precession angle is 76° for a 90° bend.

A Wien spin rotator (Wien filter) was employed to produce the longitudinally polarized electrons at the target for this experiment. A Wien spin rotator is a device which uses crossed electric and magnetic fields to rotate the polarization vector of a particle without changing its momentum. It is located right after the polarized injector, where the beam energy is low, and upstream of all of the bunching and accelerating elements. The electron beam has a finite energy spread in the low energy part of the accelerator due to the bunching elements, which compress the cw beam into pulses by decelerating the leading part and accelerating the trailing part of the beam pulse. The magnetic field of the focussing solenoids will cause a spin precession about the magnetic field of the transverse polarization vector, as axes of the solenoids are parallel to the beam momentum direction. The angle of the spin precession is energy dependent. The Wien spin rotator rotates the polarization vector away from the longitudinal direction in order to produce longitudinally polarized electrons at the target, causing a ϕ rotation of the electron polarization vector away from the 76° direction imposed by the Wien spin rotator, as well as a ϕ spread as a function of the beam energy because of the beam energy spread and the magnetic field from the focussing solenoids. The Wien filter was calibrated carefully and the ϕ rotation of the electron polarization vector versus the currents in the solenoids was mapped out completely before the experiment. The ϕ spread was also studied and the effect was found to be negligible. So the Wien spin rotator was set properly to produce the longitudinally polarized electrons at the target during the experiment based on the calibration of the Wien spin rotator and the mapping of the ϕ rotation versus the solenoids currents.

The quantum efficiency of the GaAs crystal was $\sim 1-3\%$ with a typical lifetime of 3-4 days during the experiment. The average beam current at the target was $25\mu A$. Three beam toroids on the B-line, BT1, BT2, and BT3 with BT2 closer to the polarized ^{3}He target, were used to monitor the beam charge by measuring the induced current during the beam pulse. The energy-defining slits in the accelerator were set so that the beam energy spread was $\sim$ 0.3% FWHM. The beam energy

was determined using the dipole bending magnet (FB1) at the 14° line and the calibration [29] relating the nominal energy (MeV) to the true beam energy:

$$E = \frac{E_{nom}}{0.987 + E_{nom}(5.6 \times 10^{-5})} \tag{2.2}$$

The beam energy is determined to be 370 MeV using this formula, which also agrees (within 1 %) with the beam energy determined from the optics study and the ^{3}He elastic runs.

2.3 Møller Polarimeter

The electron beam polarization was measured using a variable energy Møller polarimeter [30]. This polarimeter, which is located in the north dump area and upstream of the polarized ^{3}He target, was developed for measuring the electron beam polarization for the B beam line at Bates. It was used previously for Bates polarized ^{3}He experiments [6] [7] in the spring of 1990 where the electron beam energy was 574 MeV. For those runs, the uncertainty in the determination of the beam polarization was $\pm$10%.

The design and operation of the Møller polarimeter employed in the present work is described elsewhere [30] and will be discussed briefly here for completeness. Determination of electron beam polarization using a Møller apparatus is based on measurement of the spin-dependent asymmetry for polarized electrons scattered elastically from polarized atomic electrons (Møller scattering) [31]. In the case of longitudinally polarized electrons impinging on a magnetized foil and scattering from longitudinally polarized atomic electrons which are aligned along the magnetic field (beam line direction), the differential cross section for Møller scattering can be written in terms of a spin-independent piece and a spin-dependent piece in the center of

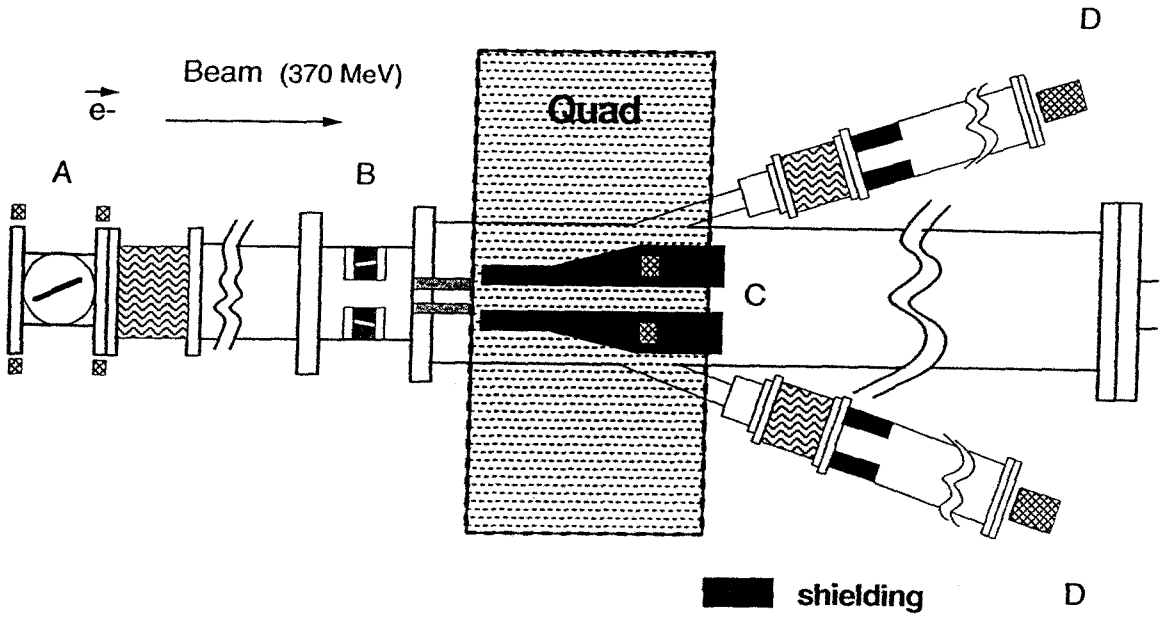

Figure 2.2: Layout of the Bates B-line Møller apparatus, (A) Møller target; (B) and (C) collimators; (D) detectors.

mass (CM) frame as [32]:

$$\left(\frac{d\sigma}{d\Omega}\right)_{cm} = \frac{\alpha^2}{8E^2}\left[\frac{2(3+\cos^2\Theta)^2}{\sin^4\Theta} + h_1 h_2 \frac{2(7+\cos^2\Theta)}{\sin^2\Theta}\right], \tag{2.3}$$

where Θ is the scattering angle in the CM frame and h_1 and h_2 are the helicities of the incident and target electrons.

One can therefore form the asymmetry from the cross-section difference between the right- and left-handed incident electrons:

$$A_M = \frac{\left(\frac{d\sigma}{d\Omega}\right)_R - \left(\frac{d\sigma}{d\Omega}\right)_L}{\left(\frac{d\sigma}{d\Omega}\right)_R + \left(\frac{d\sigma}{d\Omega}\right)_L} = P_t P_b \frac{\sin^2\Theta(7+\cos^2\Theta)}{(3+\cos^2\Theta)^2} \tag{2.4}$$

where P_t and P_b are the target and beam polarizations, respectively. The asymmetry is maximum for $\Theta = 90°$ in the CM frame, which corresponds to a scattering angle of 3.01° in the lab frame for an electron beam energy of 370 MeV. The experimentally measured asymmetry is diluted by the background from processes other than Møller scattering and is given by:

$$A_{meas} = A_M \left(\frac{1}{1 + B/S} \right), \tag{2.5}$$

where S is the rate from Møller scattering and B is the background rate.

Fig. 2.2 is a schematic diagram of the B-line Møller polarimeter. The apparatus consists of a target chamber surrounded by a pair of Helmholtz coils with the field $\vec{B}$ along the beam direction, followed by a collimator to select the Møller scattered electrons in the horizontal plane at a CM angle of 90° (3.01°, in the lab frame). Downstream is a quadrupole magnet that bends the electrons away from the beam direction providing momentum selection. Deflected electrons are then detected in aerogel Čerenkov counters. The distance between the target and the collimator was adjusted for a beam energy of 370 MeV. A new beam dump located downstream of the polarimeter but upstream of the polarized ^{3}He target was installed for this experiment to protect the main target area and nearby electronics from beam spray during Møller measurements. Previously water-cooled slits were used as a beam dump for the ^{3}He experiments in 1990. It was discovered that the polarized ^{3}He target degraded very fast because of the repeated exposure to the beam spray from Møller measurements due to the inefficiency of the water-cooled slits. With the new beam dump, no obvious degrading of the ^{3}He target was found during the Møller measurements for this work.

The target chamber contained a movable ladder with two Supermendur (49% Fe, 49% Co, 2% Va by mass) targets, of thickness $13\mu m$ and $25\mu m$ for polarization measurements. Longitudinal polarization was generated in the plane of the foils, which was inclined at 30° to the beam, with a field of 150 G (the saturation field

$\sim$ 100 G) produced by the Helmholtz coils. In addition to the Supermendur foils, BeO and Al targets were used for alignment of the beam and other diagnostics. An empty target frame was also available to allow the beam to pass through to the main experimental area further downstream. The target polarization of each foil was determined to be 8% before the experiment by measurements of the internal magnetic field. The $13\mu m$-thick foil was used for beam polarization measurements in this experiment.

By selecting a CM scattering angle of 90°, both electrons have the same final energy and can be detected in coincidence mode in the two Čerenkov detectors at identical angles on each side of the beam line. For this experiment, all of the data collected for the beam polarization measurements were taken in singles mode. The signals from the detectors were recorded by integrating the photomultiplier tube current over the $15\mu s$ of the incident beam pulse. Each signal was then divided by the beam charge in the beam pulse and tagged by the beam helicity. The quadrupole field was scanned across the Møller peak in order to determine the signal to background ratio under the peak. For this experiment, additional collimators and shielding material were installed for each detector which improved the signal to background ratio substantially. The typical signal to background ratio for the asymmetry measurement was 3.7:1 (previously 1:6). Different fitting procedures were used to fit the background underneath the Møller peak to minimize systematic uncertainty associated with the fitting procedure. The average of the polarizations determined from the two detectors was assigned for the beam polarization, and an overall systematic uncertainty of $\pm 4\%$ was assigned to it. The systematic uncertainty in the determination of the beam polarization is dominated by the uncertainty associated with fitting the background ($\pm 3\%$), the uncertainty of the target foil polarization ($\pm 1.25\%$), and the uncertainty of the angle of the target foil plane with respect to the beam direction ($\pm 1\%$).

There is an additional correction to the beam polarization due to the intra-atomic motion of bound electrons. This effect was first studied by Levchuk [33]

^{3}He runs	P_b %
≤ 128	36.1 $\pm$ 1.44
130 - 134	38.1 $\pm$ 1.52
135 - 150	37.0 $\pm$ 1.48
151 - 216	36.6 $\pm$ 1.46
217 - 231	37.6 $\pm$ 1.50
232 - 252	36.3 $\pm$ 1.45
253	35.0 $\pm$ 1.40
254 - 272	31.1 $\pm$ 1.24
273 - 282	33.3 $\pm$ 1.33
283 - 292	36.1 $\pm$ 1.44
294 - 312	37.8 $\pm$ 1.51
313 - 351	37.0 $\pm$ 1.48
352 - 379	35.7 $\pm$ 1.43
380 - 381	37.9 $\pm$ 1.52
382 - 396	36.9 $\pm$ 1.48

Table 2.2: Beam polarization versus the ^{3}He asymmetry runs.

for the Bates polarimeters and it was found that the beam polarization could be lower by $8 - 10\%$ (relative percentage) due to this effect. Recently this effect for the B-line Møller polarimeter was studied using a more realistic scattering angle and momentum acceptance and a more realistic momentum distribution [34] and a 2% effect was found for this experiment.

Typically a Møller measurement was taken right after the source crystal had been reactivated and one or more runs were taken before the next reactivation. The average of the measured polarizations between the two activations was used as the beam polarization for the ^{3}He asymmetry measurements during that period of time. The average beam polarization from all the Møller measurements was 36.5%. Table 2.2 listed the beam polarization determined from the Møller measurements versus the run numbers for the ^{3}He asymmetry measurements.

2.4 The Spectrometers

2.4.1 OHIPS

The OHIPS spectrometer consists of two quadrupole magnets and a 100-in radius dipole magnet, which bends particles in the vertical plane (QQD). For this experiment, the quadrupoles were operated in the VH mode, where Q1 focused in the dispersive direction (x) and Q2 focused in the direction transverse to the bend plane (y). This configuration gives better angular acceptance for the extended targets at the expense of the momentum resolution, a quantity less important for quasielastic asymmetry measurement because of the wide quasielastic peak caused by Fermi motion of the nucleons inside the nucleus.

The spectrometer was moved as close as possible to maximize the solid angle; the drift distance from the target center to the effective field of the first quadrupole was 93 cm. A 21 cm-thick lead collimator was attached in front of the first quadrupole to reduce the spectrometer background and define the solid angle acceptance. The collimator opening was 17.1 cm (x direction, closer to the ^{3}He target) by 7.6 cm (y direction, closer to the ^{3}He target).

The detector package for OHIPS consisted of a crossed-wire, vertical drift chamber (VDCX), three planes of trigger hodoscopes to form the event trigger, and a Čerenkov detector. The readout system for the OHIPS VDCX is a delay line system (see Section 4.1). The Čerenkov detector was used for pion rejection. Each hodoscope was a NE110 plastic scintillator. S0 and S1 were 0.48 cm thick, and S2 was 3.8 cm thick. A detailed discussion of the VDCX and its electronic readout is described elsewhere [35]. For the ^{3}He quasielastic asymmetry measurement, the spectrometer was set to have a central momentum of 287 MeV/c. Fig. 2.3 shows the OHIPS detector layout.

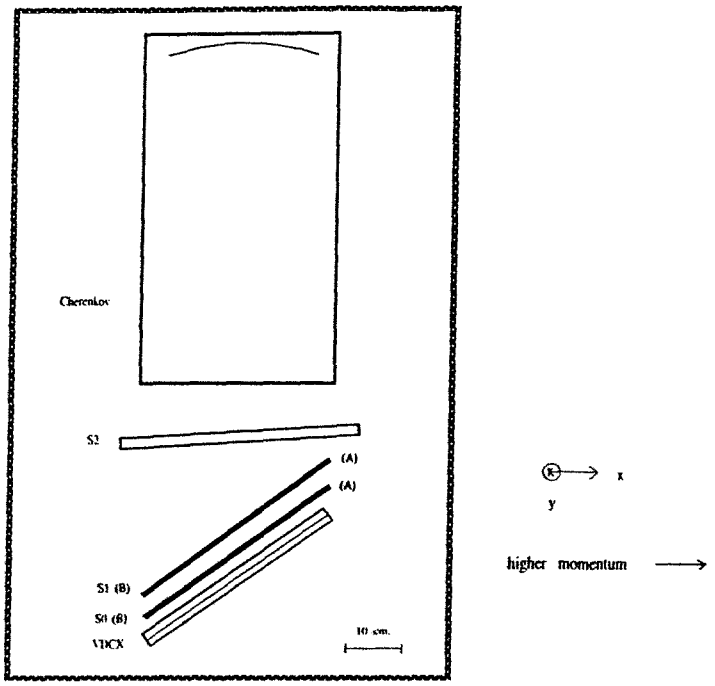

Figure 2.3: OHIPS detector layout.

2.4.2 MEPS

The Bates Medium Energy Pion Spectrometer (MEPS) consists of two quadrupole magnets and one dipole magnet with a bending radius of 0.75 m. The optics of MEPS is point-to-point in the dispersive (vertical, x) direction $< x|\theta > = 0$ with a small dispersive magnification $< x|x > = 0.4$. The optics in the transverse (horizontal, y) direction is parallel-to-point $< y|y > = 0$, so that measuring the transverse position in the focal plane is roughly equivalent to measuring the scattering angle. The quadrupoles were configured such that Q1 focused in the horizontal direction and Q2 focused in the vertical direction for this experiment resulting in a poor extended target acceptance (2 cm) and a good momentum resolution.

The first drift from the target center to the effective field boundary of the first quadrupole was 51 cm. A 5 cm-thick lead collimator was installed to the front of Q1 to minimize the background and defined the solid angle. The collimator was 5.2 cm (x direction, closer to the ^{3}He target) by 7.6 cm (y direction, closer to the ^{3}He target).

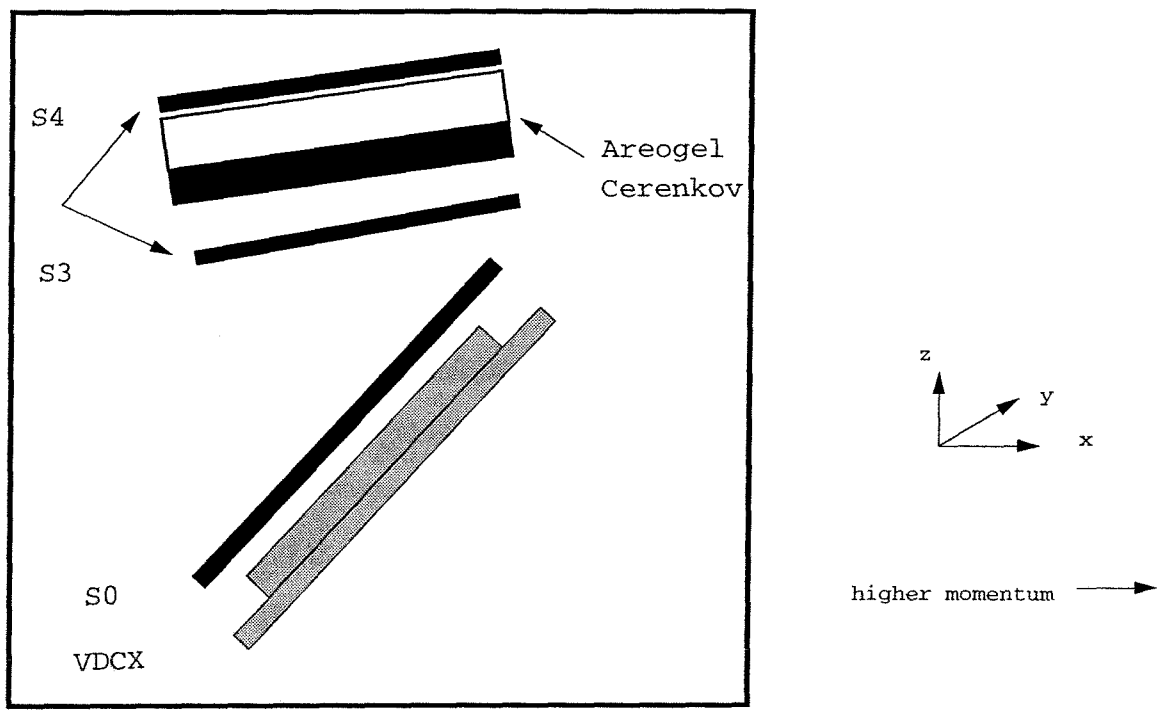

Figure 2.4: MEPS detector layout.

The detector package consisted of crossed vertical drift chamber (VDCX), three planes of trigger scintillators, and a silica aerogel Čerenkov detector for pion rejection. The first scintillator (S0) between the VDCX and the Čerenkov detector is a segmented two-piece plastic (one phototube for each section) which is of the same size as that of the VDCX. There is one more scintillator (S3) between the VDCX and the Čerenkov detector. S4 is the last scintillator located above the Čerenkov counter. S3 and S4 were viewed by two phototubes (one at each end) and were mean-timed in the electronics. The Čerenkov counter was made of silica aerogel (n = 1.05) and was viewed by 10 5" RCA phototubes. For most of the ^{3}He quasielastic asymmetry measurement, MEPS was set to have a central momentum of 250 MeV/c. Fig. 2.4 shows MEPS detector layout.

Detailed information on the MEPS VDCX readout system is given in [36] and will be described briefly here. Previously MEPS VDCX was equipped with a Bates-built readout system TIRUS (Time Interval Readout Using Scalers) [37]. For this

experiment TIRUS was replaced by a commercially available system (LeCroy 4290 Drift Chamber System) which together with software and additional electronics has been termed DCOS (Drift Chamber Operating System). The DCOS system is similar to the LeCroy PCOS-III system for multiwire proportional chambers. DCOS and TIRUS are both TDC-per-wire systems and DCOS operates almost identically to TIRUS. The advantages of the TDC-per-wire readout system over the delay line system are: no ambiguity about the identity of the fired wire, higher efficiency of the chamber (better than 99.5%), and the possibility that any number of wires can fire simultaneously. Though it is much more expensive than the delay line system.

2.5 Data Acquisition System

The data were acquired using the LAMPF "Q" data acquisition system [38] running on a dedicated microVAX III computer. The Q system was set up to trigger on each beam-burst and read the integrated charge, measured by the beam toroids upstream of the target, and the electron helicity for that beam-burst. Therefore, the charge was counted accurately for each beam helicity. The Q system also read scalers and the event data for both spectrometers. The target polarization was acquired by a separate acquisition and control system running on a dedicated microVAX II (see Section 3.5.3). The polarization information was passed to the main data acquisition system every second through CAMAC event registers. The beam helicity information was included in the event stream for each spectrometer, in addition to being included in each beam-burst event.

Data were acquired in single-arm modes for both spectrometers. The analog signals from the phototubes for the scintillators were used to form the trigger logic in addition to being sent through Analog to Digital Converters (ADC) and Time to Digital Converters (TDC) for the spectrometer event data stream. The digitized information from all the detectors was buffered by the Microprogrammable Branch Driver (MBD), then transferred to the Q data acquisition system, which stored the

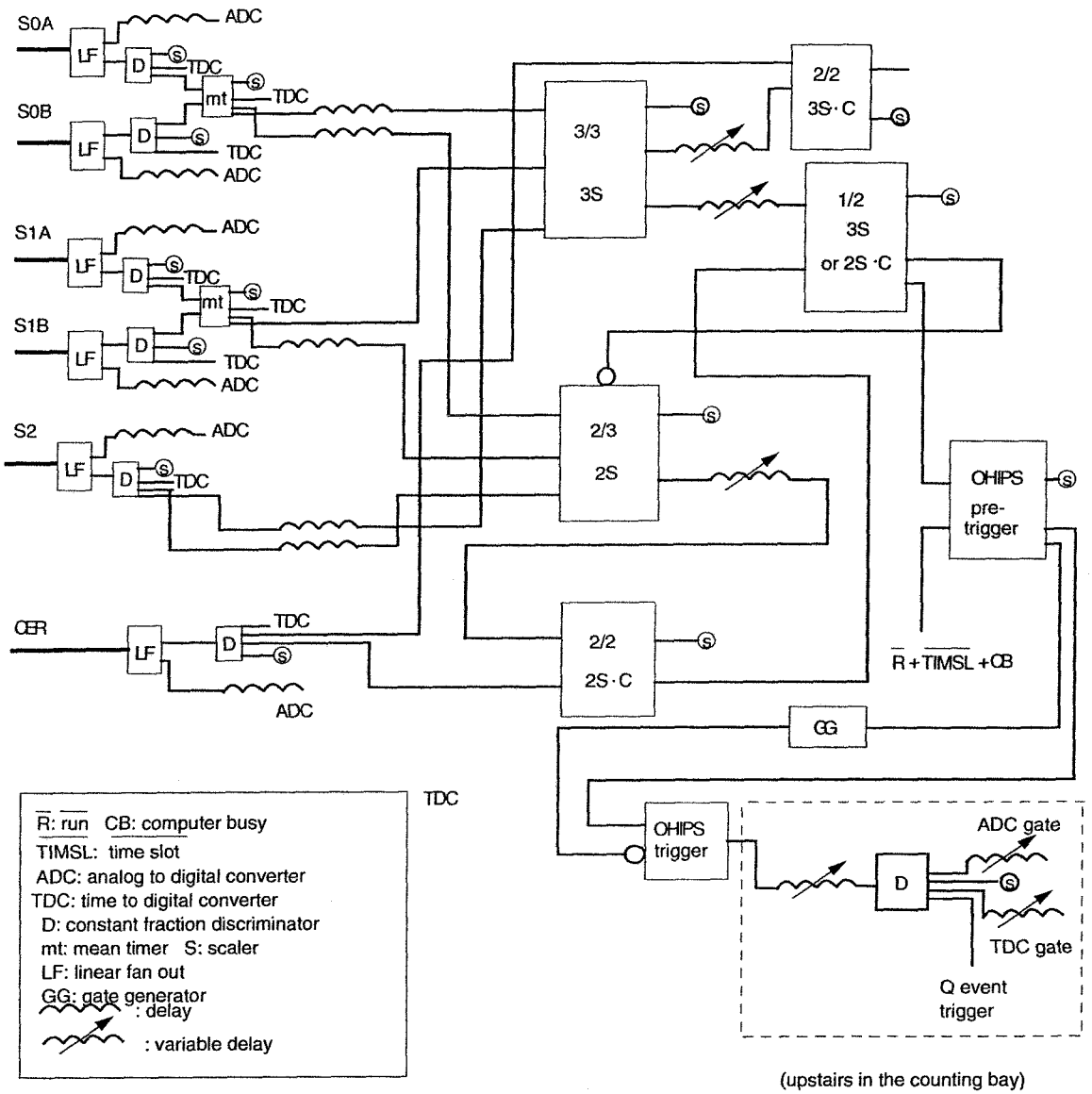

Figure 2.5: OHIPS event trigger logic.

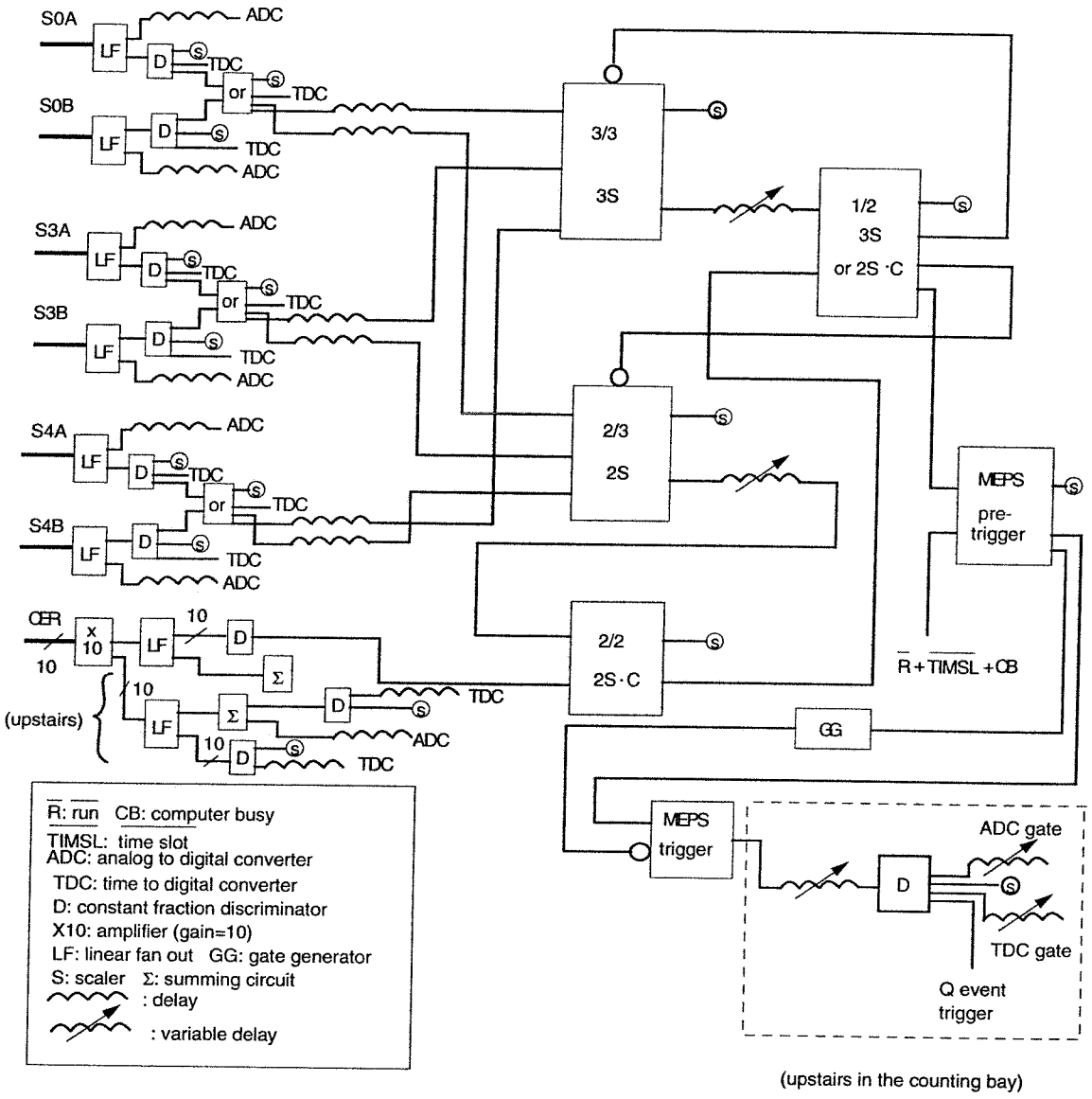

Figure 2.6: MEPS event trigger logic.

events on 8-mm tape and performed the online analysis.

Figure 2.5 shows the OHIPS event trigger logic. The ungated OHIPS event trigger required a signal from all three scintillators, or a hit in each of any two out of the three scintillators together with a hit in the Čerenkov counter, with a veto for events outside the beam gate or when data acquisition was not requested by the Q system. The gated events were vetoed if the computer was busy and were limited to a single event per beam-burst. MEPS event trigger was formed in the same way as that of OHIPS and Figure 2.6 is a diagram for the MEPS event trigger.

Chapter 3

The Polarized ^{3}He Target

The polarized ^{3}He target employed in this experiment was an external cryogenic gas target using the metastability-exchange optical pumping technique. This technique was developed in the early 1960s at Rice university [39] to polarize ground state ^{3}He or ^{4}He atoms through metastability-exchange collisions with optically pumped ^{3}He or ^{4}He metastable atoms. Since the invention of this optical pumping technique to polarize helium ground state atoms, the use of polarized helium in atomic and nuclear physics has generated much interest and activity in the community. The applications of spin-polarized helium atoms range over several fields of physics. They include the ^{4}He and now ^{3}He magnetometers, which can be used to measure the earth and the interplanetary magnetic fields [40]; polarized beams of metastable helium atoms for the study of atomic collisions and to probe magnetic surfaces [41]; polarized targets and beams in nuclear physics [42-44] and the application to study quantum properties of polarized ^{3}He fluid at low temperature [45].

Earlier attempts to build polarized ^{3}He targets for nuclear physics are described elsewhere [46]. With the development of laser technology much effort has been directed towards developing the polarized ^{3}He nuclear targets for electron scattering experiments. The target discussed in this work was first developed at Caltech [47] and used previously in an experiment at the Bates Linear Accelerator Center (Bates

88-02) [6]. In this experiment, the spin-dependent asymmetry in quasielastic scattering of longitudinally polarized electrons from polarized ^{3}He was measured for the first time. Since this experiment, we have substantially improved the target performance and stability largely due to the development of the LNA laser. The earlier attempts to construct a dense polarized ^{3}He target with high polarization (25%) were embarked on by a group at Toronto [48-49]. They used the metastability-exchange optical pumping technique to polarize the ^{3}He atoms and tried to achieve the high density (1 atmosphere) by compressing the ^{3}He atoms using a mercury Toeppler pump. They failed in the end because of the difficulty of working with the mercury compression pump and the limited pumping rate achieved with the ^{4}He lamp. Recently, a new type of dense polarized ^{3}He gas target using the metastability-exchange optical pumping technique has been developed at Mainz [50-51]. A first measurement of the neutron electric form factor in the exclusive quasielastic scattering of polarized electrons from polarized ^{3}He was made recently at the Mainz Microtron MAMI using this new type of dense polarized ^{3}He target [52]. K. Lee *et al.* have developed a polarized ^{3}He internal gas target and have taken data successfully using the polarized proton beam at IUCF with their internal target [53]. The MIT group is currently building another internal ^{3}He target for the HERMES experiment, which will run over the next few years. Because the polarized ^{3}He nucleus is a very interesting nucleus for polarization studies, many experiments using polarized ^{3}He targets are underway at several major electron accelerator facilities: SLAC, DESY HERA, MAINZ, CEBAF, and MIT-Bates. These experiments will study the neutron electromagnetic structure and the spin structure of the nucleons.

3.1 Optical Pumping of ^{3}He

Optical pumping is a method of transferring angular momentum from the photons of a pump beam to the sample atoms. Often the pumping transition corresponds to the optical transition from the ground state to the first excited state, but this is not

practical for helium because it is difficult to produce radiation at the high photon energy (21 eV) that is required to reach the first excited state.

Two indirect techniques have been developed to optically pump ^{3}He atoms, one by Colegrove, Schearer and Walters in the early 1960s [39] and referred to as the metastability-exchange optical pumping technique. This method involves optical pumping of 2^3S_1 metastable state atoms, then transferring the polarization to ^{3}He ground state atoms through metastability-exchange collisions, in which the excitation of the electronic cloud is exchanged leaving the ground state polarized after the collision. Another technique for polarizing ^{3}He involves spin-exchange with polarized alkali atoms; however, because this technique was not used for the Caltech polarized ^{3}He target, it is not discussed here.

Metastability-exchange optical pumping of ^{3}He works as follows: metastable 2^3S_1 atoms are produced by an electrodeless weak rf discharge in a glass cell filled to a pressure of order 1 torr of pure ^{3}He. The ratio of the ground state atoms to the 2^3S_1 atoms is about $10^6 : 1$; the exact number depends on discharge characteristics such as intensity, uniformity and the discharge frequency. The sample is placed in a weak uniform magnetic field which defines the spin direction of the sample. Right-handed or left-handed circularly polarized light (defined by the right-hand rule used in atomic physics) at $\lambda = 1083.4\ nm$ corresponding to the transition of $2^3S_1 \rightarrow 2^3P_0$ excites transitions between the 2^3S_1 and 2^3P_0 states with the selection rule $\Delta m = \pm 1$ depending on the helicity of the incident light (+ for the right-handed circularly polarized light and − for the left-handed case). The pumping light excites atoms from the $m_F = -\frac{1}{2}$ and $m_F = -\frac{3}{2}$ sublevels of the metastable state to the 2^3P_0 level which then decay back to all sublevels of 2^3S_1 through spontaneous emission. The result is that atoms from lower magnetic sublevels of the 2^3S_1 level ($m_F = -\frac{1}{2}$, $m_F = -\frac{3}{2}$) are transferred to higher sublevels of the 2^3S_1 level ($m_F = \frac{1}{2}$, $m_F = \frac{3}{2}$), hence the metastable atoms become polarized. In metastable state, hyperfine interaction mixes electronic polarization into nuclear polarization. The polarization of the metastable atoms is then transferred to the ground state through

metastability-exchange collisions in which only the excitation of the electronic cloud is exchanged. If the ground state of ^{3}He is polarized, then the nucleus is polarized because the atom is in a $J = 0$ state. This process can be expressed schematically as:

$$^3He + ^3\vec{H}e^* \rightarrow ^3\vec{H}e + ^3He^* \tag{3.1}$$

where $*$ denotes the 2^3S_1 metastable state and the vector notation indicates that the nucleus is polarized.

Figure 3.1 shows the level scheme of the 2^3S_1 and 2^3P states of the ^{3}He atom including fine and hyperfine structure. The transition lines between states 2^3S_1 and 2^3P are labeled as C1-C9. Figure 3.2 shows the relative frequencies and intensities of these 9 transition lines. The achievable ground state polarization vs. pumping light intensity for the four major transition lines, C1, C5, C8 and C9, has been studied in detail [54] under two extreme pressure conditions, one, the low pressure limit where there is no collisional depolarization of the 2^3P state and the other one, the high pressure limit where there is total collisional depolarization. For the pressure of ~ 2.0 torr where our target operates, they found that C8 and C9 yield higher polarization than that obtained with C5. The performance of C8 and C9 for our polarized ^{3}He target has been investigated thoroughly at Caltech [55]. C9 is determined to be superior to C8 in terms of the pumping rate and the achievable polarization for the target with a ^{3}He gas pressure of ~ 2.0 torr.

There are a few relative timescales associated with the two processes discussed above, the optical pumping of the metastable state 2^3S_1 and the metastability-exchange collision between the 2^3S_1 state and the ground state 1^1S_0. τ_p (pump-up time) stands for the time constant characterizing the approach to equilibrium in the optical-pumping process if no other mechanisms exist to mix the sublevels of the metastable atoms. τ_r stands for the spin-lattice relaxation time constant of the metastable atoms. T_r denotes the ground state nuclear relaxation time. τ_2 and T_2 are of the order of the lifetimes of the metastable and ground state atoms, respec-

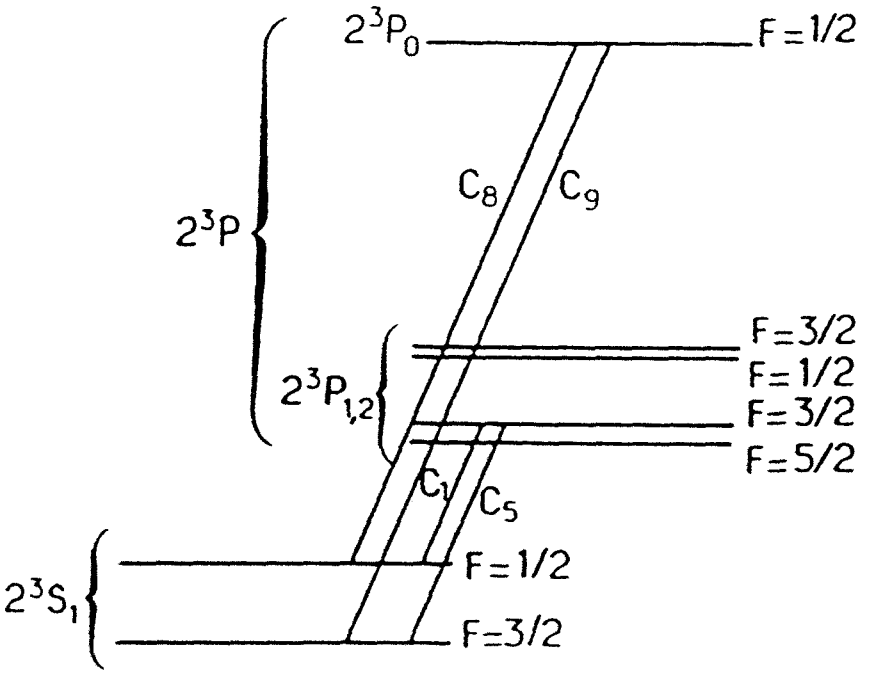

Figure 3.1: Level diagram for the 2^3S and 2^3P states of ^{3}He. [54]

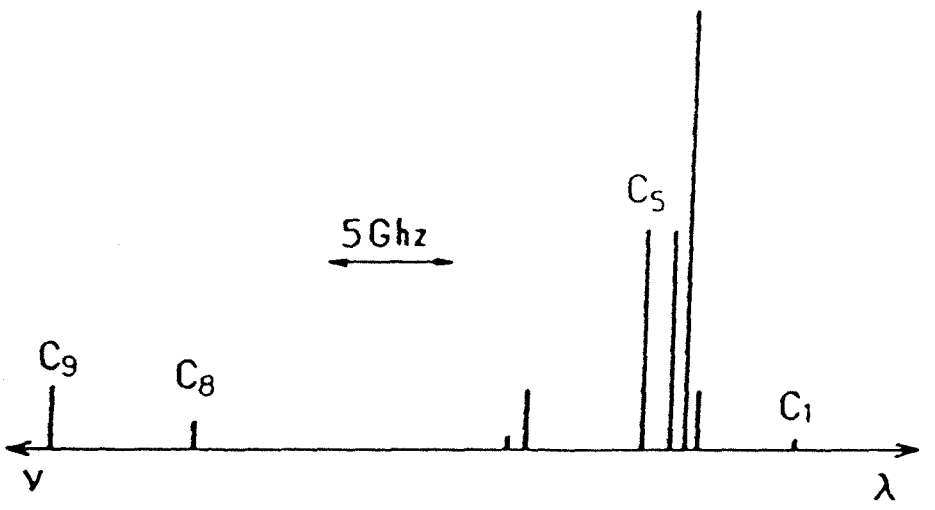

Figure 3.2: Relative strength and frequency of the transition lines for $2^3S \rightarrow 2^3P$ states of ^{3}He. [54]

tively, before undergoing the metastability-exchange collision and τ is the lifetime of the 2^3P state ($\sim 10^{-7}$ seconds). τ_c stands for the timescale for the collisional mixing of the 2^3P atoms. A detailed discussion of all these timescales is given in [56]. It is necessary that the spin relaxation timescales be long compared to the metastability exchange timescales in order to polarize the ground state efficiently. The metastability-exchange rate can be written in terms of the metastability exchange cross-section, σ_e, which is very temperature dependent for the case of ^{3}He atoms [56] [57].

$$\frac{1}{T_e} = < \sigma_e v > n_m \tag{3.2}$$

$$\frac{1}{\tau_e} = < \sigma_e v > N_g \tag{3.3}$$

where the brackets denote thermal averages, N_g and n_m are the number densities of the ground state and the metastable state atoms respectively. It is necessary to operate optical pumping around room temperature to achieve efficient optical pumping because σ_e decreases roughly two orders of magnitude between 300 K and 4.2 K. For a gas at one torr at room temperature, typical values in good optical pumping conditions are $T_e \sim 1$ s and $\tau_e \sim 10^{-6}$ s. There are several relaxation mechanisms crucial for building a polarized ^{3}He target which have been studied and described in detail in [47] and will be discussed briefly in Section 3.5.1. The relaxation times are sensitive to the exact operating conditions, but in general, $\tau_r \sim 10^{-4}$ s and $T_r \sim 100$ s. The metastable pumping rate is dependent upon the power and the spectral characteristics of the pumping light. With the current laser sources for optical pumping, metastable pump-up times of order 10^{-7} s have been achieved, which are significantly shorter than that obtained with a ^{4}He lamp (10^{-4} s) used in the early work of optical pumping of ^{3}He.

This optical pumping technique only works for relatively low pressure conditions (0.1 torr to 10 torr). Destruction of metastables at the wall of the container dominates the relaxation at pressures below about 0.1 torr and at high pressures the

lifetime of the metastable state atoms limits the optical pumping efficiency. It is also experimentally difficult to maintain a uniform discharge under high pressure conditions.

The metastability-exchange optical pumping technique has benefited substantially from the development of lasers that operate in the infrared region. A Nd:YAP (neodymium-doped yttrium-aluminum-perovskite) laser [58] [59], pumped by a krypton arc lamp, was used by Jones *et al.* [6]. In 1986 Laird Schearer, Michele Leduc and co-workers developed and tested a new laser that employs a neodymium-doped lanthanum magnesium hexaluminate crystal (LNA) [60] [61]. While the frequency required for optical pumping of ^{3}He is at the end of the Nd:YAP tuning curve, it is near the center for LNA. Furthermore, the LNA laser outperforms the YAP laser in terms of power and stability. The LNA laser has been used to polarize the target in the present work and the laser system will be discussed in detail in Section 3.3.

3.2 The Polarized ^{3}He Target Apparatus

Because the metastability-exchange optical pumping technique works well only at relatively low gas pressure region (0.1 torr to 10 torr) near room temperature, people have tried successfully to make a dense nuclear physics target by mechanically compressing the polarized gas. At Toronto, Timsit *et al.* in the early 1970s [49] constructed a dense target and achieved a density of 0.7×10^{19}cm^{-3} with 3% polarization by compressing the gas with liquid mercury. However, the performance of these targets was severely limited by the absence of laser sources for optical pumping. Recently, at Mainz Otten *et al.* have designed and built a new type of dense polarized ^{3}He target using the compression method [50] [51] and have achieved pressures around 1 bar with 38% of polarization [52]. Low temperature is another approach to take to construct a dense polarized ^{3}He target. A double-cell system consisting of a pumping cell and a target cell is a practical design for a polarized ^{3}He nuclear target. The pumping cell is at room temperature where metastability-exchange optical

pumping can be performed efficiently and the target cell is cooled to low temperature where a practical luminosity can be achieved for a nuclear physics experiment. This idea was first explored at Rice University [62]. The ^{3}He nuclei in the target cell become polarized because the polarized ^{3}He atoms diffuse between the pumping cell and the target cell, reaching an equilibrium polarization state.

At Caltech, the low temperature approach has been used to achieve higher densities. A double-cell polarized ^{3}He target [47] has been developed over the last few years. This target system consists of a pyrex glass pumping cell at room temperature and an OFHC copper target cell which is connected to a ^{4}He gas refrigerator cold surface through flexible copper braids. The pumping cell is connected to the copper target cell by a pyrex glass transfer tube. Fig. 3.3 shows the layout of the target apparatus as seen from the top and the side.

The pumping cell, 6.35 cm in diameter by 15 cm long, is made of standard pyrex tubing with 0.32 cm thick pyrex windows for endcaps. The target cell is 2.54 cm in diameter and 16 cm long with a wall thickness of 0.254 mm. The target cell windows are 5.8×10^{-4}-cm-thick copper foils which have been tested for pinholes with a floodlamp. The transfer tube is made of standard pyrex glass tubing chosen to have an i.d. of 1.2-1.25 cm and is 6.6 cm long. Fig. 3.4 is a diagram of the target and the pumping cells. Low-temperature epoxy, Emerson and Cumings Stycast 2850GT with catalyst LV24 is mixed (ratio of 100:7 by weight) to connect the glass transfer tube to the pumping cell, the transfer tube to the copper target cell and to attach the copper foil windows to the target. Eight straight copper leads are attached to the outer side of the pumping cell to generate an electrical discharge that is as uniform as possible. The copper target cell is cleaned chemically before attaching the copper foils to the target cell and the target cell to the glass tube. Detailed description of the target machining, assembling, and alignment can be found in [47].

An important part of the target system is the vacuum and gas handling system. The double-cell system is connected to a turbo pump, through a bypass valve to a roughing pump which is connected to the scattering chamber, as well as to the

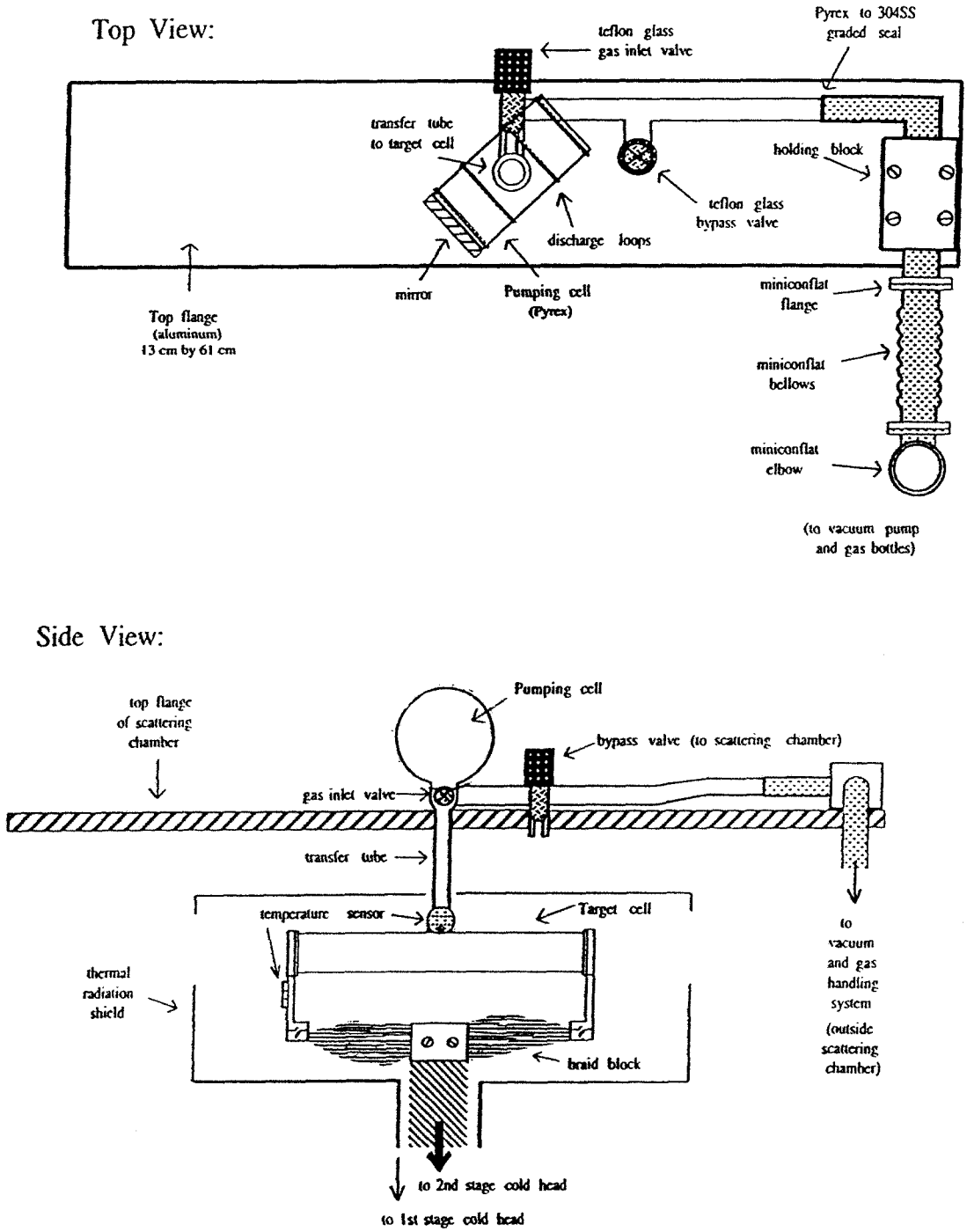

Figure 3.3: Top and side view of the general layout of the target apparatus. In the top view the pumping cell and part of the plumbing can be seen. In the side view, both the pumping cell and the target cell are shown, along with the thermal radiation shield, the temperature sensors, and the braid block.

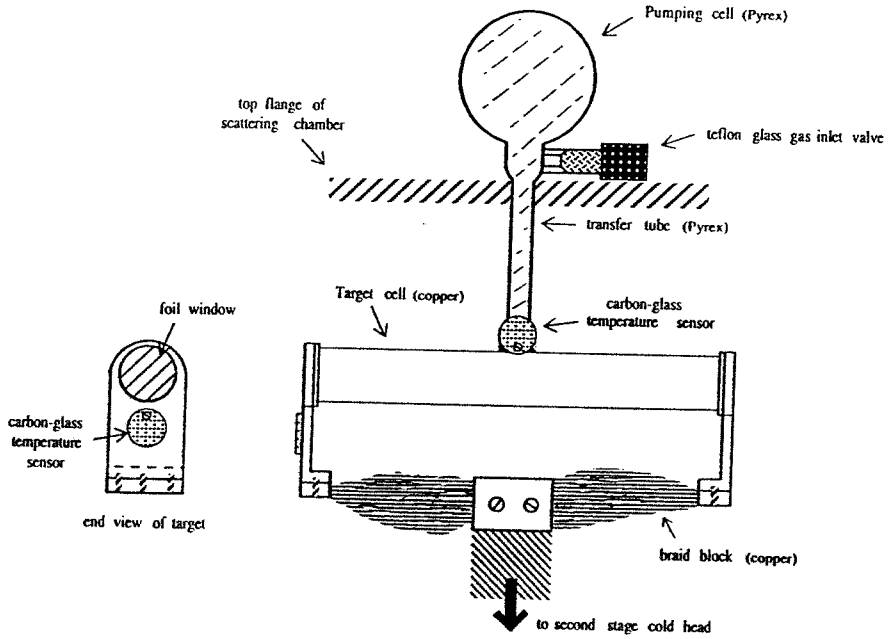

Figure 3.4: Schematic of the polarized ^{3}He target double-cell system. The relative positions of the pumping cell, transfer tube, and target cell are shown, in addition to the braid block, the temperature sensors, and the gas inlet valve.

helium gas bottle to fill the target with pure ^{3}He gas and the nitrogen gas bottle to coat the target at low temperature to minimize the low temperature surface effect. There are also an ion gauge and thermocouple gauges to measure the vacuum of the system, a baratron head (MKS Instruments Type 122A pressure transducer) to monitor the target pressure during filling and evacuation. There are two teflon valves in the system; one isolates the double-cell system from the rest of the vacuum and gas handling system, the other one serves as the bypass valve between the target system and the scattering chamber as care must be taken during initial pump out to not break the foil windows, which can only withstand a differential pressure of 20-40 torr. There are also various other valves in the system to isolate the target system from the turbo pump and to control the filling of the target. Detailed information on the vacuum and gas handling system is given in [47].

The target cell is cooled by a Cryomech GB04, closed cycle, helium refrigerator which consists of two cold surfaces, a first stage ($\sim$ 10 K) and a second stage (30$-$40 K). The copper target cell is connected to the second stage cold surface by flexible

copper braids and OFHC copper blocks. The flexible copper braids release the stress from the contraction ($\sim$ 2-3 mm) in the process of cooling down and the copper blocks serve as contact surfaces. A pair of nickel coated copper thermal radiation shields (made by Cryomech) are attached to the refrigerator first stage cold surface to shield the target cell from room temperature radiation. The thermal radiation shields have rectangular windows where 0.16 mm thick aluminum foils have been attached as part of the electron exit windows. Detailed information on the dimensions of the radiation shields and the way they are attached to the refrigerator first stage cold surface are found in [47]. Two carbon-glass temperature sensors (Lakeshore CGR-1-3000) are mounted on the target to monitor the target temperature with one mounted close to the transfer tube and the other mounted on the end of the target cell. The average of the two readings gives the target temperature. The temperature readouts are controlled by the Lakeshore Cryogenics temperature controller (Model DR-82C). The carbon glass temperature sensors are chosen for their insensitivity to radiation damage. The pair of sensors used in the present work were used previously in Bates experiment 88-02 [6] four years ago and were recalibrated by Lakeshore Cryogenics after Bates experiment 88-02. The calibration curves are very close to those obtained prior to that experiment.

The aluminum scattering chamber was made by Cryomech as part of the refrigerator system. The side flanges have 0.25 mm-thick aluminum windows to allow the scattered electrons to exit the scattering chamber without too much energy loss. The refrigerator is mounted on the bottom of the scattering chamber directly below the center of the target cell. The vacuum feedthrough for the signals from the temperatures sensors is also connected to the bottom of the scattering chamber. Detailed description on the dimensions and machining of the scattering chamber is given in [47]. As it is very important to have only non-magnetic material in the target area, all the screws used for the target, thermal radiation shields and the scattering chamber are made of either copper or brass.

A pair of Helmholtz coils is used to provide the magnetic field that defines the

^{3}He nuclear spin direction. The Helmholtz coils employed are water-cooled and are capable of operating at a field up to 200 gauss. The center of the Helmholtz coils is set between the pumping cell and the target cell, with the pumping cell closer to the center of the Helmholtz coils as the pumping cell is at room temperature where the relaxation due to the magnetic field gradients is more significant than at low temperature. A detailed description of the dimensions and construction of the Helmholtz coils is found in [47]. The coils were operated at 60 A, providing a field of 36 guass, with water cooling during the experiment. Four thermal switches were attached to the cooling water lines on the coils to trigger the interlock on the Helmholtz coil power supply. The pumping cell axis is oriented along the axis of the coils to an accuracy of $\pm 5^\circ$ restricted by glass blowing. The magnetic field direction was measured by aligning a Brunton Classic compass along the beam line using a transit, then reading the field direction from the compass. The magnetic field was aligned to the designed direction with both the Helmholtz coils and all the magnets of the two spectrometers powered up. It was found that the field direction changed by $\sim 1^\circ$ due to the background field from the spectrometers. The Helmholtz coils were rotated slightly to achieve the designed direction with the spectrometer magnets on.

For this experiment, the magnetic field alignment was more complicated than as described above, because a large magnetic field gradient from the MEPS spectrometer was seen when it was first turned on. The field gradient was so large that only ~ 60 seconds relaxation time constant for a single sealed cell in the position of the pumping cell of the target was measured. The relaxation measurement is discussed later in the section on the target performance. A holding field of 72 gauss (corresponding to 120 A) for the Helmholtz coils was chosen to minimize the spin-lattice relaxation effect from the background magnetic field. Over 1000 seconds relaxation time for the single sealed cell was achieved with a 72 gauss holding field and the spectrometers on. The magnetic field was aligned to the designed 44.3° to the right of the electron beam under this condition. The polarized ^{3}He target was then installed on the pivot, the whole beam line was pumped down, and the copper target

cell was cooled down. The target was then tested before putting beam onto it and problems were found. Very short relaxation time constants in the cold target cell ($\sim$ 12 K), about 500 seconds, were measured. The cold target cell had been tested on the bench to have a relaxation time of 1400 seconds at a holding field of 18 gauss before the installation. A relaxation time constant longer than 1200 seconds on the cold target cell is required with no beam on in order to achieve a sufficiently long relaxation time in the target cell with beam on to perform the experiment. The relaxation mechanisms have been discussed in detail in [47] and will be discussed in Section 3.5.1. Tests were done with the magnetic spectrometers off and a holding field of 18 gauss, and the copper target cell was measured to have a relaxation time constant of $\sim$ 1400 seconds. The final optimum holding field setting was chosen to be 36 gauss with field clamps mounted onto the front surface of the MEPS first quadrupole to minimize the spin-lattice relaxation due to the background field gradient from the MEPS spectrometer to the pumping cell. Over 1200 seconds was achieved for the cold target cell relaxation time constant with this new holding field and with both the spectrometers on. The magnetic field direction was re-measured after the experiment under the same condition as data were taken and the actually field direction was found to be 42.5° to the right of the electron beam line with an accuracy of $\pm 0.5°$. It was not understood why the cold target cell relaxation time constant became shorter as the holding field was increased, although one possible explanation could be that there is some magnetic impurity in the close vicinity of the copper target cell, for example the nickel coating on the thermal radiation shields, which might cause significant spin-lattice relaxation as the holding field is increased.

The polarized ^{3}He target discussed here has several features which are different from the one described in the previous work [47]. First of all the pumping cell is much bigger, 2.5 in (O.D.) by 6 in (long) as compared with 2 in (O.D.) by 4 in (long). The larger cell was chosen because better pumping rate and polarization can be achieved with the LNA laser system.

A dilute solution of "bright dip", a mixture of hydrofluoric, nitric and sulphuric

acids, is used for cleaning the copper target cell which is more reliable than HF used previously. Although concentrated "bright dip" is actually quite dangerous, it does not have some of the special risks of HF. The "recipe" for mixing the bright dip acid can be found in appendix A. It is also found that baking the glass pumping cell for $24 - 48$ hrs. under vacuum is good enough for efficient optical pumping which corresponds to the condition of a good vacuum of $\sim 1 \times 10^{-7}$. This also differs slightly from the technique used previously for cleaning the pumping cell which required cycling hot discharge after $24 - 48$ hrs. of baking under vacuum. This feature is largely related to the powerful LNA laser used for this target.

A different kind of copper braid block is used for attaching the target cell to the refrigerator cold surface, avoiding the problem of additional stress caused by the original design. The braids used are more flexible and less work-hardened compared with the group of copper wires used before. The target is very robust and the problem with breaking glass has been solved using this new type of braid blocks.

Indium foils have been placed in between all the thermal contacting surfaces and a helium leak in the refrigerator system has been discovered and fixed. These resulted in a lower operating target temperature $\sim$ 13 K compared with $\sim$ 17 K obtained previously, making this target 30% more dense.

Target polarization is determined with higher accuracy ($\pm 3\%$) than in the experiment of Jones *et al.* ($\pm 10\%$) [6]. We have performed an NMR calibration of optical measurement of ^{3}He nuclear polarization [63] with an accuracy of $\pm 2\%$ after the previous experiment (see Section 3.4). Lastly and most importantly, a different type of laser crystal, LNA, has been used in this work which resulted higher average target polarization achieved in the present work (over 38% with $25\mu A$ average beam current). The LNA laser system will be discussed in detail in Section 3.3.

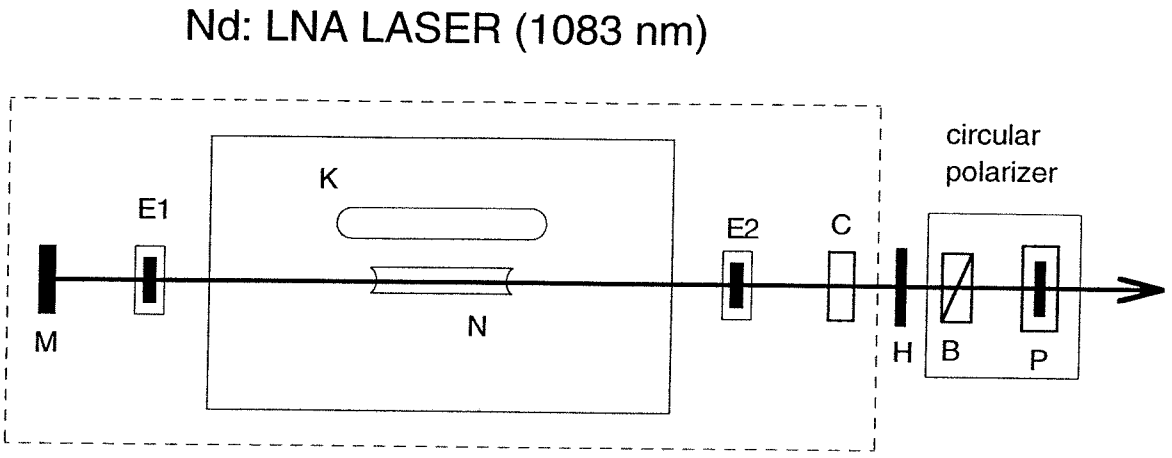

Figure 3.5: Schematic diagram of the laser system and the polarizing optics. (M) end mirror; (E1) 0.3 mm etalon; (N) curved LNA rod; (K) Krypton arc lamp; (E2) 1.0 mm etalon; (C) output coupler; (H) half-wave plate; (B) beam-splitter cube; (P) Pockels cell.

3.3 The LNA Laser System

The LNA laser system was developed at Caltech [55] following the work of M. Leduc and co-workers [60]. The laser system is simple to construct and easy to operate. A neodymium-doped lanthanum magnesium hexaluminate (LNA) crystal antireflection coated at 1083 nm replaces the YAG crystal in a Laser Applications Model 9560 laser. The LNA laser is pumped by a krypton arc-lamp. Two étalons are added to the laser cavity for tuning and bandwidth reduction. The two étalons used in the laser system for the ^{3}He target are 0.3 mm-thick and 1.0 mm-thick which result in a linewidth that matches well to the 2-GHz Doppler profile of the ^{3}He atoms. The laser can be tuned by tilting the étalons or varying their temperatures. Fig. 3.5 shows the schematic diagram of the laser system and the polarizing optics.

The LNA rod is 4-mm-diameter by 79-mm-long, grown along the a axis and doped with $\sim$ 15% Nd. It was purchased from Union Carbide. The typical beam shape is elliptical because of asymmetry in the thermal conductivity along the b and c axes [64]. This ellipticity of the laser beam shape has been improved with the recent development of rods grown along the c axis [65]. The rod ends are cut with concave curvature (R= 60 cm) to compensate for the thermal lensing effect which is

caused by the heating of the rod from the intense light of the arc lamp. The outside of the rod is water cooled, so a temperature gradient develops in the rod that results in a gradient in the index of refraction. The rods acts like a converging lens with a focal length that shortens as the current on the arc lamp is increased. If the lamp power is sufficiently high to cause a focus inside the laser cavity, not only the laser power drops but the rod can also break from the thermal stress. There are usually signs shown before this disaster happens: the laser beam shape begins to deteriorate, the laser needs substantial realignment to maximize the power and the increase of the laser power saturates as the lamp current is increased. The approach is taken to use the shortest laser cavity as possible, as well as using a curved rod to minimize the thermal lensing effect. The cavity is 36 cm long with 28 cm being occupied by the commercial laser head.

A partially reflecting mirror with a reflectivity of 99.0% is used at one end of the laser as the output coupler with the other end being a completely reflecting mirror. Highest laser power is obtained with the two mirrors placed symmetrically about the LNA rod. The LNA laser is tunable around 1.05 μm and 1.08 μm. In order to tune the laser to the ^{3}He transition wavelength of $\lambda = 1.0834$ μm, two étalons, one 0.3 mm thick and one 1.0 mm thick are inserted into the laser cavity. These two étalons serve as laser tuning elements as well as linewidth reduction elements. The étalons can be tuned by either tilting the angles or varying their temperatures. It is not ideal to tune the étalon by tilting its angle away from normal incidence because the reflected waves from the two surfaces of the étalon interfere less effectively which results in lower laser power and deterioration of the beam shape. An alternate approach following the work of Larat [66] is taken by positioning the étalon near normal incidence and varying its temperature for tuning. If the temperatures of the étalons are stabilized, this tuning approach also eliminates the frequency drift of the laser caused by the drift of the temperatures of the étalons. The étalon heater is a homemade system consisting of a copper block that surrounds the étalon, a resistive wire heater, and a feedback circuit to regulate the temperature. The heater

is 2.5 cm long and rests on a 3.5-cm-diameter rotation stage (Ealing Electro-Optics Model 37-0502), allowing the end mirrors of the laser to be only 4 cm from the laser head. The étalons can also be tuned by tilting their angles remotely using the two motordrives (Ealing Electro-Optics Model 37-0221) controlled by the motor drives control units (Ealing Electro-Optics Model 37-0031) which are mounted on the two rotation stages where the étalon heaters sit. During the experiment the laser was tuned primarily by varying the étalon temperatures using the étalon temperature controllers which were shielded well in the experimental hall. Minor tuning of the laser was realized by the remote tuning of the étalons using the motordrive controller upstairs in the counting bay.

A sealed ^{3}He cell with a pressure of 0.8 torr is used as a tuning cell to monitor the fluorescence signal from the ^{3}He atoms. The cell is placed after the laser end mirror with a tiny fraction of the laser light passing through it and a weak rf discharge is maintained in the cell to excite metastable ^{3}He atoms. A Hamamatsu R316-02 phototube, sensitive to 1.08 μm light, views the tuning cell from a position with the tube's axis perpendicular to laser beam. A collimator is placed between the cell and the phototube to minimize the amount of the direct scattered laser light from the wall of the cell seen by the phototube. The tuning signal is monitored on a oscilloscope. When the laser is tuned to the frequency corresponding to the ^{3}He transition $2^3S_1 \rightarrow 2^3P_0$, a large signal can be seen on the scope which corresponds to spontaneous emission of the ^{3}He atoms that were excited to the 2^3P state by the laser light. This signal can be easily distinguished from the background light, and C8 and C9 can be identified from each other clearly for the LNA laser.

The laser light coming directly from the laser cavity is linearly polarized. It is circularly polarized using a polarizing beam-splitter cube followed by a Pockels cell. A multiple order quartz half-wave plate at $\lambda = 1083.4$ nm, antireflection coated at the same wave length, is placed between the laser cavity and the beam-splitter cube to maximize the laser power after the Pockels cell. The helicity of the laser light is changed by varying the high voltage applied to the Pockels cell, and the target spin

can be flipped easily by this means. To minimize systematic uncertainties in the asymmetry measurements, the target spin was flipped a few times a day during the experiment by remotely varying the applied high voltage of the Pockels cell.

With the laser system discussed above, typical operating parameters for the lamp power are 1.0 kW for the laser threshold and 1.8 kW for 6 W output. The two transitions C8 and C9 can be separated from each other easily and a laser linewidth of 1.5-GHz is obtained with the combination of the two étalons. Pumping rates of 10^{18} (10^{19}) atoms/s with 82% (50%) polarizations are achieved on a single sealed cell with this laser under ideal conditions [55]. Careful study of the pumping rates vs. ^{3}He gas pressures, discharge frequencies, discharge intensities, laser intensities and cell sizes for C8 and C9 using this LNA laser system have been done on single sealed pyrex glass cells [55]. The polarized ^{3}He target for the present work was chosen to operate at a gas pressure of $\sim$ 2.0 torr, a discharge frequency of 200 KHz or 2 MHz, and a pumping cell size of 2.5-in-diameter by 6-in-long using the transition line of C9 based on the study mentioned above.

The laser system was installed in a hut shielded by heavy concrete blocks and lead bricks to prevent radiation damage to the laser crystal and the polarizing optics. A retroreflector was placed after the pumping cell to double the velocity groups of the metastable atoms interacting with the pumping light for maximum pumping efficiency. A filter (Kodak Wratten 87B) was placed in front of the retroreflector to avoid reflection of the 668-nm light used for the polarization measurement. This filter absorbed the 668-nm light but transmitted the optical pumping light. The laser power was lower (3 Watts) as compared with the typical laser power obtained by Gentile *et al.* [55] which may have been caused by the dirty environment in the experimental hall. The laser power decreased over time and the optics required cleaning once every two days. A laser shutter was installed in front of the laser hut which can be controlled remotely to start or stop optical pumping. The laser beam was confined inside the hut with shutter closed for safety.

In conclusion, the LNA laser has several significant advantages over the YAP laser

used previously for metastability-exchange optical pumping of ^{3}He: higher power (over 3 Watts), a linewidth that matches well to the Doppler profile of the ^{3}He atoms, several longitudinal modes within this bandwidth, and good spectral overlap with the optical pumping transition. It is also easy to construct and operate. Its stability and easy tuning make it an ideal laser system for polarizing ^{3}He nuclear targets.

3.4 NMR Calibration of Optical Measurement of ^{3}He Nuclear Polarization

Optical measurement of ^{3}He nuclear polarization involves detection of the circular polarization of a ^{3}He atomic transition line chosen for the optical measurement. The ^{3}He nuclear orientation is partially transferred to electronic orientation due to hyperfine coupling. A relation exists between the detected circular polarization of the atomic transition line and the ^{3}He nuclear polarization, but this relation is pressure dependent because part of the electronic polarization is lost due to collisions. This measurement requires a weak rf discharge to excite ground state atoms to excited states. The optical measurement technique does not perturb the target and can monitor the polarization continuously during data acquisition. However, it is not a direct measurement of the nuclear polarization. Precise calibration of the optical measurement is necessary for polarization experiments where an accurate knowledge of the target polarization is required. The 668-nm light corresponding to the ^{3}He transition of $(3^1D \rightarrow 2^1P)$ is the line commonly chosen for the optical measurement of ^{3}He nuclear polarization because of its spectroscopic strength. In this section we will discuss the optical measurement using the 668-nm line of the ^{3}He nuclear polarization first, and then the NMR calibration of this optical measurement.

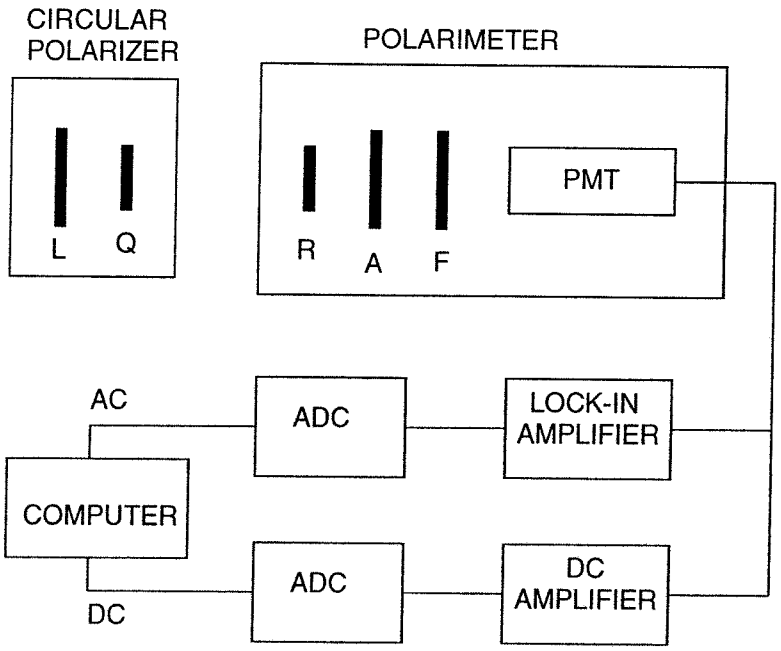

Figure 3.6: Schematic diagram of the optical polarimeter.

3.4.1 Optical Measurement of ^{3}He Nuclear Polarization

An optical polarimeter is used to detect the circular polarization of the 668-nm line to measure the ^{3}He nuclear polarization. The polarimeter consists of a rotating quarter-wave plate (R) for 668 nm, a linear polarizer (A), an interference filter (F) and an Amperex XP2023B phototube. The rotating quarter-wave plate at a rotation frequency of f converts the incoming circularly polarized light from the cell into linearly polarized light, which is transmitted maximumly through the linear polarizer following the quarter-wave plate at a frequency of 2f. The interference filter placed behind the linear polarizer and before the phototube transmits only 668-nm light. The signal from the phototube is sent to a lock-in amplifier to measure the ac component of the signal at the 2f frequency, and a dc amplifier to amplify the dc component. The output of each amplifier is sent to a Kinetic Systems 3553 ADC, which is read by the target data acquisition program. A schematic diagram of the optical polarimeter is shown in fig 3.6.

The ^{3}He nuclear polarization is expressed in terms of the measured ac and dc

component of the 668-nm line as follows:

$$P_{nuc} = f_{pressure} \frac{f_\theta}{\cos\theta} \frac{V_{ac}}{V_{dc}} \tag{3.4}$$

where V_{ac} is the ac component of the phototube signal measured by the lock-in amplifier, V_{dc} is the dc component amplified by the dc amplifier, $f_{pressure}$ is the pressure factor which relates the circular polarization of the 668-nm line to the ^{3}He nuclear polarization, and θ is the angle of the axis of the optical polarimeter relative to the magnetic holding field, $\vec{\mathbf{B}}$. The pressure factor $f_{pressure}$ will be discussed in Section 3.4.2. An accurate determination of the target pressure is necessary for its polarization measurement and is discussed in [47]. $f_\theta/\cos\theta$ is the correction factor [47] that accounts for the polarimeter being off-axis from the nuclear spin direction. The polarimeter was at an angle of 14° with respect to the target spin direction and f_θ was determined to be 1.05 experimentally for the present work.

The optical polarimeter is calibrated by placing a circular polarizer in front of it. It consists of a linear polarizer (L) followed by a quarter-wave plate (Q) with the angle between the axis of the polarizer and the optical axis of the quarter-wave plate being 45°. The polarimeter was calibrated to measure 99.8% circular polarization with the circular polarizer in front to an accuracy of ±0.5% for the present work.

3.4.2 NMR Calibration of the Optical Measurement of ^{3}He Nuclear Polarization

The optical measurement of ^{3}He nuclear polarization was calibrated previously in the early 1970s by Pinard and Van Der Linde [67] using absorption of the pumping light from a ^{4}He lamp. The pumping light absorption technique works in the following way: as optical pumping light polarizes the sample, the pumping light absorbed by the metastable atoms decreases as the polarization of the sample increases because the population in the metastable state shifts to the magnetic sublevels that do not

interact with the pumping light. So utilizing the change in the absorbed pumping light, this technique actually measures the metastable polarization, which should be equal to the ground state polarization as these two quantities are closely coupled through rapid metastability-exchange collisions. Because the accuracy of these measurements was not quoted in [67] and was subject to systematic uncertainties due to lack of knowledge of the spectrum of the lamp, an NMR calibration has been performed at Caltech which calibrated the optical measurement to an accuracy of $\pm 2\%$. A calibration against the pumping light absorption technique using a diode laser-pumped LNA laser has been performed by Bigelow, Nacher, and Leduc [68] concurrently with the Caltech work. The two recent calibrations are consistent with one another. However, only the Caltech NMR calibration will be discussed here.

To avoid systematic uncertainties associated with an absolute NMR measurement, the ^{3}He signal is compared with the signal from an identical water sample. The polarization for water is known from the Boltzman distribution. The NMR measurements are performed using the technique of adiabatic fast passage (AFP). The advantage of this technique is that the line shape of the NMR signal is identical for ^{3}He and water, which is ideal for the case of a direct comparison.

Adiabatic Fast Passage

Adiabatic fast passage (AFP) refers to a technique to reverse the direction of a macroscopic magnetization with respect to a static magnetic field. Let's consider the effect of an oscillating rf magnetic field $\vec{B}_x = 2B_1 \cos\omega t\, \hat{x}$ applied to a sample which is in a static magnetic field $B_0\hat{z}$. The lab frame is defined by the $(\hat{x}, \hat{y}, \hat{z})$ coordinate system. In a rotating frame $(\hat{x'}, \hat{y'}, \hat{z'} = \hat{z})$ with an rf frequency of ω, B_x can be decomposed into two components: a stationary part and a part rotating at a frequency of 2ω. Under the conditions of the NMR measurements discussed here, the latter part can be neglected as it is not resonant. The effective field in the

rotating frame can be written as:

$$\vec{B}_e = \left[B_0 - \frac{\omega}{\gamma}\right]\hat{z}' + B_1\hat{x}', \tag{3.5}$$

where γ is the gyromagnetic ratio ($\gamma_p/2\pi = 4.26$ kHz/G for protons in water and $\gamma_h/2\pi = 3.24$ kHz/G for ^{3}He). If initially the static field is far enough away from ω/γ so that $|B_o - \omega/\gamma| \gg B_1$, then $\vec{B}_e$ and the magnetization $\vec{M}$ are oriented nearly along the $\hat{z}'$ axis in the rotating frame. If the static field is ramped through resonance ($B_0 = \omega/\gamma$), the effective field rotates away from $\hat{z}'$ axis towards $-\hat{z}'$ and carries the magnetization vector along with it. The effective field can be expressed as $\vec{B}_e = B_1$ $\hat{x}'$ at resonance. The adiabatic condition means that the ramping rate is slow enough that the magnetization follows the effective field and the "fast" condition means that the relaxation effects can be neglected during the time of passage through resonance. These two conditions for AFP are given by

$$\left|\frac{dB_o}{dt}\right| \ll \gamma {B_1}^2, \tag{3.6}$$

$$\frac{1}{B_1}\left|\frac{dB_o}{dt}\right| \gg \frac{1}{T_1}, \frac{1}{T_2}, \tag{3.7}$$

where T_1 and T_2 are the longitudinal and transverse relaxation times respectively. In our system, the transverse relaxation time is dominated by dephasing of the individual precessing spins due to gradients in B_o. If the inhomogeneity in B_o across the sample is much smaller than the size of the rotating field B_1, then the transverse relaxation time can be neglected in Eq. (3.7) [69] [70]. There are two ways to do an adiabatic fast passage measurement, one can either ramp the static magnetic field to go through resonance or vary the rf frequency to go through resonance. The first approach is used for the NMR calibration discussed here since a tuned circuit can be used to amplify the small water signal for a system with a fixed rf frequency.

As $\vec{M}$ slowly reverses direction, it is also precessing rapidly in the lab frame at

rf frequency ω. If a pick-up coil is placed in the xz plane, an induced ac voltage of amplitude $\mathcal{E}$ can be detected due to this precessing magnetization. $\mathcal{E}$ is given by

$$\mathcal{E} = -NQ\frac{d\Phi}{dt} = -NQ\omega\Phi, \tag{3.8}$$

where Q is the quality factor of the tuned pick-up circuit and Φ is the magnetic flux through the pick-up coils with N turns.

Taking into account the small difference for the volumes ($\pm 2\%$) of the ^{3}He and water cells, the ratio of the amplitude of the induced ^{3}He signal to that of water is given by

$$R = \frac{\mathcal{E}_o^h}{\mathcal{E}_o^p} = \frac{(Q\omega P_n n V \mu)_h}{(Q\omega P_n n V \mu)_p}, \tag{3.9}$$

Where P_n is the nuclear polarization, n is the number density of spin 1/2 particles with magnetic moment μ, and V is the volume of the cell. The subscripts h and p denote ^{3}He and water (protons) respectively. The nuclear polarization P_n is defined by

$$P_n = \frac{n_+ - n_-}{n_+ + n_-}, \tag{3.10}$$

where n_+ and n_- are the number densities for the two eigenstates of the spin 1/2 particles with respect to the $\hat{z}$ axis. The nuclear polarization for the protons in water based on the Boltzmann distribution is approximated with sufficient accuracy by

$$P_n^p = \frac{\mu_p \omega_p}{K T_p \gamma_p}, \tag{3.11}$$

where μ_p is the proton magnetic moment in water, K is the Boltzmann constant, and T_p is the temperature of the water cell at the time of the NMR measurement. The ^{3}He density can be expressed in terms of the pressure p_h and temperature T_h at the time when the cell is sealed off. Finally, p_n^h can be written in terms of the

known quantities and the measured quantities as

$$p_n^h = \frac{(QV\omega^2\mu^2)_p}{(QV\omega\mu)_h}\frac{n_p T_h}{\gamma_p T_p p_h}, \tag{3.12}$$

with the small volume difference between cells being taken into account.

Free Induction Decay

The adiabatic fast-passage technique discussed above is most suitable for the kind of NMR measurement discussed here. Another type of technique, free induction decay (FID), is also useful for providing additional information about the NMR system. This technique works in the following way: a static field is fixed and an rf pulse is applied to the sample at the Larmor frequency. In the rotating frame the effective field is $B_e = B_1\hat{x'}$ and the magnetization precesses around the $\hat{x'}$ axis at the angular frequency of γB_1. The magnetization is rotated by $\gamma B_1 \tau$ with τ being the duration of the rf pulse. B_1 was determined by measuring the pulse length required for rotating the magnetization by $\pi/2$ which is easily accomplished in the case of helium by monitoring the optical polarimeter signal dropping to zero.

After the rf pulse the magnetization precesses freely and decays due to the inhomogeneity in B_0. The temporal behavior of the decay is given by the Fourier transform of the spectral distribution of Larmor frequencies for the water case. The timescale of the decay is roughly $\gamma_p \Delta B_0{}^{-1}$ which is the time required for a spread of 1 mrad in the distribution of accumulated phase of the Larmor precessing of the individual spins. This decay timescale can be used to estimate the inhomogeneity in B_0 (ΔB_0) of the NMR system across the sample to test the fast passage condition for the system. A Water sample was used for this purpose because there was a motion-narrowing [71] effect in the helium case which resulted in a much longer decay time than that of water.

NMR Experimental Apparatus

The experimental apparatus for the NMR system is shown in fig 3.7. A cylindrical pyrex cell, 5.0-cm-diameter by 5.7-cm-long, filled with ^{3}He or water is placed in a homogeneous magnetic field $B_o\hat{z}$ produced by a pair of 30-cm-radius Helmholtz coils. The cylindrical axis of the cell is along the $\hat{z}$ direction. An rf driving field $B_1\hat{x}$ is generated by a pair of 14.8-cm-radius Helmholtz driving coils placed in the yz plane. A pair of rectangular pick-up coils, 6.9-cm-long by 6.2-cm-wide, separated by 5.6 cm, surround the pyrex cell with their axes in the $\hat{y}$ direction. Each pick-up coil has 400 turns.

For an accurate measurement of small signals from water and low gas pressure ^{3}He ($\leq$ 0.2 torr), care is taken to minimize the systematics from vibrational noise and electromagnetic noise. The NMR system is encased in an aluminum box with a thickness of 1.6 mm to shield out electromagnetic fields. Shock absorbers, styrofoam and springs are used underneath the aluminum box to minimize mechanical vibrations.

^{3}He gas was polarized by optical pumping with an LNA laser as described in section 3.3. The circularly polarized laser light was incident along the $\hat{z}$ axis onto the ^{3}He cell through a 9-cm-diameter opening in the front of the aluminum box. The 668-nm line from the ^{3}He cell used for optical measurement exits through this opening and is detected by an optical polarimeter described in section 3.4.1 which is located 6° off the $\hat{z}$ axis in the xz plane and 95 cm from the cell. An rf high voltage (0.1 - 20 MHz) applied to a pair of aluminum foil strips taped around the outside of the cell generated a weak electrical discharge in the helium cell. The discharge was turned off during NMR measurement because it produced substantial rf interference on the NMR signal caused by the contact between the aluminum discharge strips and the metal electrodes in the pick-up coil support. The relaxation of the polarization is less than 0.2% during the time required for NMR measurement with the discharge off. A preamplifier placed close to the aluminum shielding box is used to amplify

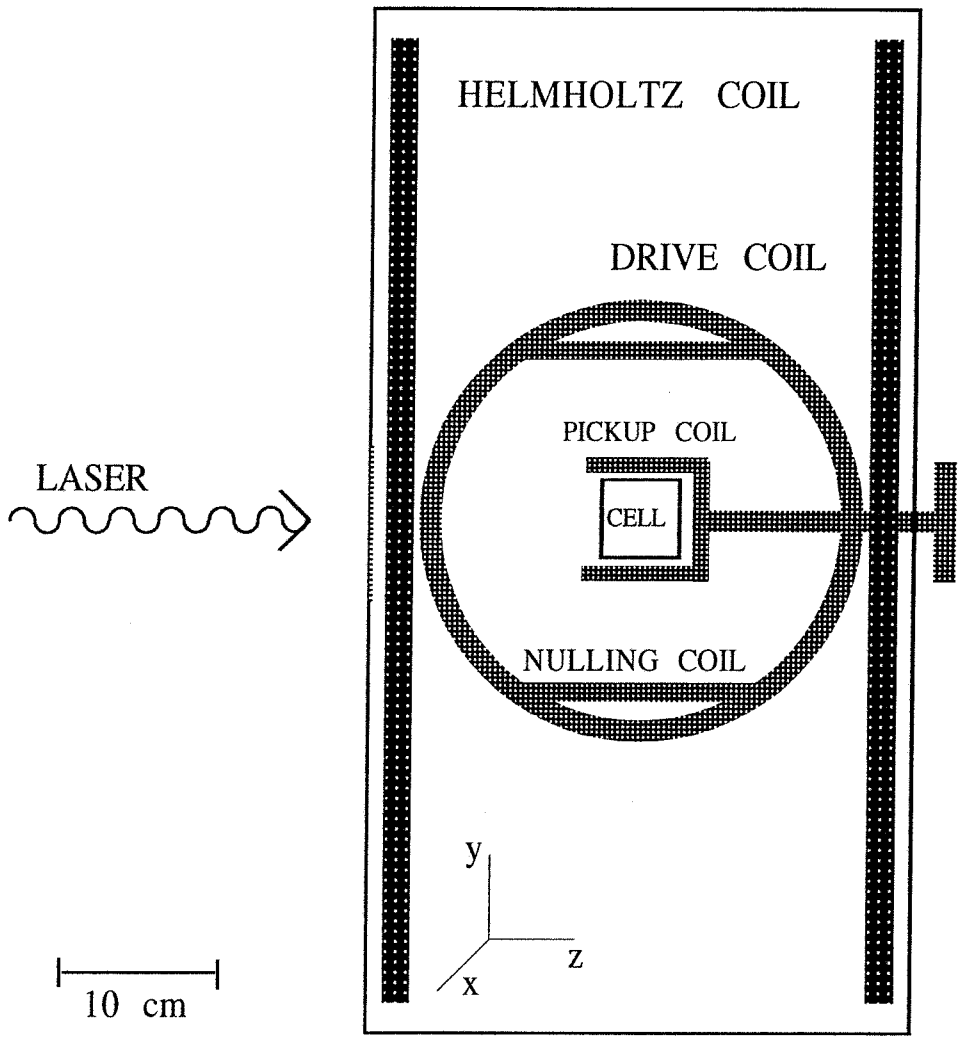

Figure 3.7: Scale diagram of the NMR apparatus.

the pick-up signal. The amplifier input is grounded whenever the discharge is on to avoid overloading it.

A block diagram of the NMR electronics is shown in Fig. 3.8. An HP function generator, tuned to the resonant frequency ($\omega/2\pi$ =96 KHz) of the pick-up coil system, produces an rf current in the driving coils. The static magnetic field B_o is ramped in 1 s from 2 gauss below to 2 gauss above the atomic resonant condition (ω/γ_h=29.6, ω/γ_p=22.5 gauss). The current in the Helmholtz coil is converted into voltage, digitized by a Kinetic transient digitizer 4010, and stored in the computer. The induced voltage in the pick-up coil is amplified by a factor of 100 using a preamplifier and then sent to a lock-in amplifier (EGG 5010) together with a frequency reference signal from the function generator. The two outputs of the lock-in amplifier, one in phase with the reference signal and the other 90° out of phase, are squared and summed before they are digitized and stored in the computer.

The pick-up coil must be mounted normal to the driving coil to minimize the crosstalk between the pick-up and the driving coils. The pick-up coil was mounted in such a way that it could be rotated around the $\hat{z}$ axis from outside of the aluminum box as shown in Fig. 3.7. The residual signal in the pick-up coil is nulled by applying a phase shifted voltage to the nulling coil. The quality factor Q of the tuned pick-up circuit is measured by sweeping the frequency of the nulling coil voltage from 60 to 120 kHz and measuring the linewidth of the response of the pick-up coil. The typical measured value of Q was 60, with variation of $\pm 5\%$ from cell to cell and $\pm 0.7\%$ on a given cell. The Q and the resonance frequency were measured on each day that the data were acquired and the resonant frequency was found to vary $\pm 0.2\%$ from cell to cell. The electronics was found to be linear to within $\pm 1\%$ using a test pulse which was a sine wave packet with a variable width between 0.5 and 20 ms. The linearity of the electronics is crucial for an accurate NMR calibration because the water signal differs that of helium by as much as a factor of 70.

Each ^{3}He cell was prepared according to techniques that are described elsewhere [39]. Briefly, each cell was evacuated to below 10^{-7} first, then cleaned by baking

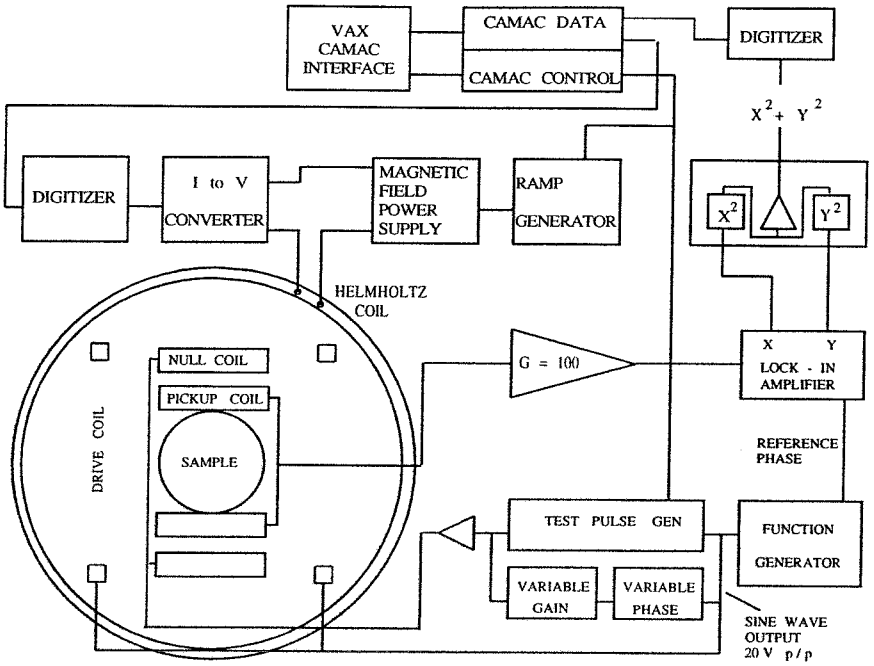

Figure 3.8: Block diagram of the NMR electronics.

overnight at a temperature of $\sim$ 400K and further cleaned by a hot discharge. The cell volume was measured with an uncertainty of $\pm 0.2\%$ by filling the cell with alcohol before it was mounted to a vacuum system. The cell volumes are around 90 cm^3 with a variation of $\pm 2\%$ from cell to cell. The cells were filled with 99.995% pure ^3He gas. When a cell was sealed off, the pressure in the vacuum manifold and the ambient temperature were measured. A small vacuum manifold was used to fill cells with pressures other than 3 and 5 torr after it was discovered that the cell pressure was lower than the original pressure and the remaining pressure in the manifold was higher after sealing off the cell and allowing the system to cool. For cells at 3 and 5 torr, there is a $2.8 \pm 1.5\%$ pressure correction associated with the filling procedure. Measurements of the pressure correction and the two filling procedures are discussed in [63].

Measurement

The adiabatic fast-passage conditions discussed previously are satisfied in the present NMR system for both the water and helium sample. The driving field B_1 was determined to be 35 ± 1 mG using the technique of free induction decay. Hence the sweep rate dB_0/dt of 4G/s is about seven times smaller than $\gamma {B_1}^2$. T_1 and T_2 are both 3.6 s for water [72], so $1/T_1$ and $1/T_2$ are both 400 times smaller than $(dB_0/dt)/B_1$. For ^{3}He T_1 is typically a few thousand seconds. The inhomogeneity in B_0 across the sample, ΔB_0, was determined to be 1mG from the observed 30-ms decay time of the FID signal for water. Hence ΔB_0 is about 35 times smaller than B_1.

The measurement on each ^{3}He cell proceeded in the following way: the helium was polarized using metastability-exchange optical pumping technique with an LNA laser and the polarization was monitored by an optical polarimeter described previously. To minimize the scattered light seen by the polarimeter, the outside of the cell was taped with black electric tape and the inside of the aluminum box was painted black. First the pick-up signal was minimized by rotating the orientation of the pick-up coil axis; then the resonant frequency of the tuned pick-up coil was found by maximizing the pick-up signal after its axis was oriented properly, while the frequency of the applied current to the driving coil was sweeping through the resonance; lastly the pick-up signal was further nulled using the nulling coil. All of these were done prior to polarizing the helium cell. After the helium polarization reached equilibrium, the optical measurement was started. To reduce the statistical uncertainty in the optical measurement to a negligible level, the optical polarization was averaged for 30 seconds before the NMR measurement. The NMR measurement started 10 seconds after the discharge was turned off and the laser shutter was closed. The helium NMR measurement takes $\sim$2 seconds, and the polarization relaxes $\sim$ 0.2% during this 12 seconds as the cell has a relaxation time of a few thousand seconds with discharge off. The NMR measurement of helium was taken on cells of pressure between 0.1

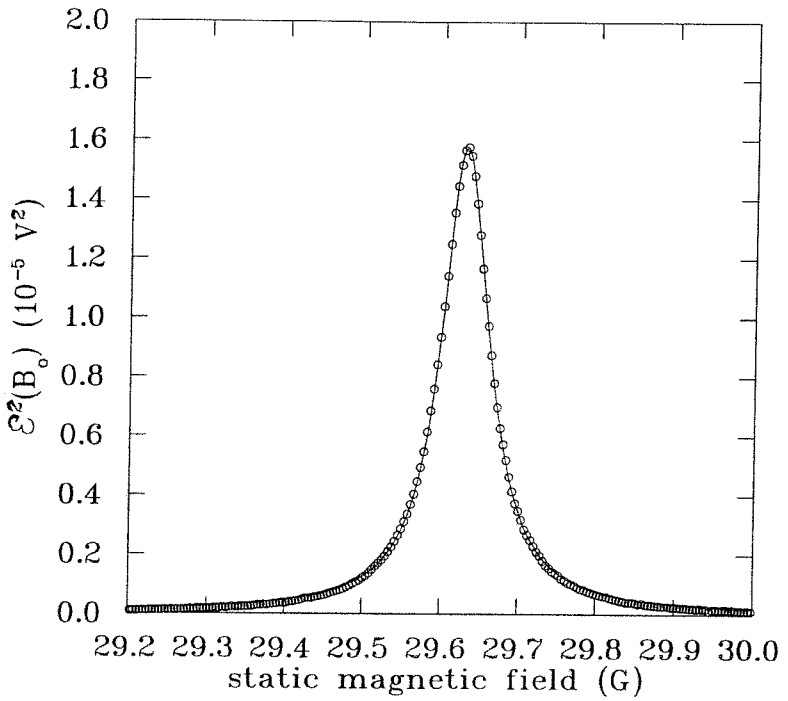

Figure 3.9: Adiabatic fast-passage signal for a 1.0-torr cell of ^{3}He (64% polarization).

torr and 5.0. Fig. 3.9 shows the adiabatic fast-passage signal for a 64% polarized, 1.0-torr cell of helium with a fit to a Lorentzian distribution.

The optical signal was also used to measure the AFP efficiency, i.e., the efficiency of the inversion of the polarization. AFP inefficiency is mainly a measure of the violation of the AFP condition caused by the magnetic field gradients seen by the atom as it moves across the sample. The effect of the field gradients for water is much smaller than that of ^{3}He. The AFP efficiency is defined as

$$\varepsilon = \frac{P_0 - P_f}{2P_0} \tag{3.13}$$

where P_0 and P_f are the polarizations before and after the sweep. Since the AFP efficiency is very close to one ($\varepsilon = 0.988$), P_f was measured after eight sweeps in rapid succession. The ^{3}He NMR signal height and the water NMR signal height were measured as a function of the AFP efficiency. The AFP efficiency was varied between 0.92 and 0.99 by introducing magnetic field gradients into the system. Empirical

quadratic fits were performed of the NMR signal height for ^{3}He and water versus the AFP efficiency. The measured ^{3}He NMR signal and the water signal were corrected by their AFP efficiencies using the empirical fits mentioned above. The correction due to the AFP efficiency to the ratio of the ^{3}He and water signals is found to be small, 1.003 ± 0.002. For an accurate NMR calibration of the optical measurement, a few corrections need to be applied to the optical signal which had been checked very carefully. The polarimeter was calibrated carefully using a circular polarizer on each day when NMR data were taken for helium. Uncertainties in this calibration had been investigated in detail in terms of the imperfections in the circular polarizer, the rotating quarter-wave plate inside the polarimeter, and the orientation of the circular polarizer. With a high quality quarter-wave plate in the circular polarizer and proper orientation of the circular polarizer being used, accurate calibration of the polarimeter was obtained [63]. A polarization offset which could be associated with the electrical noise in the system was measured each day when a helium NMR measurement was performed. This offset was corrected to the measured polarization using the optical polarimeter. The angle between the polarimeter axis and the direction of the magnetic holding field was measured carefully and the correction due to this off-axis orientation to the measured polarization was applied. Lastly, a correction was applied to the measured optical polarization because of its magnetic field dependence. The measured degree of circular polarization of the 668-nm light from the atomic transition decreases with increasing magnetic field because of the decoupling of the electronic and nuclear spins. This effect was measured [63] on cells of He pressures of 0.3 torr, 0.8 torr and 5.0 torr against a static field of 12 gauss and is show in Fig. 3.10. Corrections had been applied to the optical polarization for a 30 gauss holding field for the helium NMR setting based on the measurement mentioned above. NMR measurement was also performed on an unpolarized ^{3}He cell and it was found to be consistent with zero within $\pm 0.02\%$. In addition, the linearity of the ^{3}He NMR signal height versus optical polarization was also checked and the offset was found to be $(0.2 \pm 0.2)\%$.

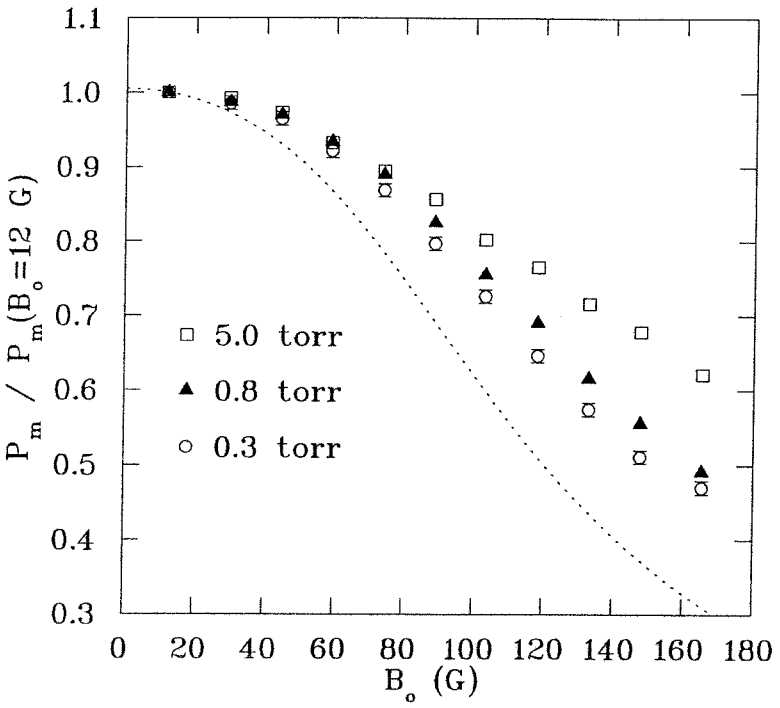

Figure 3.10: Magnetic field dependence of optical signal.

The NMR measurement for water is a little different from that for helium. Its signal is determined by the Boltzmann distribution and it is very small. At room temperature and B_o =22.5 G, the polarization of the protons in the water is only 7.6×10^{-9}. The induced voltage is 130 μV and 9-mV rms is detected by the lock-in amplifier after the induced signal is amplified by the tuned pick-up circuit and the preamplifier. Because of the 3.6-s longitudinal relaxation time on the water signal height and 1-s sweep time, the polarization at the time of passage through resonance is close to the value at the beginning of the sweep. Hence the signal height depends on whether the field is ramped from below or from above resonance. For these measurements, the field was ramped symmetrically both from below and from above the resonance so that the signal height corresponding to the polarization at resonance was obtained by averaging the signal heights from the two ramps. A 20 s interval between sweeps guaranteed equilibrium conditions. There is a slight uncertainty of $\pm 0.3\%$ in this averaging procedure due to non-linearity in the ramp.

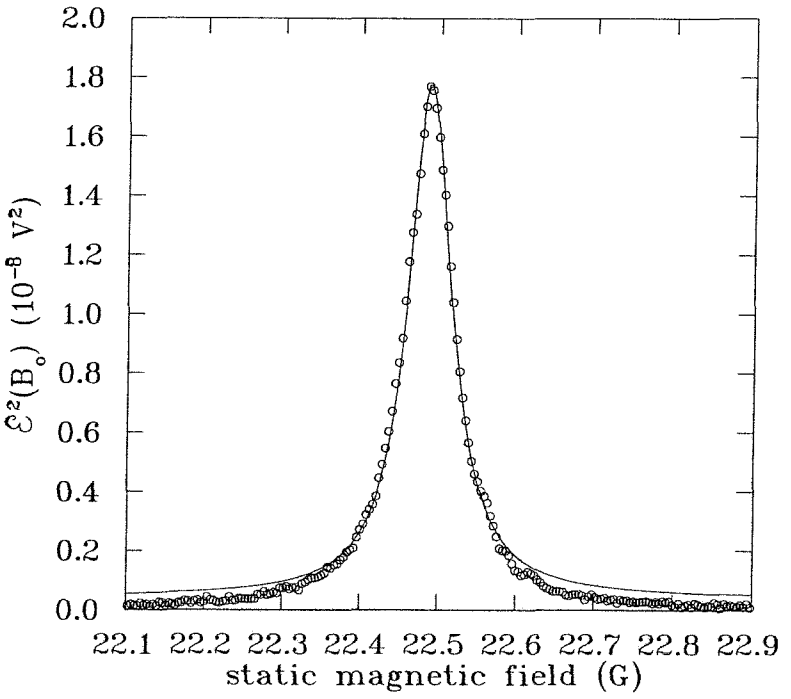

Figure 3.11: Adiabatic fast-passage signal for water.

To improve the signal-to-noise ratio of the water signal, data of 10 sweeps (five up, five down) were averaged with a correction applied to the peak positions first because of the small shifts in the starting time of the ramp ($\leq$ 2ms). Fig. 3.11 shows the adiabatic fast-passage signal for water with a Lorentzian fit to the data. The procedure of finding the proper orientation of the pick-up coil, finding the resonance frequency of the tuned pick-up circuit and nulling the pick-up signal are the same as those for helium described earlier. The water cell was also taped with black tape and aluminum foil strips in the same way as the helium cell to minimize systematic uncertainties. The measured water signal was also compared with a simple calculation which evaluated the water NMR signal by integrating the contributions to the induced signal from a magnetization distributed uniformly throughout the cell. A agreement was found within 20%.

Results

The theory of the pressure dependence of the degree of circular polarization of the 668-nm light used for optical measurement has been investigated by Pinard and Van Der Linde [67]. With P being defined as the degree of circular polarization of the 668-nm light emitted by the discharge and P_n as the nuclear polarization, they obtain the following expression for a $J = 2 \rightarrow J = 1$ transition:

$$\frac{P}{P_n} = \frac{3a^2(\Gamma + \gamma_2)/2}{(\Gamma + \gamma_2)(\Gamma + \gamma_1)^2 + 6a^2(\Gamma + \gamma_1)(\Gamma + 2\gamma_2/3)/\Gamma + a^2(\Gamma - \gamma_1 + 2\gamma_2)/4} \quad (3.14)$$

where Γ is the spontaneous emission rate for the transition, and γ_1 and γ_2 are the disorientation and disalignment rates, respectively. The constant a is the hyperfine coupling constant. $a\hbar\vec{I}\cdot\vec{J}$ is the hyperfine Hamiltonian with I being the nuclear spin angular momentum and J being the total electronic angular momentum.

The rates γ_1 and γ_2 are related to the corresponding cross sections σ_1 and σ_2 by $\gamma_i = n\sigma_i v_r$, where n is the number density of the ground-state atoms and v_r is the mean relative velocity of the two colliding atoms. Γ is replaced by $\Gamma' = \Gamma + n\sigma_0 v_r$ to account for other types of collisions that effectively destroy the 3^1D_2, where γ_0 is the total cross sections for these processes (σ_0 is labeled as $\sigma_0 + \sigma_e$ in [67]). The three cross sections $\sigma_i, i = 1, 2, 3$ are adjusted to reproduce the measured variation of P/P_n with pressure.

In the zero pressure limit, with $\gamma_{1,2} = 0$, Eq. 3.14 reduces to:

$$\frac{P}{P_n} = \frac{0.24}{(1 + \Gamma^2/\Omega^2)} \quad (3.15)$$

For the 3^1D_2 level, $\Gamma = 6.58 \times 10^7$ s^{-1} [73] and Ω, the hyperfine splitting in frequency, is 8.74×10^8 s^{-1} [74] which yields $P/P_n = 0.239$ at zero pressure. However, Pinard and Van Der Linde found the pressure dependence of P/P_n for the 3^1D_2 was inconsistent with the expected zero pressure limit. This inconsistency could be caused by the cascading effects from higher level ^1F states that would be manifested as an overall

p_h (torr)	P_n/P (data)	P_n/P (fit)	P_n/P [a] (fit)	Uncertainties fit (%)	Uncertainties systematic (%)
0.0998	5.67			0.5	4.5
0.207	6.42	6.42	7.3	0.4	1.9
0.299	6.78	6.78	7.5	0.4	1.9
0.499	7.42	7.33	8.0	0.3	1.9
0.800	7.94	8.02	8.7	0.3	1.9
1.010	8.37	8.43	9.3	0.3	2.1
1.977	10.09	9.97	11.6	0.3	2.1
2.92	11.38	11.42	13.8	0.3	2.5
4.85	14.98	14.98	17.8	0.3	3.1

[a] ref [68]

Table 3.1: Measurement of P_n/P as a function of p_h (for T_h= 297 K).

multiplicative correction for P/P_n above some critical pressure as explained in their paper. They found that they could fit their data above 0.15 torr using Eq.3.14 by introducing a normalization factor Z. The NMR results discussed here are fitted in the same way as that of Pinard and Van Der Linde.

The NMR measurements have been performed at pressures ranging between 0.1 and 5 torr. The data have been fitted in the way described in the previous paragraph for pressures above 0.2 torr. The data and the fit are shown in Fig. 3.12 as the ratio of the degree of circular polarization of the 668-nm light to the nuclear polarization, P/P_n, vs ^{3}He pressure, p_h, together with a fit of the data from [68]. In order to obtain an accurate calibration, uncertainties have been studied carefully in terms of two categories: fit uncertainty and systematic uncertainty. The fit uncertainty is the sum (in quadrature) of the typical uncertainties in the fitted values of $\mathcal{E}_o^p$ and $\mathcal{E}_o^h$. The total uncertainty is dominated by the systematic uncertainty, and the fit uncertainty is dominated by the $\pm 0.3\%$ uncertainty in the fitted value of $\mathcal{E}_o^p$. The systematic uncertainties have been divided into two groups: those uncertainties that can lead to day to day variations in the measurements on a given cell and those

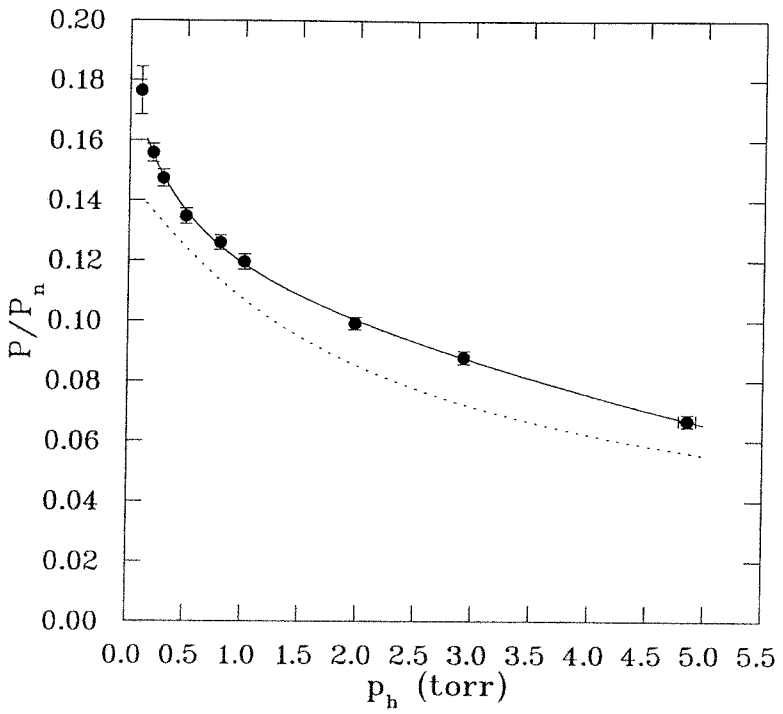

Figure 3.12: The NMR result: P/P_n vs. P_h.

that will not cause day to day variations. Detailed discussion on the systematic uncertainties of the NMR measurements is given in [63]. The data and the results of a fit using the procedure of Pinard and Van Der Linde as discussed in the text are listed in Table 3.1, where the inverse of P/P_n, P_n/P, is listed. The fit and systematic uncertainties are tabulated in Table 3.1 as well, and the values from a fit of the data in [68] are also listed in Table 3.1 for comparison.

3.5 Target Performance

The performance of a polarized target is very crucial for a nuclear physics experiment in which a polarized target is employed. Good target performance not only represents high polarization achieved on the target with beam incident, but also means stability over a long period of time. The performance of the polarized ^{3}He target employed in this work is related to many factors: the efficiency of the optical pumping light,

the discharge characteristics, the cleanliness of the pumping cell and the target cell, the relaxation mechanisms of the target system, etc. The relaxation mechanisms as well as the measurements of the relaxation time constants for this double-cell system have been studied and described in detail in [47]. They will only be discussed briefly here.

3.5.1 Relaxation Mechanisms for a Polarized ^{3}He Target

For spin depolarization, there are two general categories: spin-spin relaxation caused by the interaction of the magnetic moments of the neighboring atoms and spin-lattice relaxation from the coupling of the spins to the external fields. The relaxation from nuclear dipole-dipole interactions for ^{3}He is negligible for the temperature and pressure region where the polarized ^{3}He target discussed in this work was operated [49]. The dominant depolarization effects for a practical polarized ^{3}He target are from the spin-lattice relaxation, which can be divided further into the following four categories: magnetic field gradients, surface effects, discharge effects and beam effects.

The spin-lattice relaxation from magnetic field gradients is caused by the magnetic field gradients seen by the atom as it diffuses across the sample volume, which tends to alter the spin orientation. Detailed treatment for this type of the relaxation effect has been described by Schearer and Walters [75]. A generalized formula is given in [47] following the prescription in [75]. This depolarization effect from magnetic field gradients decreases as the sample temperature is decreased because the atom diffuses more slowly and consequently sees less field change. For the double-cell target system discussed here the target cell was operated at 12 K where the relaxation due to magnetic field gradients was not a concern. It is important to maintain a long enough relaxation time in the pumping cell that it can feed the target cell efficiently. The pumping cell is at room temperature where the dominant depolarization effects are from magnetic field gradients and the discharge effects. The pumping cell was

designed to have the optimized volume so that it can achieve high pumping rate and polarization with the LNA laser and at the same time maintain a sufficiently long relaxation time due to the magnetic field gradients from the holding field. Field clamps were mounted in front of the first quadrupole of one of the spectrometers (MEPS) during the experiment to minimize the background gradients from it, as discussed earlier in Section 3.2.

The ^{3}He nuclear polarization can be destroyed by interactions with atoms in the wall. The ^{3}He atoms maybe absorbed into or adsorbed onto the wall and interact with any magnetic impurities present when they diffuse into the wall. This type of depolarization mechanism is called a surface effect, and it is related to the specific surface chosen for the container. The depolarization processes for glass surfaces are fairly well understood in terms of two competing processes, one that dominates at high temperature and the other that dominates at low temperature. Permeation of the ^{3}He atoms into the glass surface is the primary depolarization process at high temperature, and adsorption of the atoms onto the wall is the dominant process at low temperature. At low temperature the surface effect becomes very important because the sticking time of the atoms onto the wall increases exponentially with the inverse of the wall temperature. A detailed description of the depolarization processes on glass surfaces is given in [47]. In the target system discussed here, the pyrex glass pumping cell was at room temperature where the surface effects are not significant. Depolarization on metal surfaces is not well understood. It is probably dominated by the adsorption onto the wall at low temperature. In particular, it is dependent on the cleanliness of the metal surface as well as the purity of the metal. The copper target cell discussed here was operated at 12 - 13 K, and a nitrogen coating was used to alleviate the surface depolarization effect [47]. The copper cell was cleaned chemically before assembling, and this cleaning process has been found to be very crucial.

In order to optically pump the ^{3}He atoms, a discharge must be maintained to create metastable atoms. The presence of the discharge causes depolarization be-

cause it creates other excited states, ions, and electrons as well as metastable atoms. All these additional species cause depolarization as they collide with the polarized ground state and metastable state atoms [76]. Depolarization from the discharge is the dominant depolarization source in the optical pumping cell. The optical pumping rate and the achievable polarization are dependent upon the discharge characteristics in addition to the efficiency of the pumping light. The discharge intensity is chosen for the pumping cell to have the optimized polarization and pumping rate for feeding the target, and a reasonably long relaxation time in the pumping cell with the discharge on, typically 3-5 minutes.

The beam effect is a dominant relaxation mechanism for atoms in the target cell where the polarized atoms are in direct contact with the electron beam. This depolarization effect was studied carefully in the early work on the development of the polarized ^{3}He target at Caltech [77] and further studied at Bates using an electron beam [47]. The depolarization effect due to the coupling of the polarized gas to the time-varying magnetic field generated by the Bates electron beam, which is a pulsed beam with frequency of 600 Hz and pulse width of 15 μsec, is negligible for a typical current of 10 - 40 μA. The main relaxation mechanism from the electron beam involves the creation of ions. Models are presented in [77] and [78] of spin relaxation from the ionization of the beam. Reference [76] contains information about the reactions between ground state helium atoms and the atomic and molecular ions. The average beam current for the present work was $\sim 25\mu A$ which contributed a relaxation time for the target cell of $\sim$ 1000 - 1500 sec as determined from the relaxation measurements taken during the experiment. It is clear from this that a sufficiently long relaxation time on the target cell without beam is necessary for a practical polarized nuclear physics target.

3.5.2 Target Relaxation Measurements

The relevant time constants associated with the double-cell target system are: the pumping cell relaxation time, the target cell relaxation time, the transfer time between the two cells, the diffusion time of the atoms in the pumping cell, and the diffusion time of atoms in the target cell. The first three time constants are important for extraction of the target polarization and will be discussed here. Solutions to the coupled pumping rate and relaxation rate equations for a double-cell system are given in [47], which will not be repeated here. The three time constants mentioned above can be determined experimentally by the following measurements. "Relaxation with discharge on" measurement refers to monitoring the decreasing optical signal from the optical polarimeter with the discharge on and the laser beam blocked. The measured optical signal under this condition can be fitted with a double exponential formula [47] with two time constants: a long time constant which is a measurement of the relaxation of the coupled double-cell system with discharge-on and a short time constant which is closely related to the transfer time between the two cells. The long and short amplitudes from the fit contain information about the initial pumping cell polarization and the target cell polarization. Fig. 3.13 shows a discharge-on relaxation measurement taken during the experiment with 24 μA beam on the target.

"Transfer measurement" is another type of relaxation measurement with the discharge on. It involves monitoring the recovery of the pumping cell polarization through diffusion of atoms from the target cell after the laser beam is blocked and the pumping cell polarization is destroyed by pulsing an rf magnetic field for ~ 0.1 sec at the Larmor frequency. The optical signal from this measurement again can be fitted by a double exponential formula as described in the previous paragraph. Fig. 3.14 shows a typical transfer run taken during the experiment with 25μA beam on the target.

The last type of relaxation measurement is called "discharge-off relaxation mea-

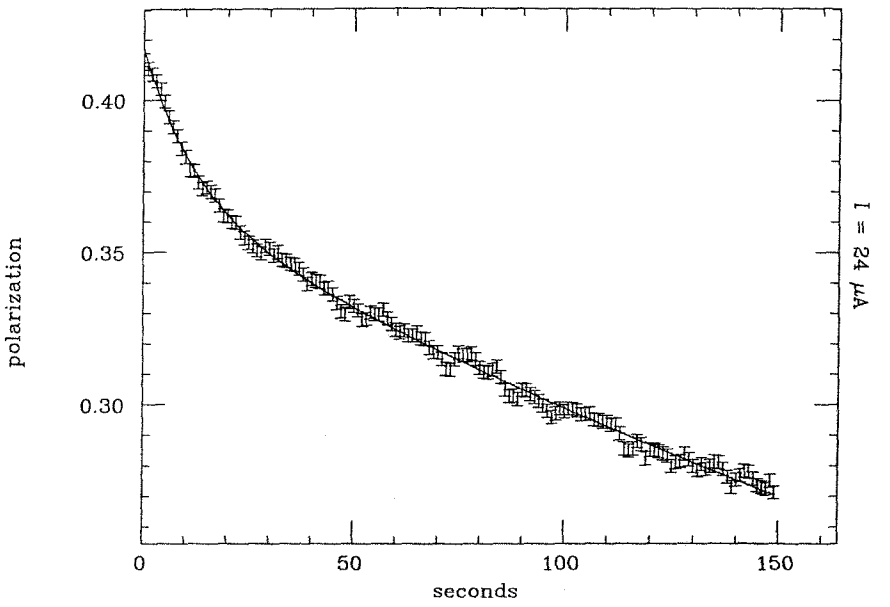

Figure 3.13: Discharge-on relaxation measurement taken during the experiment.

surement" and is essentially a measurement of the copper target cell relaxation time under the condition that the relaxation time of the pumping cell with discharge off is known. The relaxation measurement with the discharge off is performed by measuring the pumping cell polarization with the discharge off and the laser beam blocked. For the optical polarimeter, the presence of a discharge is necessary for exciting the 668-nm light. The discharge is turned on for 2 seconds to perform the measurement every 30 seconds. Data are only averaged for the last 0.7 second of the 2 seconds when the discharge is on because the discharge requires some time to stabilize. The relaxation effect from the discharge itself has to be corrected for this type of measurement before extracting the relaxation time constant. The ith sample polarization is corrected as follows:

$$p_{corr} = p_{meas} e^{i\Delta t/t_d}, \tag{3.16}$$

where Δt is the amount of time that the discharge is on and t_d is the relaxation time constant that is due to the discharge. The long time constant obtained from either

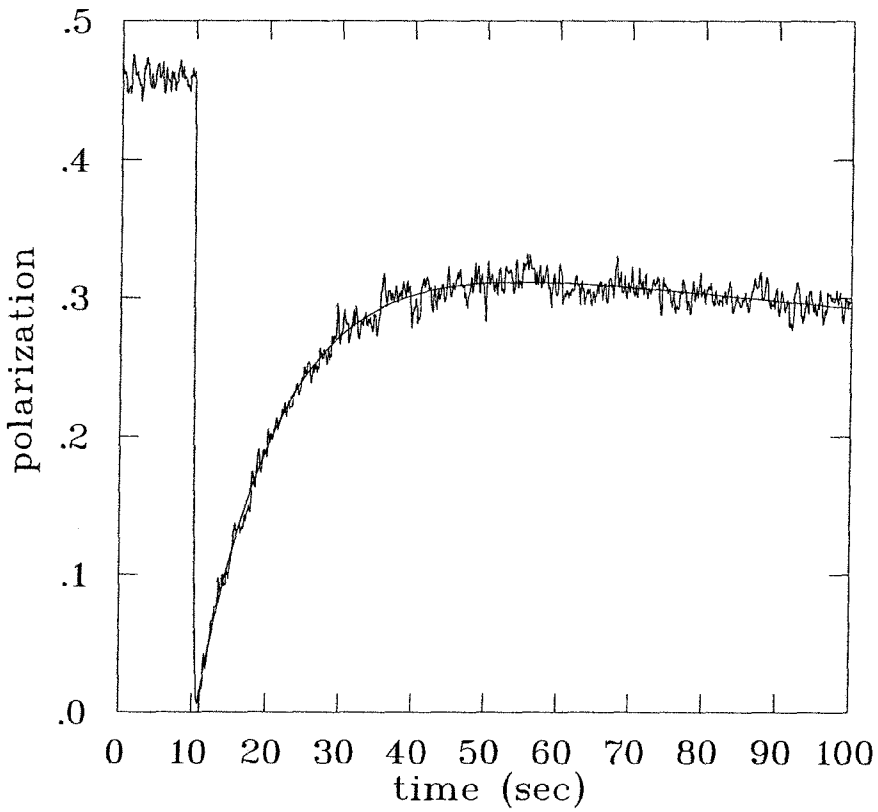

Figure 3.14: Transfer run taken during the experiment with 25μA beam.

the transfer run or the discharge-on relaxation run has been used as an approximated value for t_d in correcting the data from the discharge-off relaxation measurement as t_d was not actually measured. The optical signal from the discharge-off relaxation measurement follows a single exponential formula except for the first data point, because mixing between the two cells occurs. The first data point is not included in the fit. The uncertainty in the fit obtained by using the approximated t_d in correcting the data points described above has been studied using the procedure from [47] (see Section 4.4.2 in [47]). The uncertainty in extracting the target polarization from this effect has been found to be less than 1%.

The information of the pumping cell relaxation time constant with the discharge off can be approximated by the single-cell relaxation time constant. It can be obtained from polarization measurements on a single sealed glass cell of the same size as that of the pumping cell and in the position of the pumping cell. The measurements were taken with the same holding field as that of the real target system and with the spectrometers on. This measurement serves as a check of the background magnetic field gradient as well.

Experimentally, by combining either the transfer run with the discharge-off relaxation run or the discharge-on relaxation measurement with the discharge-off relaxation measurement, one can determined the pumping cell relaxation time, the target cell relaxation time, and the transfer time between the two cells. These three time constants together with the volume ratio of the pumping cell to the target cell can be used to extract the target polarization from the pumping cell polarization measured by the optical polarimeter during the experiment.

The single-cell relaxation time τ_{sc} for the present work was measured to be 715 ± 28 sec with a holding field of 36 gauss and both spectrometers on. The target cell relaxation time τ_t is given by [47]:

$$\frac{1}{\tau_t} = \frac{N}{N_t}\left(\frac{1}{\tau_{l(off)}} - \frac{N_p}{N}\frac{1}{\tau_{sc}}\right), \tag{3.17}$$

where N_p, and N_t are the number of ^{3}He atoms in the pumping cell, and target cell, respectively. $N = N_p + N_t$ and $\tau_{l(off)}$ is the single time constant obtained from discharge-off relaxation run. N_p/N_t is obtained by measuring the volume ratio of the pumping cell to the target cell as is described in [47].

The pumping cell relaxation time τ_p can then be determined using the long time constant τ_l of a double exponential fit obtained either from a transfer run or a discharge-on relaxation run [47].

$$\frac{1}{\tau_p} = \frac{N}{N_p}(\frac{1}{\tau_l} - \frac{N_t}{N}\frac{1}{\tau_t}). \tag{3.18}$$

Lastly the transfer time of the coupled system is obtained [47]:

$$\frac{1}{t_{ex}} = \frac{1}{\tau_s} + \frac{1}{\tau_l} - \frac{1}{\tau_p} - \frac{1}{\tau_t}, \tag{3.19}$$

where τ_s is the short time constant which can be obtained either from a transfer run or from a discharge-on relaxation run.

With the knowledge of the time constants of the double-cell system, the initial pumping cell and target cell polarization are obtained using a double exponential fit from a discharge-on relaxation run [47].

$$P_p(0) = a_l + a_s, \tag{3.20}$$

$$P_t(0) = \left[1 + \tau_s(\frac{1}{\tau_p} - \frac{1}{\tau_t})\right] a_l - \left[\frac{N_p}{N_t}\right] a_s, \tag{3.21}$$

where a_s and a_l are the short and long amplitudes of the double exponential fit, respectively.

If a transfer run measurement is taken, then the target cell polarization is obtained from this type of measurement in the following way [47]:

$$0 = a_l + a_s \tag{3.22}$$

$$P_t(0) = \left[(\frac{N}{N_t}) + \tau_s (\frac{1}{\tau_p} - \frac{1}{\tau_t}) \right] a_l \tag{3.23}$$

The equilibrium pumping cell polarization before it is zeroed is obtained from the optical measurement. From these equations the ratio of the equilibrium target cell polarization to the pumping cell polarization is obtained, which is used to extract the target cell polarization because only the pumping cell polarization was monitored during the experiment. The ratio of the target cell polarization to the pumping cell polarization can also be expressed in terms of the transfer time and the target cell relaxation time [47], which can be used to cross check this ratio obtained as described above.

$$\frac{P_t}{P_p} = \frac{1}{1 + \frac{N}{N_p} \frac{t_{ex}}{\tau_t}}. \tag{3.24}$$

3.5.3 Target Data Acquisition and Control System

A dedicated VAXstation II connected to a Camac crate monitored the target and performed control functions through a target data acquisition program. This program was first developed at Caltech and later modified at MIT into a version which can be used both for the MIT internal target [53] and the Caltech external target. The modified version was used for the present work. The computer monitored the voltage signals for the polarization measurement (see Section 3.4.1), read the target temperatures from the temperature controller, monitored the laser power output, controlled the shutter to the laser, turned the discharge in the ^{3}He gas on and off, performed relaxation measurements, and changed the high voltage on the Pockels cell to flip the target spin direction. The polarization and target temperature information was passed to the main data acquisition (LAMPF Q data acquisition) system for the experiment through output and input registers. Because the polarization was stable, the target polarization was sampled every second and passed to the main data acquisition system every second. The polarization information from the main data stream was used in the data analysis, as it was checked to be consistent

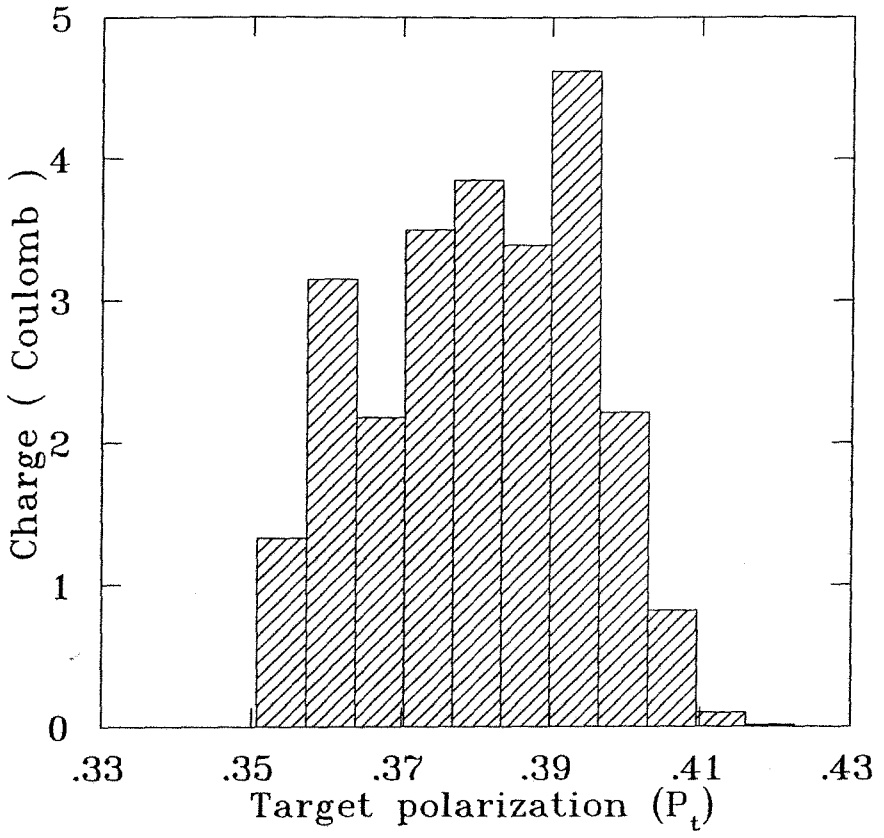

Figure 3.15: Histogram of the target polarization vs. the beam charge.

with the information from the target computer. Because of the radiation problem of the temperature controller during the experiment, the temperature readout by the target computer was disabled and a camera was set up in the experimental hall to remotely monitor the temperatures in the counting bay. Detailed information on the electronics for the target computer control and polarization measurement system is given elsewhere [47].

3.5.4 Target Polarization Analysis

The target polarization was very stable during the experiment. The target spin was flipped a few times a day to minimize systematic uncertainties. It took about 15 minutes to flip the target spin from one orientation to another. The target polarization was found to be a few percent higher for the right helicity of the incident

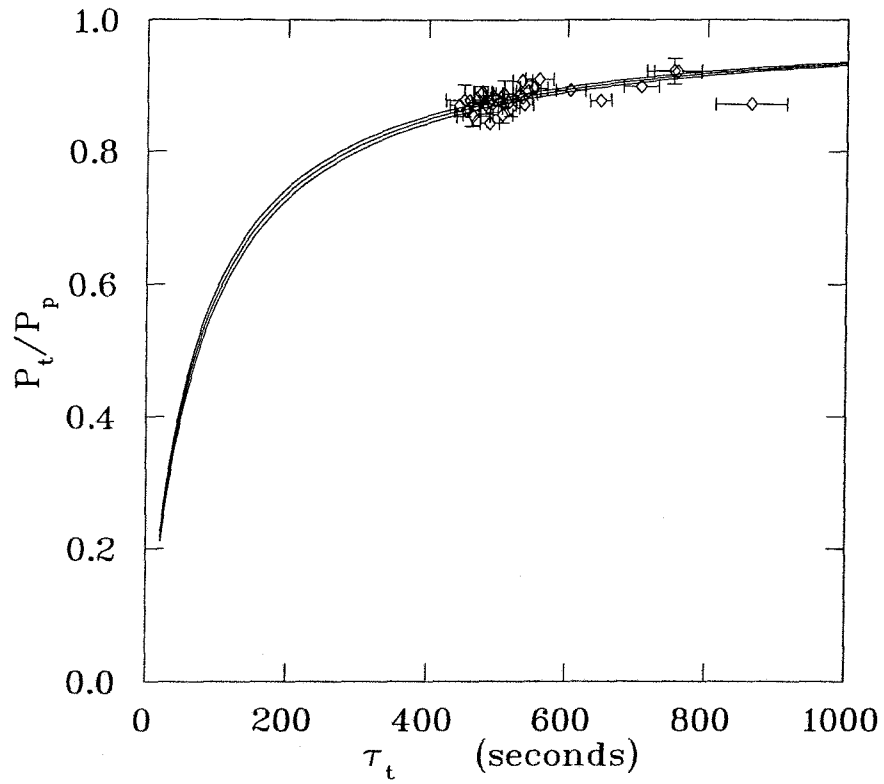

Figure 3.16: Measured P_t/P_p vs. the target cell relaxation time.

laser light than that of the left helicity, which was not quite understood as the degree of circular polarization of each light helicity was adjusted to be better than 99.7%. The average target polarization was over 38% with 25μA of incident electron beam. Fig. 3.15 is a histogram of the average target polarization for the experiment versus the beam charge in Coulombs.

The target was cooled to 12 K before the experiment and the target temperature rose about 1 K or so with 25 μA beam incident. The average target temperature during the experiment was 12.8 K and the average helium gas pressure was 2.15 torr. Nitrogen coating was applied to the inner surface of the copper cell to reduce the low temperature surface effects. No obvious deterioration of the nitrogen coating was found during the experiment and the target was only re-coated twice during one month of data taking plus one month of waiting for beam. The electron beam current was around 20 - 30 μA with an average beam current of about 25 μA. The target

cell relaxation time was measured once a day during the experiment by either the transfer run with discharge-off relaxation run, or the discharge-on relaxation run with the discharge-off relaxation run, and the target cell relaxation time was found to be fairly stable. The ratio of the target cell polarization to the pumping cell polarization, P_t/P_p, was determined from these relaxation measurements. Fig. 3.16 shows all the measured values of P_t/P_p during the experiment with beam on the target and a fit of P_t/P_p versus the measured target cell relaxation time. The transfer time obtained from this fit is 11.6 ± 0.5 sec which is consistent with the transfer time determined from the relaxation measurements. Table 3.2 lists the results of relaxation runs taken during the experiment with beam on the target, and an average $P_t/P_p = 0.89$ was used for calculating the target polarization from the measured pumping cell polarization for the asymmetry analysis.

A few corrections have been applied to the target polarization. A correction factor of 1.02 with an uncertainty of 0.5% for a holding field of 36 gauss has been applied to the optical signal because of the decoupling of the electronic spin from the nuclear spin due to the magnetic field. This correction is based on the measurements taken on a sealed cell as was discussed earlier in the section on NMR calibration [63]. The optical polarimeter was positioned 14° off-axis with respect to the holding field, and a correction factor of 1.05 with an uncertainty of less than 1% to the optical signal, was determined after the experiment (see Section 3.4.1). Lastly, a correction for the pressure factor has been applied on a run-to-run basis due to temperature variation from run to run.

The optical signal was very stable during the experiment and the statistical uncertainty of the optical measurement was negligible as compared with the systematic uncertainties. The optical measurement has been calibrated by an NMR measurement with an accuracy of ±2%. The uncertainty of the pressure factor due to the uncertainty of the target temperature (0.5 K) has been determined to be ±1%. The uncertainty of the ratio P_t/P_p because of the uncertainties of the target cell relaxation time, the transfer time, and the target temperature, has been estimated to be

$\pm 1.5\%$. An overall uncertainty of $\pm 3\%$ has been applied to the target polarization.

I (μA)	P_t/P_p	τ_t (sec)	type
16.0	0.871 ± 0.009	863 ± 48	R
20.0	0.921 ± 0.008	757 ± 32	R
20.0	0.898 ± 0.007	705 ± 23	R
20.0	0.877 ± 0.008	648 ± 14	R
12.0	0.922 ± 0.020	753 ± 36	T
26.0	0.866 ± 0.013	518 ± 10	T
26.0	0.887 ± 0.007	510 ± 12	R
24.0	0.874 ± 0.006	514 ± 10	R
24.0	0.868 ± 0.006	538 ± 12	R
26.0	0.887 ± 0.020	509 ± 15	T
28.0	0.856 ± 0.018	462 ± 12	T
27.0	0.842 ± 0.008	487 ± 24	R
25.0	0.861 ± 0.009	453 ± 16	R
22.0	0.892 ± 0.008	543 ± 17	R
27.0	0.889 ± 0.009	478 ± 12	R
24.0	0.887 ± 0.009	531 ± 23	R
24.0	0.875 ± 0.010	487 ± 24	R
24.0	0.853 ± 0.015	464 ± 22	T
20.0	0.896 ± 0.009	551 ± 19	R
26.0	0.907 ± 0.007	535 ± 13	R
26.0	0.881 ± 0.009	535 ± 13	R
20.0	0.910 ± 0.009	559 ± 20	R
25.0	0.883 ± 0.008	493 ± 14	R
25.0	0.871 ± 0.013	491 ± 19	R
23.0	0.887 ± 0.012	475 ± 9	R
20.0	0.870 ± 0.008	443 ± 13	R
24.0	0.877 ± 0.008	458 ± 8	R
23.0	0.877 ± 0.025	452 ± 25	R
20.0	0.855 ± 0.013	506 ± 14	R
20.0	0.870 ± 0.014	482 ± 17	R
12.0	0.893 ± 0.009	604 ± 21	R
13.0	0.931 ± 0.008	893 ± 26	T
17.0	0.921 ± 0.007	790 ± 22	T
23.0	0.902 ± 0.009	732 ± 26	T

Table 3.2: Results of relaxation runs taken during the experiment with beam on target; T denotes transfer run and R stands for discharge-on relaxation run.

Chapter 4

Data Analysis

In this chapter, we will discuss mainly the analysis of the MEPS data, which involves the extraction of the MEPS spin-averaged quasielastic yield and the spin-dependent quasielastic transverse asymmetry $A_{T'}$. The OHIPS elastic asymmetry was measured as a check of the experimental procedure. The analysis for the OHIPS elastic cross section and the elastic asymmetry will be discussed in this chapter. Data for the quasielastic transverse-longitudinal asymmetry $A_{TL'}$ in OHIPS elastic-threshold region, a region sensitive to different schemes for extracting spin-dependent structure functions, as well as to final state interactions and meson exchange currents, have also been analyzed in this work and will be described in this chapter.

4.1 The Experimental Cuts

The experimental cuts defining the OHIPS and MEPS "good" electron and pion events are discussed in this section. The hardware trigger for OHIPS events discussed in Section 2.5 required a hit in each of the three scintillators (3S), or a hit in any two out of the three scintillators together with a hit in the Čerenkov counter (2S·Č). The events triggered by the requirement that each of the three scintillators fired (3S), are filtered in software and used in the data analysis. The hardware trigger

does not necessarily eliminate background events from the ^{3}He target wall, the beam pipe, etc. Further experimental cuts are required to restrict the spectrometer events to be those originated from the ^{3}He target. The experimental cuts discussed here are the software cuts pertaining mainly to the information from the drift chamber. Information on extraction of the track position and the slope from the delay line signals is given in detail in [35]. For each plane of the VDCX, there are four delay lines with 28 or 29 wires on each line. The wire number is determined from the time difference of signals from each end of the delay line. The sum of the signals from each end of the delay line gives the drift time which can then be used to calculate the drift distance. The test defining an event to have "good" momentum information required a signal from all four of the delay lines and that the signals from the four delay lines be in order. There was a slope test applied to the VDCX which required that the slope of the track, calculated from the drift distance, must be positive for each plane of the VDCX. This eliminated multiple-hit events or events with noise on the delay line which interfered with the wire number determination, resulting in poor track reconstruction. Additional tests were the two-dimensional cut on the reconstructed target θ versus ϕ acceptance to restrict the electrons to originating from the ^{3}He target, and the cut on the target y acceptance to match the spectrometer target length acceptance. A software cut on the Čerenkov ADC signal was applied for rejecting the pions. The pion rejection efficiency was better than 95%. Lastly, there was a test on the scintillator timing signal which required good timing peaks for all three of the scintillators. The efficiency of this cut was better than 99.9%. The "good" electron events defined by the tests described above were named ODELGS in the Q histograms. ODELGS was used to extract the OHIPS elastic and quasielastic yield with corrections applied to account for the good events that failed the slope test (see Section 4.3.1). The experimental cuts defined for ODELGS as described above together with an additional test for the electron beam helicity were used for extracting the helicity-dependent asymmetry without further momentum cuts.

The hardware trigger for MEPS events required also a hit in all three of the

trigger hodoscopes, or a hit in any two out of the three trigger hodoscopes together with a hit in the Čerenkov counter. Again, the events triggered by the requirement that all three trigger hodoscopes fired (3S) are filtered in software and used in the data analysis. The software cuts pertained to the information of the VDCX were very similar to those of OHIPS: the test on the reconstructed target θ versus ϕ acceptance, and the test on the target y acceptance.

The momentum cut defining "good" events were different from those of the OHIPS VDCX, as the MEPS VDCX readout was different (see Section 2.4.2). For each event, the minimum and maximum wire fired were determined from the raw data. The VDCX area bound by the minimum and maximum wire fired was considered the active area for that event. Looping over this area, all wires were grouped together into clusters allowing one hole per cluster. A cluster was called a cluster with pivot if an internal wire had the minimum absolute drift distance. For the cluster with a pivot, the tracks to the left of the pivot and right of the pivot were fitted. The difference between the projected tracks at the pivot point measured how well the left and right sides fit together. For an event which had multiple clusters, a cluster was chosen as the selected cluster for the chamber if the difference between the projected tracks at the pivot point was smallest. The "good" electron events were those events which had good selected cluster with pivot in each chamber. Fig. 4.1 shows a charged particle track and drift distances in the vertical drift chamber (VDC). The cluster grouped by these four fired wires indicated in Fig. 4.1 is a selected cluster with pivot. Again detailed information on the MEPS VDCX readout electronics and software can be found in [36].

A software cut on the Čerenkov ADC signal was also used to separate the pions from the electrons, and the efficiency for the pion rejection was better than 97%. There was an additional test applied to all three of the scintillator ADC signals requiring the ADC signals to be above the background level. The MEPS "good" electron events, defined by the above experimental cuts, were named FPDELS in the Q histograms, were used for extracting the quasielastic cross-section with cor-

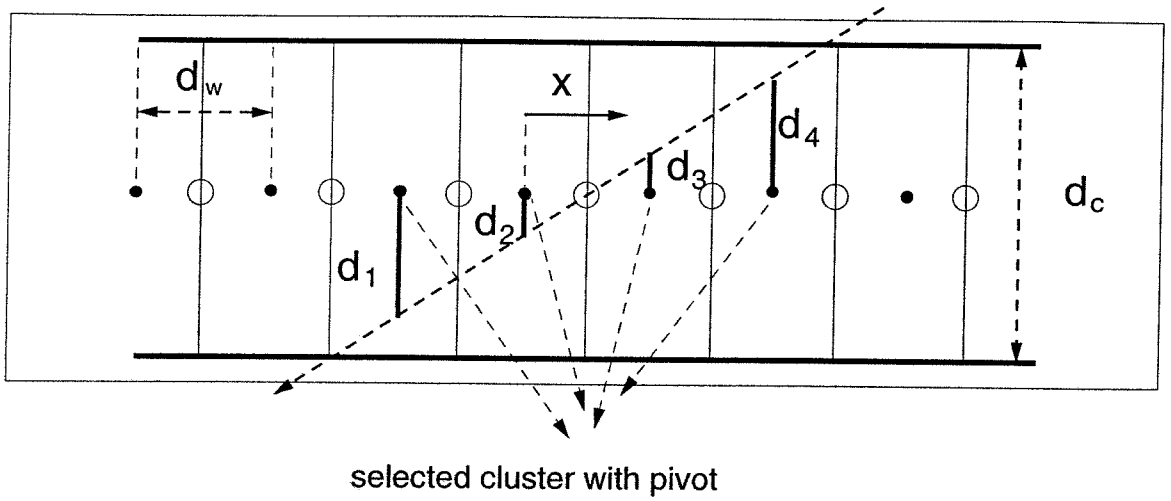

Figure 4.1: Charged particle and drift distances in the vertical drift chamber (VDC) with wire distance d_w and thickness d_c.

rection applied to account for the good events which had bad reconstructable momenta because of multiple clusters. The experimental cuts used to define FPDELS together with an additional test on the electron beam helicity were used for extracting the spin-dependent asymmetry without further momentum cuts. For both spectrometers, the "good" pion events were defined by all the experimental cuts for the electrons except the Čerenkov ADC cut.

4.2 Background

The spectrometer background came from the empty target events and the elastic radiative tail. The pion background was negligible, as pions were separated from the electrons using the Čerenkov counters. The measurements of the empty target background and the calculation of the elastic radiative tail are described in this section.

4.2.1 Empty Target Yield

As the target employed in this work was a low pressure gas target ($\sim 1.6 \times 10^{19}\text{cm}^{-2}$ for OHIPS, and $\sim 3.3 \times 10^{18}\text{cm}^{-2}$ for MEPS), significant background came from the target wall and the target window. Tungsten collimators were installed outside of the scattering chamber along the target direction to prevent the spectrometers from seeing events originated from the target window. The dominant contribution to the empty target yield were events originated from the target wall and it was discovered previously that the empty target background was sensitive to the beam position on the ^{3}He target [47]. Prior to the data taking of this experiment, the empty target yield versus the beam positions were studied carefully (run 150 - 165). The optimum beam position, -1 mm to the left of the target center and -5 mm below the center of the target was found, corresponding to the minimum empty target yield in both spectrometers. This was the nominal beam position for the data taking of ^{3}He spin-dependent asymmetry measurement. It was found that the empty target background was not sensitive to the beam position as the beam moved around the x or y direction within $\pm$ 1 mm from its nominal position. The beam position was checked between the runs to make sure that it was at the nominal position or close to it using the fluorescence of a beryllium oxide (BeO) target upstream of the ^{3}He target. Empty target runs were taken from time to time during the experiment and the on-line $\frac{\pi}{e}$ ratio (the ratio of the raw on-line pion events over the electron events) served as a good monitor of the empty target yield. It was discovered around ^{3}He runs 285 to 291, after an activation of the GaAs crystal for the polarized source, that the on-line $\frac{\pi}{e}$ ratio was very high. The target was pumped out immediately and an empty target run (run 292) was taken. The empty target yield was very high for this run as was expected from the high on-line $\frac{\pi}{e}$ ratio. A better beam tune was requested which improved the situation significantly. The empty target yield versus the beam position was studied again between runs 302 - 312 and the same nominal beam position was found as before. The data from runs 285 - 291 were

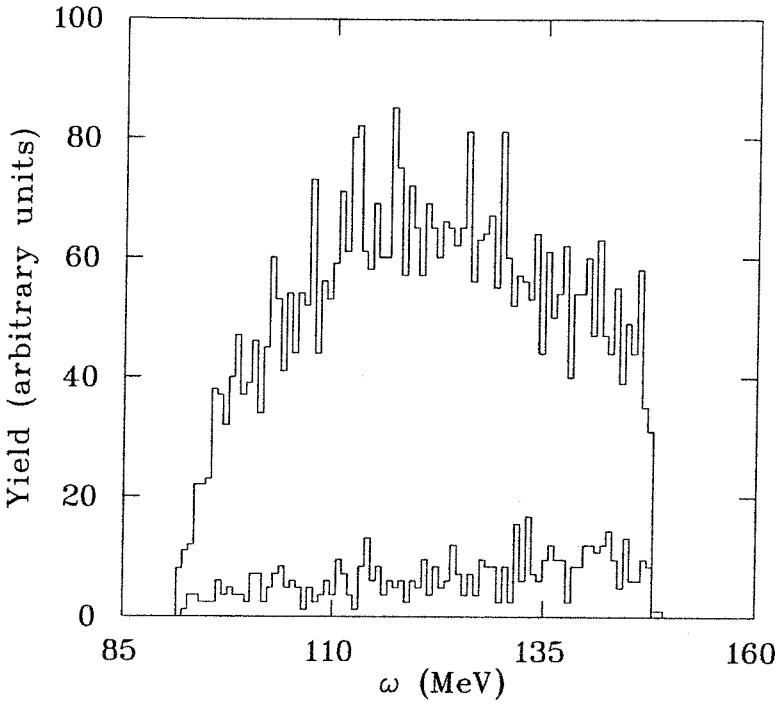

Figure 4.2: MEPS empty vs. full target yield as a function of energy loss, ω.

not used in the analysis due to the high background yield. Variations in the empty target background larger than the statistical fluctuations were observed from the empty target runs taken. The average of all the empty target runs with beam at the nominal position or close to it (except for runs 292, 157, and 304 - 307) was used for the background subtraction.

MEPS spectrometer had two quasielastic spectrometer settings during the ^{3}He data taking. It was set to a central momentum of 255 MeV/c at the beginning of the experiment (runs before 178) with a total accumulated beam charge of 2.67 Coulomb. The empty target yield was $12.4 \pm 1.1\%$ of the full target yield for this setting in the electron energy loss range of $86 \leq \omega \leq 144$ MeV. The MEPS spectrometer central setting was changed to 250 MeV/c from run 179 and the total accumulated charge for this setting was 21.37 Coulomb. The empty target yield was $11.7 \pm 1.1\%$ of the full target yield for this setting in the ω range of $91 \leq \omega \leq 148$ MeV. Fig. 4.2 shows the typical empty target versus full target yields in the MEPS spectrometer.

The OHIPS spectrometer was used to measure the ^{3}He quasielastic transverse-longitudinal asymmetry, $A_{TL'}$, as well as the elastic asymmetry and $A_{TL'}$ in the elastic-threshold region. Fig. 4.3 shows the typical OHIPS quasielastic empty versus full target yield as a function of ω and the empty vs. full target yield in the elastic-threshold region. The OHIPS quasielastic empty target yield was $4.9 \pm 0.3\%$ of the full target yield in the ω region of $72 \leq \omega \leq 95$ MeV.

4.2.2 Elastic Radiative Tail

In the lowest order of QED (one-photon exchange diagram) the elastic peak appears as a delta function in the momentum space, smeared by the beam energy spread and the spectrometer resolution. However, because of the straggling effect in the target and bremsstrahlung, there are events for which the elastically scattered electrons have lower final momentum than the elastic peak; these events comprise the elastic radiative tail. The experimentally measured inelastic spectrum is superimposed on the elastic radiative tail. Subtraction of the elastic radiative tail is crucial especially in the elastic-threshold region where the tail height is of a size comparable to the quasielastic yield. An accurate calculation of the elastic radiative tail is also important for extracting the quasielastic asymmetry from the experimentally measured asymmetry because the ^{3}He asymmetry in the elastic radiative tail is much bigger than the ^{3}He quasielastic asymmetry.

The elastic radiative tail was calculated following the procedure of Mo and Tsai [79] in which the formula of multiple-photon emission was used. The average target thickness corresponding to the average target temperature and pressure was used in the calculation. The target entrance window was a 5.8 μm copper foil and the exit material consisted of the 0.25 mm copper target wall, corrected for the scattering angle, and approximately 0.41 mm of aluminum in the exit window of the scattering chamber, and the first-stage thermal radiation shield. The effect from the additional material of the spectrometer windows was negligible. The elastic radiative tail is

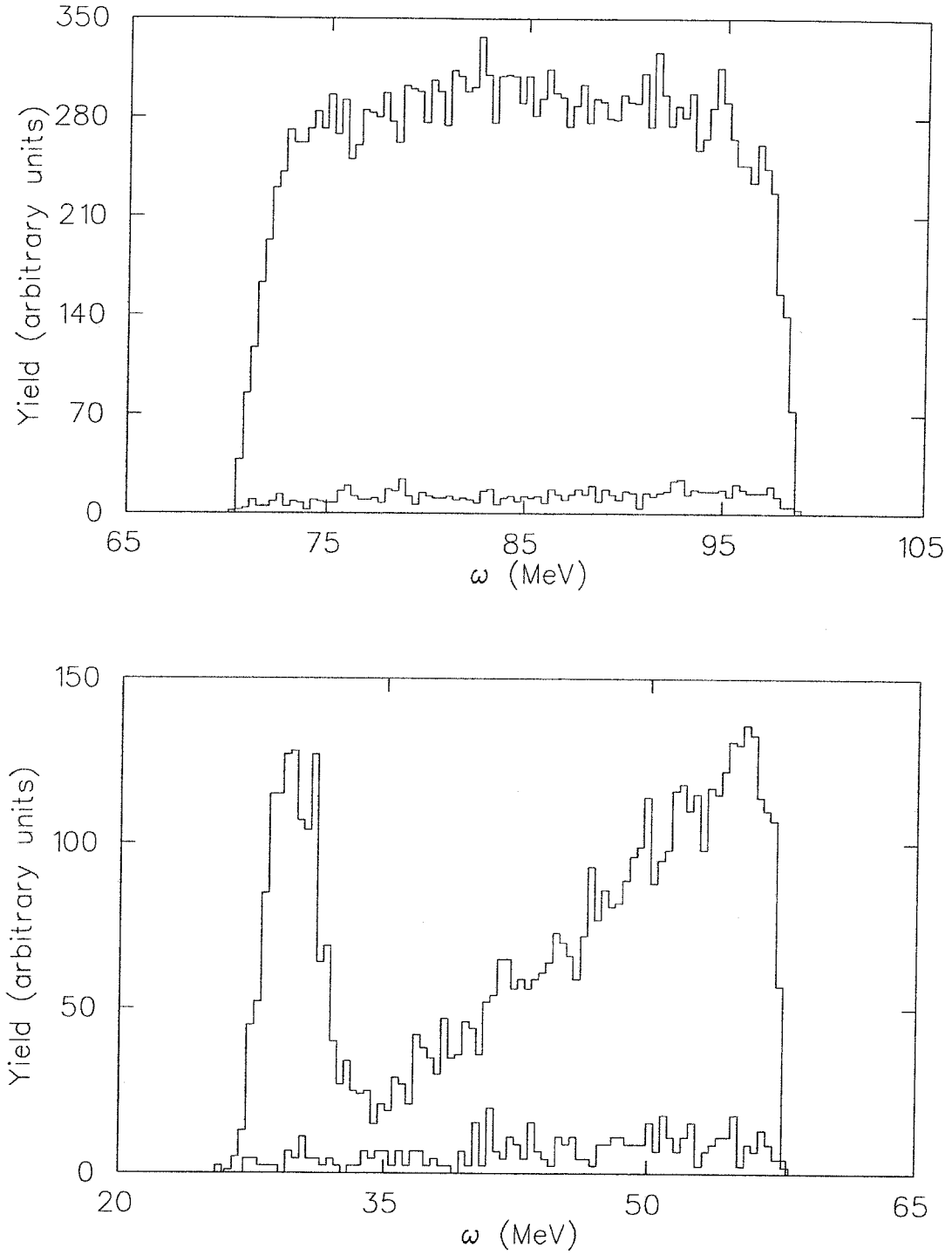

Figure 4.3: OHIPS empty vs. full target yield as a function of the electron energy loss, ω. The top plot shows the quasielastic empty vs. full target yield and the bottom plot is the empty vs. full target yield in the elastic-threshold region.

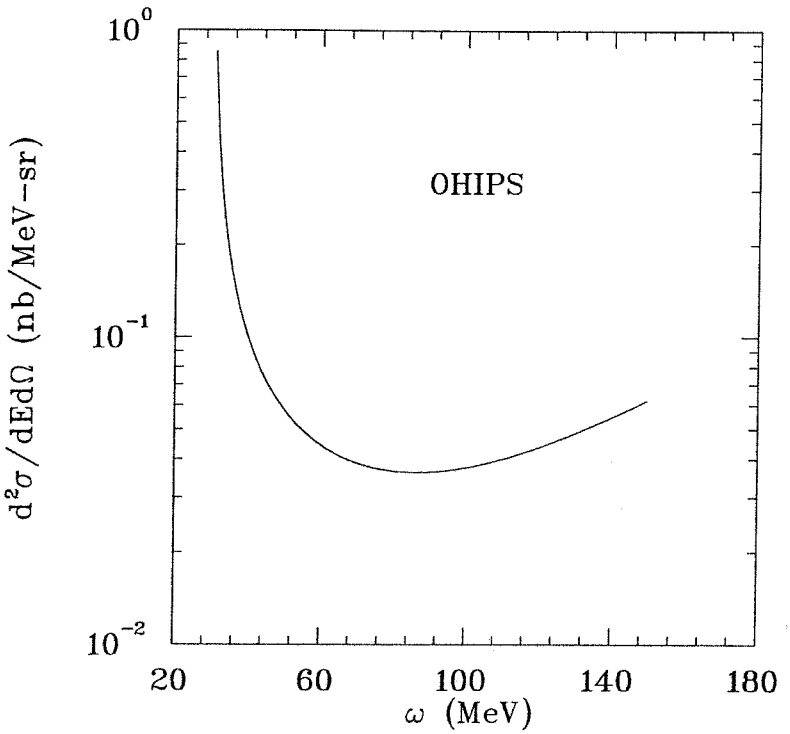

Figure 4.4: Calculated OHIPS elastic radiative tail.

dominated by the "internal" radiation for the ^{3}He target system, where "internal" radiation refers to radiation in the field of the primary target nuclei involved in the scattering process, and "external" refers to radiation from interactions from other target nuclei or with nuclei in the entrance and exit material of the target system. Fig. 4.4 is the calculated elastic radiative tail for the OHIPS quasielastic kinematics corresponding to a beam energy of 370 MeV and a scattering angle of 70.1° to the right of the electron beam. The elastic radiative tail was estimated to contribute 0.8% to the total yield in OHIPS spectrometer. Fig. 4.5 is the calculated elastic radiative tail for the MEPS quasielastic kinematics for a scattering angle of 91.4° to the left of the electron beam. The elastic radiative tail was estimated to contribute 0.4% to the total yield in the MEPS spectrometer.

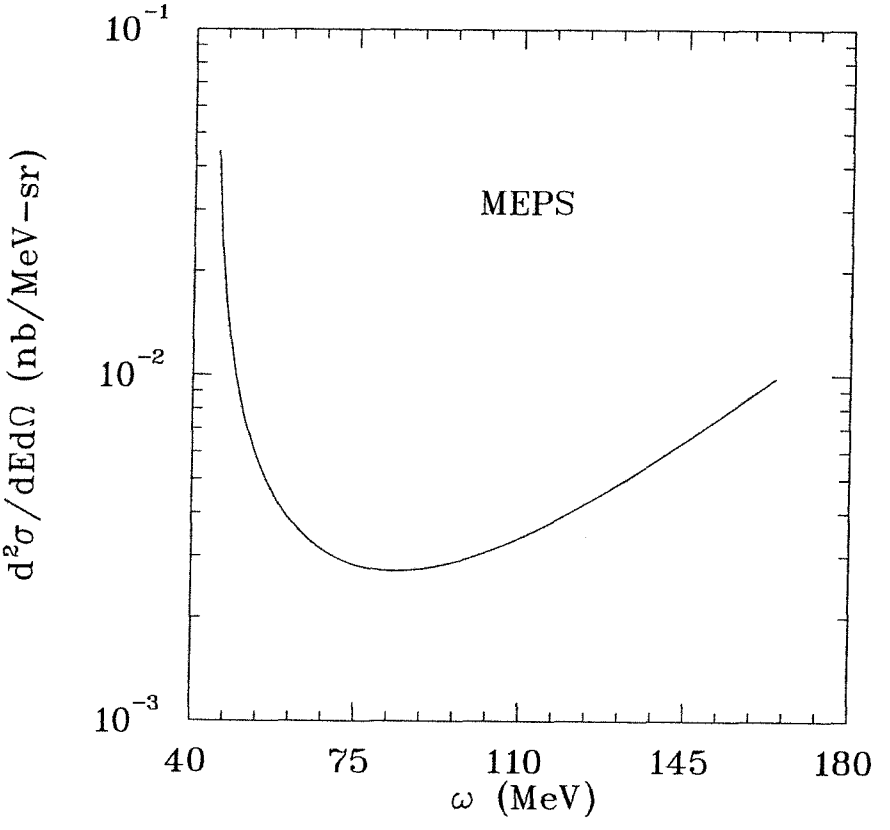

Figure 4.5: Calculated MEPS elastic radiative tail.

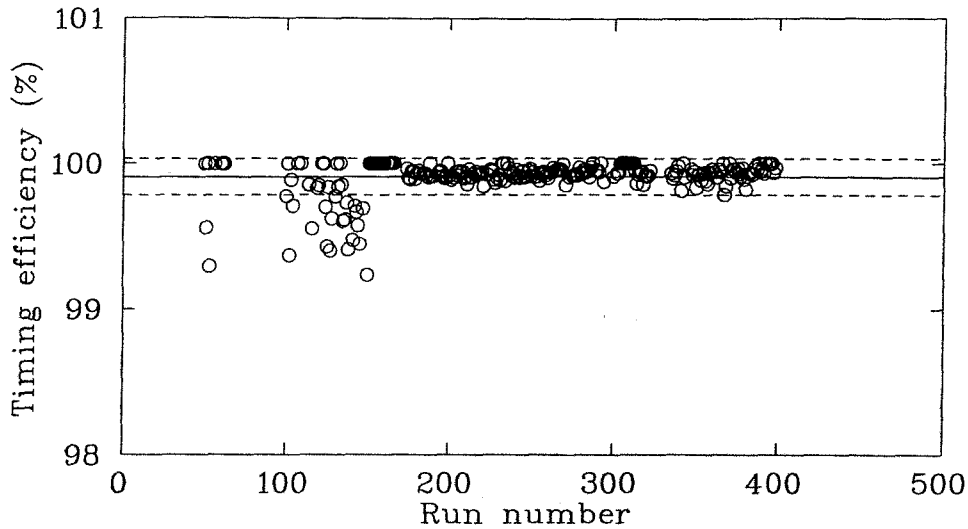

Figure 4.6: OHIPS scintillator timing efficiency vs. run numbers.

4.3 Experimental Cross Section

4.3.1 OHIPS Elastic Cross Section

Both the elastic asymmetry and cross section were extracted from the OHIPS data. The experimental elastic cross section was calculated from the experimental observables as follows:

$$\frac{d\sigma}{d\Omega} = \frac{N_{ODELGS}(\Delta E)}{N_e N_t \Delta\Omega \epsilon e^{-\delta(\Delta E)}}, \tag{4.1}$$

where

$N_{ODELGS}(\Delta E)$ = number of counts in the elastic peak up to inelasticity ΔE,

N_e = number of the incident electrons,

N_t = target thickness in nuclei per unit area,

$\Delta\Omega$ = solid angle,

ϵ = delay line efficiency $\times$ computer live time $\times$ tracking efficiency,

$e^{-\delta(\Delta E)}$ = radiative correction for inelasticity ΔE.

Inelasticity of 1% from the elastic peak has been chosen in this analysis. Eq. 4.1 gives the spin-averaged elastic cross section, as histogram ODELGS included events of both electron helicities. The OHIPS scintillator timing efficiency is not included

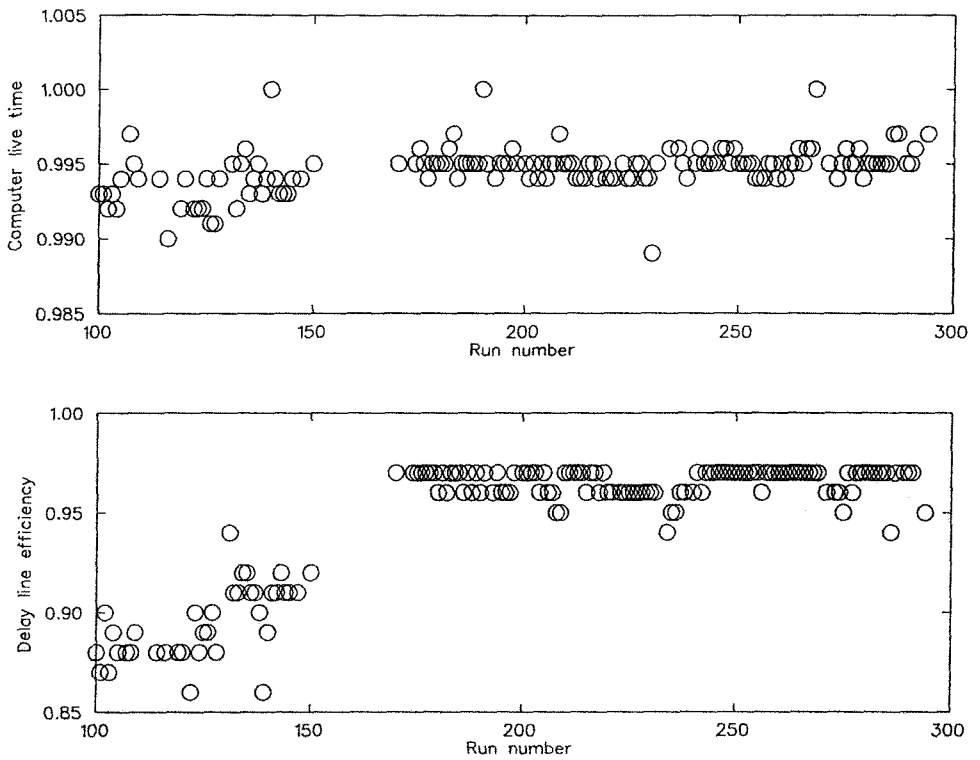

Figure 4.7: OHIPS computer live time, delay line efficiency vs. run numbers.

in the above expression for calculating the overall efficiency ϵ as the average timing efficiency is better than 99.9% for all the runs. Fig. 4.6 shows the OHIPS timing efficiency for all the runs (target full and target empty). The beam charge was measured for each beam pulse with three beam toroids (BT1, BT2, BT3) and recorded for each pulse. The charge information from BT2, closer to the ^{3}He target, was used in calculating the spin-averaged cross section and the ^{3}He asymmetry. The target nuclei thickness, N_t, is calculated by

$$N_t = 9.7 \times 10^{18} \, (\frac{pL}{T}), \tag{4.2}$$

where N_t is in units of nuclei/cm^2, p is the target pressure in torr, L is the effective target length in centimeters, and T is the target temperature in kelvins. The target thickness was calculated for each run using the average target temperature for the run and the target temperature and pressure when it was filled. The average target

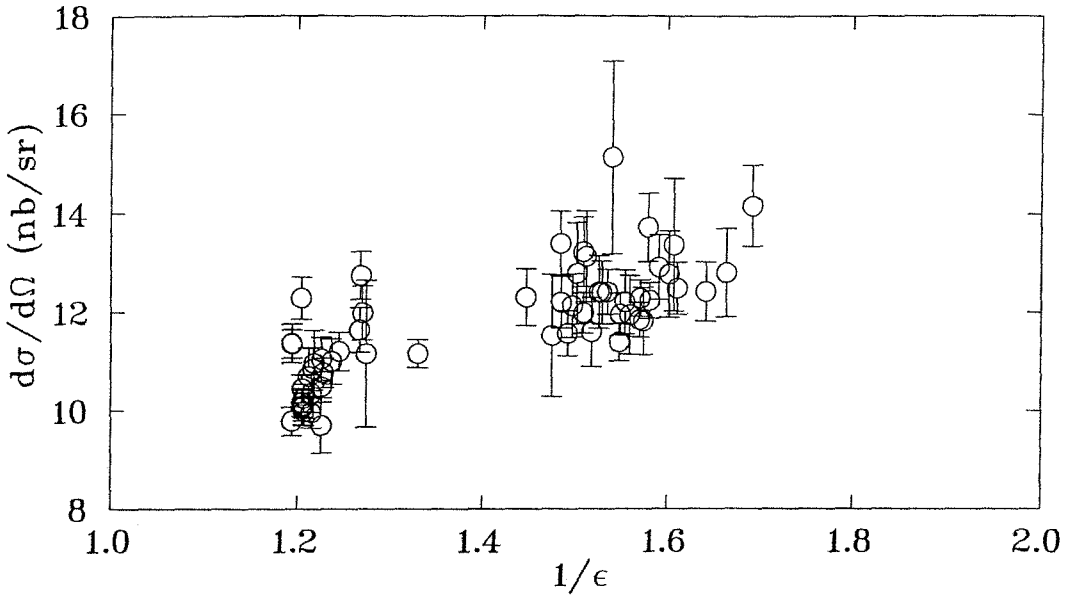

Figure 4.8: The OHIPS experimental elastic cross section vs. the inverse of the overall efficiency for all the elastic runs; the overall efficiency is the product of the delay line efficiency, the computer live time, and the tracking efficiency. The tracking efficiency is calculated using Eq. 4.4.

temperature for the experiment was 12.8 K, the average pressure was 2.15 torr, and the extended target length acceptance was 10 cm for OHIPS, corresponding to an average target thickness of 1.6×10^{19} cm^{-2}. The OHIPS solid angle used in calculating the experimental cross section was 12.2 msr. This solid angle value was based on a Monte Carlo simulation of the OHIPS acceptance using the TURTLE program [80] with respect to an extended target length of 10 cm. The OHIPS delay line efficiency of the VDCX is given by the product of the individual delay line efficiency (4 delay lines for each plane, 8 in total). For the purpose of determining a single line efficiency, an event is judged "good" if it registered a hit on all the other delay lines; i.e., the efficiency of the i^{th} delay line is given by

$$\epsilon_i = \frac{\mathcal{N}\,(\text{hits on all 8 delay lines })}{\mathcal{N}\,(\text{hits on all delay lines j } \neq \text{ i })}. \tag{4.3}$$

Fig. 4.7 shows the OHIPS delay line efficiency and the computer live time for all the asymmetry runs taken with the target full.

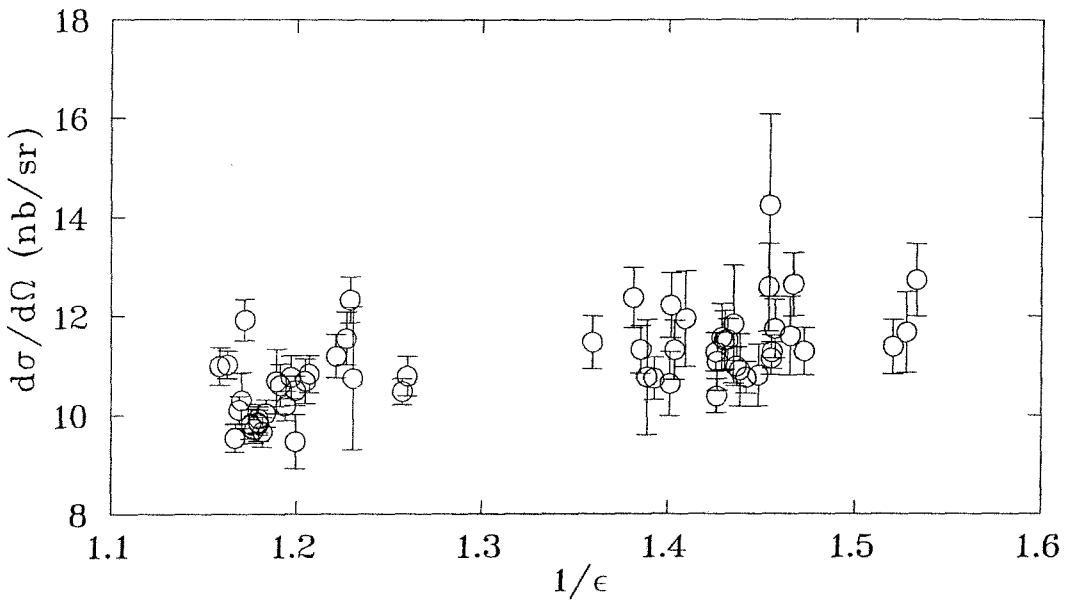

Figure 4.9: The OHIPS experimental elastic cross section vs. the inverse of the overall efficiency for all the elastic runs; the overall efficiency is the product of the delay line efficiency, the computer live time, and the tracking efficiency. The tracking efficiency is calculated using Eq. 4.5.

The correction to the cross section due to the tracking efficiency is essentially a correction to account for the good events which failed the slope test described in Section 4.1 because of badly reconstructed tracks caused by multiple hit events. This correction was applied to the experimental cross section because data collected during the optical study of the previous ^{3}He experiment [47] on the ^{12}C elastic scattering cross section indicated that the events eliminated by the more stringent test on ODELGS were good events but without reliably reconstructable momenta.

The definition of the tracking efficiency used previously [47] was

$$\epsilon_{\text{tracking}}^{-1} = \frac{\mathcal{N}\,(\text{events with hits on four wires})}{\mathcal{N}\,(\text{events with hits on four ordered wires and pass slope test})} \tag{4.4}$$

This definition of the tracking efficiency was initially used in calculating the experimental elastic cross section. A correlation between the overall efficiency, ϵ, and the experimental elastic cross section has been found. The OHIPS elastic data were taken with three different spectrometer central momentum settings during the ex-

periment to measure the elastic asymmetry as well as to cover the elastic-threshold region. Fig. 4.8 shows the calculated experimental elastic cross section for all three of the spectrometer settings versus the inverse of the overall efficiency with the tracking efficiency defined by Eq. 4.4, and a correlation between the cross section and the overall efficiency is indicated clearly. The empty target yield was 5.8% of the full target yield for the cut chosen for the elastic peak. Empty target background was subtracted from the elastic peak before calculating the experimental cross section, so was the small contribution from the quasielastic yield. The elastic radiative correction factor has been calculated to be 1.44 for the inelasticity chosen for this analysis using the formula of Mo and Tsai [79] for the ^{3}He target system.

A new definition for calculating the tracking efficiency

$$\epsilon^{-1}_{\text{tracking}} = \frac{\mathcal{N}\,(\text{events with hits on four ordered wires})}{\mathcal{N}\,(\text{events with hits on four ordered wires and pass the slope test})} \tag{4.5}$$

was used then in calculating the experimental cross section which improved the correlation between the overall efficiency and the experimental cross section to some extent, as shown in Fig. 4.9. It is believed that the original definition double counted events which failed the slope test.

The differential cross section for ^{3}He elastic scattering is calculated by the following formula

$$\frac{d\sigma}{d\Omega} = \sigma_M(1 + \frac{2E}{M}\sin^2\frac{\theta}{2})^{-1}\left\{\frac{Z^2F_c^2}{1+\tau} + \tau\mu_A^2F_m^2\left(\frac{1}{1+\tau} + 2\tan^2\frac{\theta}{2}\right)\right\}, \tag{4.6}$$

where F_c and F_m are the ^{3}He charge and magnetic form factors respectively. Using Eq. 4.6 together with the ^{3}He charge and magnetic form factors measured by Rosenbluth separation [81], the calculated ^{3}He elastic cross section is 12.4 nb/sr for an incident electron beam energy of 370 MeV and an electron scattering angle of 70.1°. The average experimental cross section for all the ^{3}He elastic runs using the tracking efficiency definition of Eq. 4.5 was 10.64 $\pm$ 0.84 nb/sr with the statistical

uncertainty being the standard deviation of the yield. This experimental yield was 16.5% lower than the expected 12.4 nb/sr.

4.3.2 OHIPS Quasielastic Cross Section

The raw experimental differential quasielastic cross section is calculated from the OHIPS experimental observables by

$$\frac{d^2\sigma}{dEd\Omega} = \frac{N_{ODELGS}}{N_e N_t \Delta E \Delta\Omega \epsilon} \tag{4.7}$$

where

N_{ODELGS} = counts in ODELGS within the chosen energy bin,

N_e = number of the incident electrons,

N_t = target thickness in nuclei per unit area,

ΔE = energy bin size in MeV,

$\Delta\Omega$ = solid angle for the chosen energy bin size,

ϵ = computer live time $\times$ delay line efficiency $\times$ tracking efficiency.

The tracking efficiency has been calculated using Eq. 4.5. A constant solid angle of 12.2 msr has been used in this analysis as the OHIPS acceptance is fairly flat across the focal plane. In order to get the ^{3}He quasielastic cross section, the empty target background, and the elastic radiative tail have been subtracted from the raw experimental yield. To get the unradiated physics cross section, the ^{3}He quasielastic radiative correction has been applied to the measured cross section based on the calculation using the formula of Mo and Tsai [79]. Fig. 4.10 shows the calculated quasielastic cross section using a y-scaling calculation [82] which describes the quasielastic cross section as the product of a kinematics factor, a single-nucleon cross section, and a universal scaling variable y, at the OHIPS kinematics with and without radiative corrections.

The quasielastic cross section near the top of the quasielastic peak (75 MeV $\leq \omega \leq$ 95 MeV) and the tail part of the peak, i.e., low ω region (37 MeV $\leq \omega \leq$

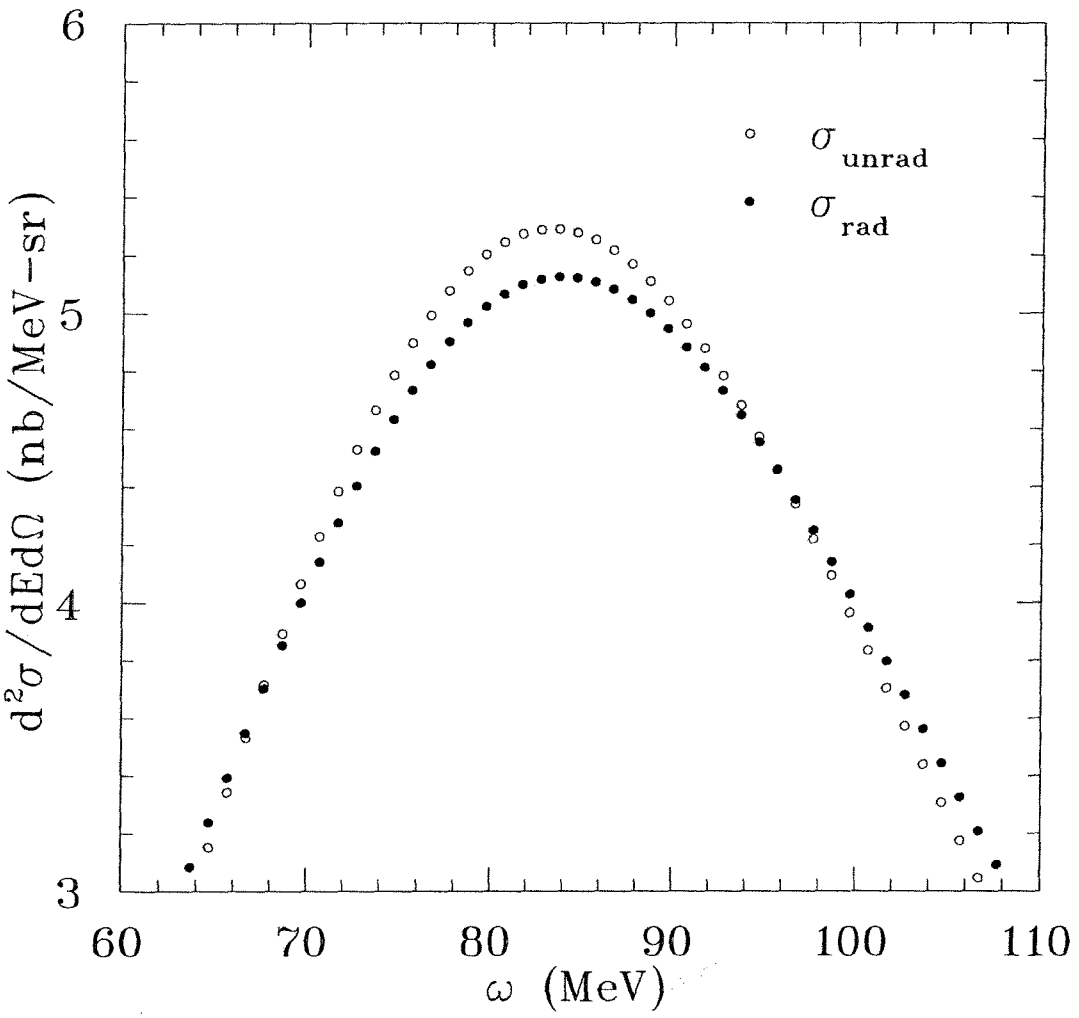

Figure 4.10: Calculated OHIPS quasielastic cross section with and without radiative corrections.

53 MeV) has been extracted from the data as the OHIPS spectrometer had the quasielastic central setting as well as settings for the elastic-threshold region (low ω region). No quasielastic radiative correction has been applied to the experimental cross section in the low ω region as the reliability of the calculation of the quasielastic radiative effects is limited by the experimental data in this region. The energy bin size of 3.3 MeV was chosen for the part of the data in the elastic-threshold region and 2.87 MeV was used for the data near the top of the peak. The normalization factor of 1.165 with respect to the experimental elastic cross section has been applied to the measured quasielastic cross section. Fig. 4.11 shows the extracted quasielastic cross section with the statistical uncertainties only together with a y-scaling calculation [82] at the OHIPS kinematics, and the previous Bates data [83] scaled to the OHIPS kinematics. The data are in good agreement with both the y-scaling calculation and the scaled data near the peak region, while the agreement is rather poor in the low ω region. analysis is 10%, dominated by the uncertainties in the solid angle and the target length acceptance.

4.3.3 MEPS Quasielastic Cross Section

The MEPS raw experimental quasielastic cross section is calculated as follows:

$$\frac{d^2\sigma}{dEd\Omega} = \frac{N_{FPDELS}}{N_e N_t \Delta E \Delta\Omega(E)\ \epsilon}, \tag{4.8}$$

where

N_{FPDELS} = counts in FPDELS within the chosen energy bin,

N_e = number of the incident electrons,

N_t = target thickness in nuclei per unit area,

ΔE = energy bin size in MeV,

$\Delta\Omega(E)$ = solid angle for the chosen energy bin size.

ϵ = computer live time $\times$ VDCX tracking efficiency.

The MEPS VDCX efficiency is not included in Eq. 4.8 in calculating the overall

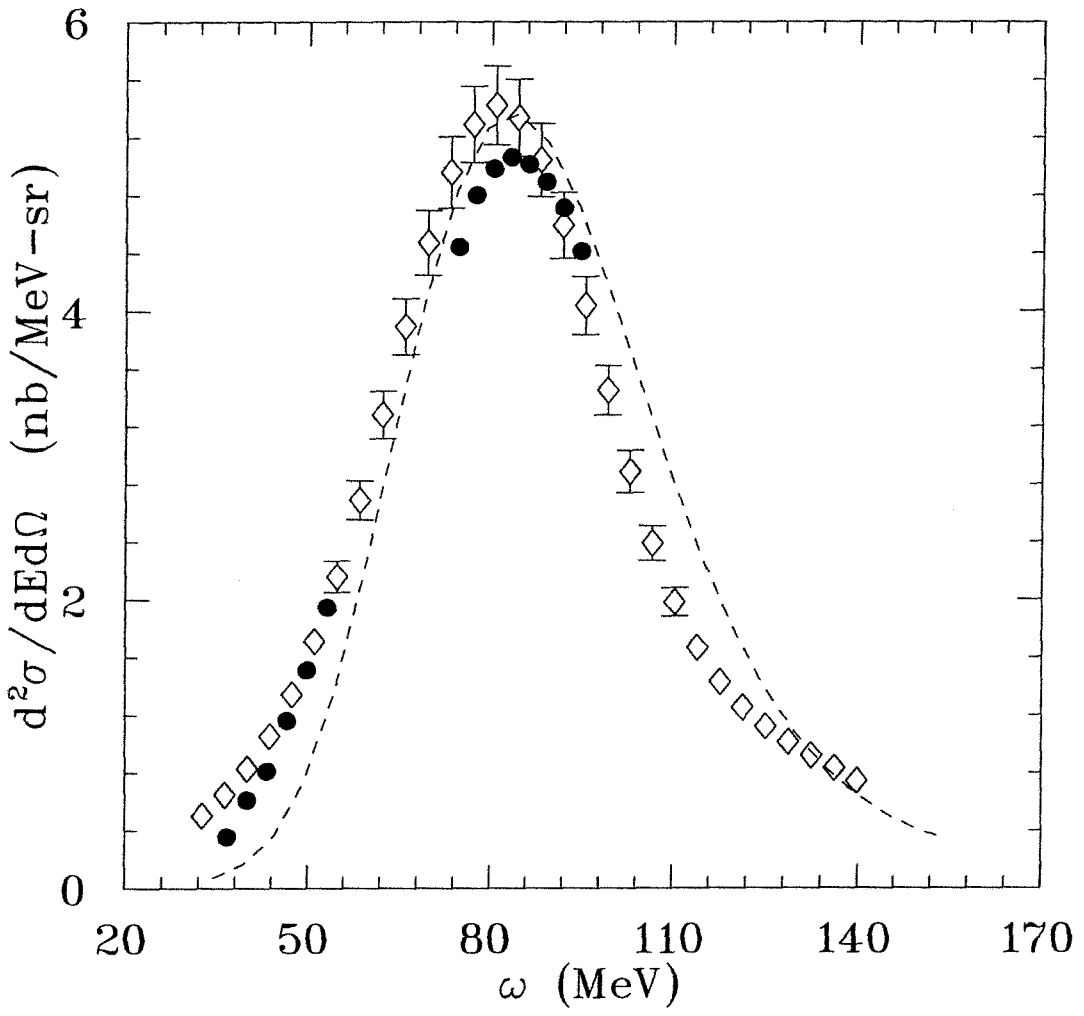

Figure 4.11: The extracted OHIPS quasielastic cross section with statistical uncertainties only (solid circles) vs. a y-scaling calculation [82] (dashed line), and the previous Bates data [83] (open diamonds) scaled to the OHIPS kinematics.

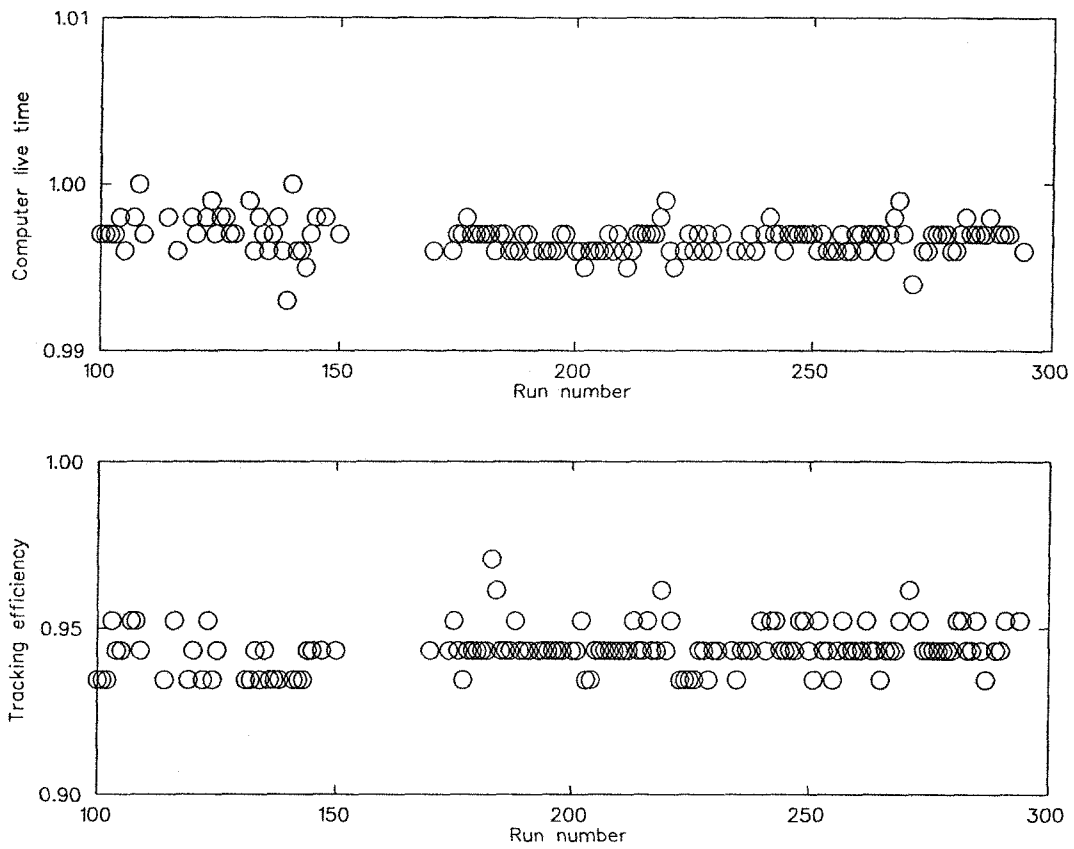

Figure 4.12: MEPS computer live time, tracking efficiency vs. ^{3}He asymmetry runs.

efficiency as it is close to 1 (better than 99.5%). The VDCX tracking efficiency is calculated by

$$\epsilon_{tracking}{}^{-1} = \frac{\mathcal{N}(\text{selected cluster in each chamber})}{\mathcal{N}(\text{selected cluster with pivot in each chamber})}, \tag{4.9}$$

where the numerator stands for the number of events which have a selected cluster in each chamber, and the denominator denotes the number of events which have a selected cluster with a pivot in each chamber. Fig. 4.12 shows the MEPS computer live time and the VDCX tracking efficiency for all the ^{3}He asymmetry runs with the target full. The MEPS acceptance across the focal plane is not flat, and the acceptance function

$$\Delta\Omega\ (p) = 14.125 - 0.367 * \delta - 2.92e - 03 * \delta^2 \ \ (\text{msr}), \tag{4.10}$$

has been obtained from the optics study done in the spring of 1993 prior to the ^{3}He data taking. δ is in percentage defined as

$$\delta = \frac{p - p_0}{p_0}, \tag{4.11}$$

where p_0 is the central momentum setting of the spectrometer, and p is the momentum of the scattered electron. This δ-dependent ($\delta = \frac{\Delta(P-P_0)}{P_0}$) solid angle has been used in extracting the MEPS quasielastic cross section. The MEPS spectrometer had an extended target acceptance of 2 cm which corresponded to an average target density of 3.3×10^{18} /cm^2. The energy bin size chosen for this analysis was 2.8 MeV. The empty target background and the elastic radiative tail were subtracted from the experimental raw cross section. The quasielastic radiative correction given by the formula of Mo and Tsai [79] has then been applied to yield the "unradiated" quasielastic cross section. Fig. 4.13 shows the calculated quasielastic cross section using a y-scaling calculation [82] at the MEPS kinematics with and without radiative corrections.

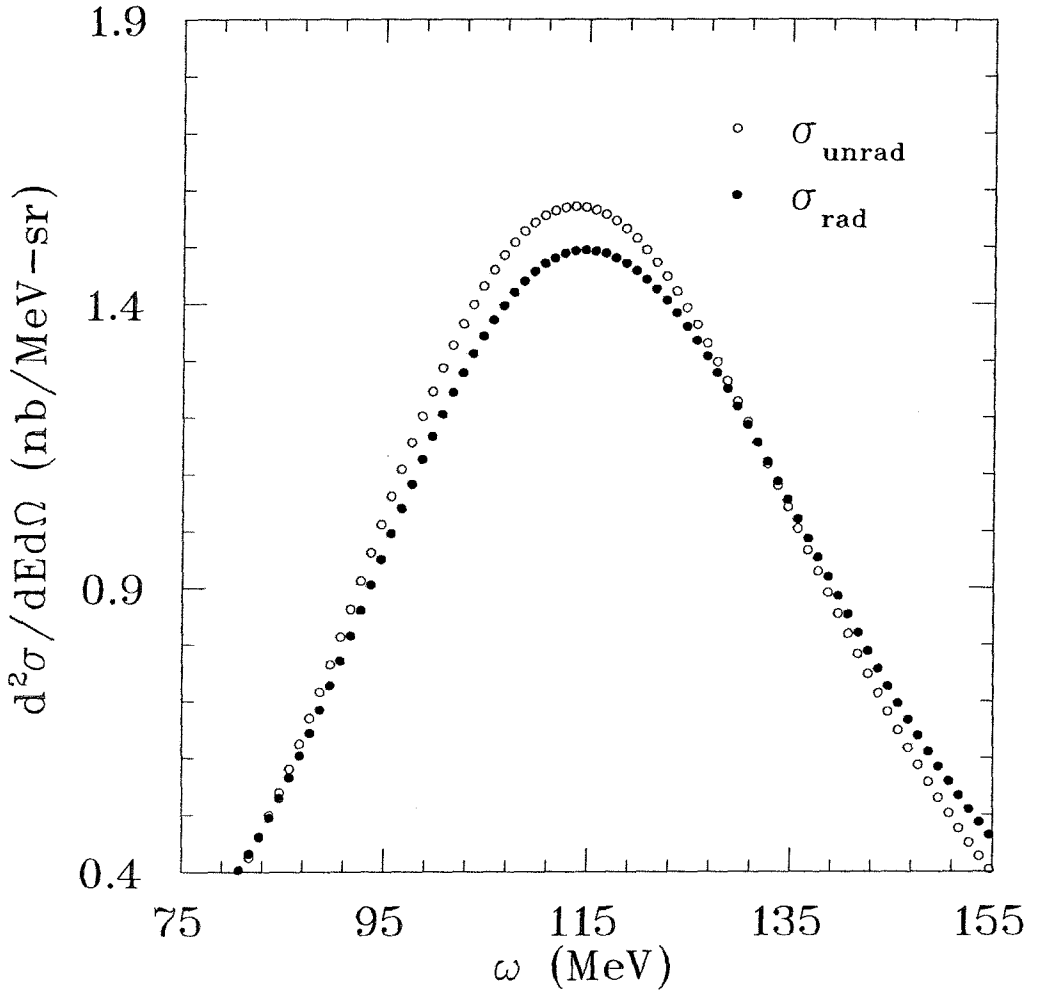

Figure 4.13: Calculated MEPS quasielastic cross section with and without radiative corrections.

There were two quasielastic spectrometer central settings for MEPS data taking. It was set to a central momentum of 255 MeV/c in the beginning of the experiment (before run 178) with a total accumulated beam charge of 2.67 Coulomb. The spectrometer central setting was changed to 250 MeV/c from run 179 and the total accumulated charge for this setting was 21.37 Coulomb. The combined extracted quasielastic cross section (weighted by the total accumulated beam charge for each setting) with statistical uncertainties only in the ω range of 95.7 MeV $\leq \omega \leq$ 140.8 MeV is shown in Fig. 4.14 together with a y-scaling calculation [82] at the MEPS kinematics, and the previous Bates data [83] scaled to the MEPS kinematics. The data are in good agreement with both the y-scaling calculation and the scaled data. The systematic uncertainty on the extracted cross section in this analysis is 10%, dominated by the uncertainties in the solid angle and the target length acceptance.

4.4 Experimental Asymmetry

4.4.1 OHIPS Elastic Asymmetry

The OHIPS raw experimental elastic asymmetry is calculated by

$$A_{exp} = \frac{N_+ - N_-}{N_+ + N_-} \tag{4.12}$$

where N_+, and N_- are the normalized (w.r.t. the beam charge) good electron events (defined by the experimental cuts described in Section 4.1) within the elastic peak for positive and negative electron helicities respectively.

The experimentally measured elastic asymmetry is diluted by the product of the target polarization and the beam polarization, as well as the empty target background. The extracted elastic asymmetry is corrected from the raw experimental asymmetry by

$$A_{el} = f\frac{A_{exp}}{P_t P_b}, \tag{4.13}$$

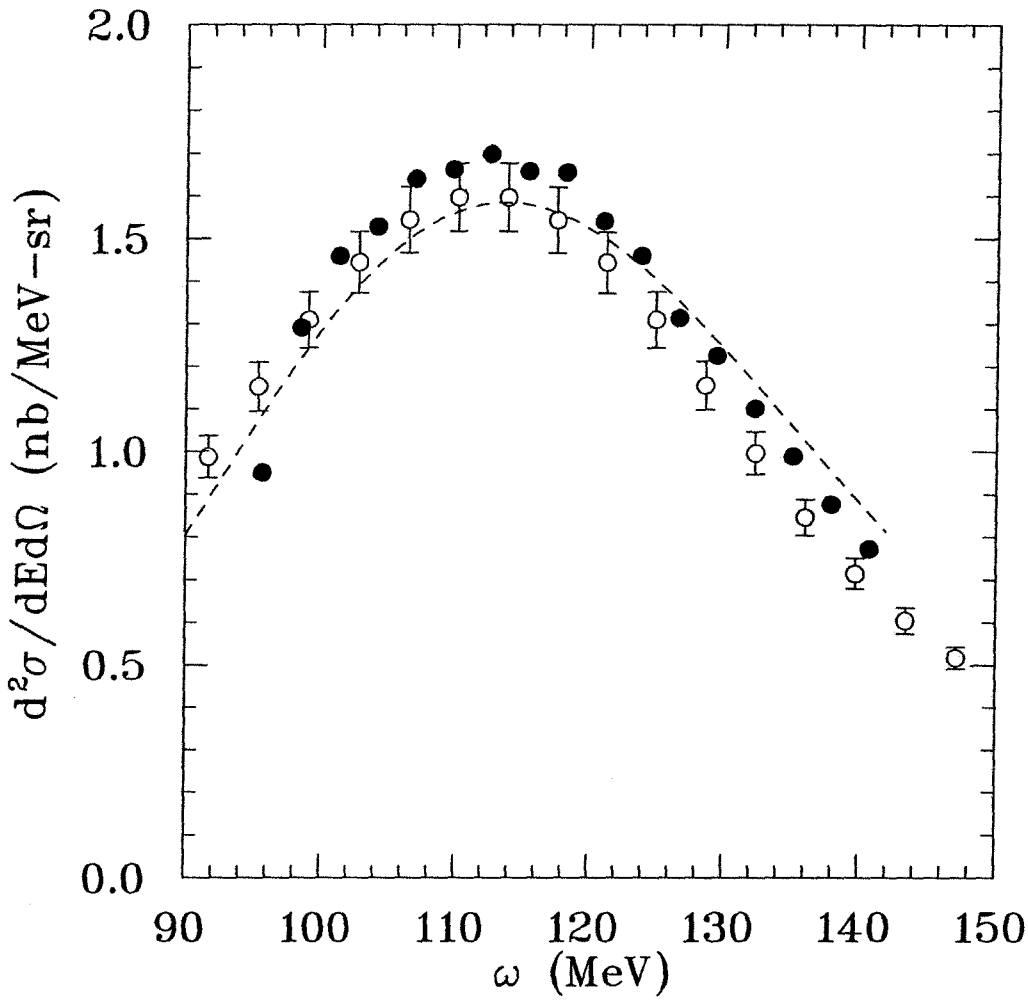

Figure 4.14: The extracted MEPS quasielastic cross section with statistical uncertainties only (solid circles) vs. the y-scaling calculation [82] (dashed line), and the previous Bates data [83] (open circles) scaled to the MEPS kinematics.

where P_t, and P_b are the target and beam polarizations, respectively. f is the dilution factor due to the empty target background given by

$$f = \frac{1}{1 - \frac{\sigma_{\text{empty}}}{\sigma_{\text{total}}}}, \tag{4.14}$$

with σ_{empty}, and σ_{total} being the empty target yield and the total yield, respectively.

4.4.2 OHIPS $A_{TL'}$ in Elastic-Threshold Region

The quasielastic asymmetry in the elastic-threshold region at the kinematics with the target spin direction close to normal with respect to the 3-momentum transfer vector $\mathbf{q}$ ($\theta^* = 93°, 87°$ for positive and negative target spin, respectively), i.e., $A_{TL'}$ kinematics, has been measured in the OHIPS spectrometer. The raw experimental asymmetry in this region (so-called low ω region) is calculated from the data as follows:

$$A_{exp} = \frac{N_+ - N_-}{N_+ + N_-}, \tag{4.15}$$

where N_+, and N_- are the normalized (w.r.t. the beam charge) good electron events within the chosen ω bin for the positive and negative electron helicities, respectively.

To get the physics asymmetry from the raw experimental asymmetry, corrections need to be made with respect to the target and the beam polarizations, the empty target background, and the elastic radiative tail. The extracted physics asymmetry, $A_{TL'}$, is given by

$$A_{TL'} = \frac{1}{P_t P_b} A_{exp} \left(\frac{1}{1 - d_{empty} - d_{eltail}} \right) - A_{eltail} \left(\frac{d_{eltail}}{1 - d_{empty} - d_{eltail}} \right), \tag{4.16}$$

where

$$d_{background} = \frac{\sigma_{background}}{\sigma_{total}}. \tag{4.17}$$

The correction to the asymmetry due to the quasielastic radiative effects is not included in the above expression. Although the correction to the asymmetry due to

the quasielastic radiative effects has been calculated to be small, this is the region where the reliability of the calculation of the quasielastic radiative effects is limited by the experimental data.

The ω bin size of 3.27 MeV was chosen for the analysis in the low omega region. This had the advantage of having relatively more data points in this region to see how $A_{TL'}$ varies around the 2-body and 3-body breakup thresholds and the disadvantage of possibly having larger statistical error bars. The calculation of the elastic radiative tail is described in Section 4.2.2 and will not be repeated. We will only discuss the calculation of the asymmetry in the elastic radiative tail here.

In addition to the cross section dilution factor, the experimental asymmetry must be corrected for the asymmetry of the events in the elastic radiative tail as shown in Eq. 4.16. The elastic asymmetry can be expressed in terms of the ^{3}He charge and magnetic form factors, F_c and F_m, as

$$A_{el} = \frac{\Delta}{\Sigma} = -\frac{2\tau\mu_A^2 v_{T'} \cos\theta^* F_m^2 + 2\sqrt{2\tau(1+\tau)}\mu_A Z v_{TL'} \sin\theta^* \cos\phi^* F_m F_c}{(1+\tau)Z^2 v_L F_c^2 + 2\tau\mu_A^2 v_T F_m^2} \tag{4.18}$$

where the form factors have been normalized to

$$F_c(Q^2 = 0) = F_m(Q^2 = 0) = 1. \tag{4.19}$$

In this formula Z is the nuclear charge, μ_A is defined in terms of the magnetic moment of ^{3}He as $(m_{\mathrm{He}}/m_n)\mu_{\mathrm{He}}$, and all other variables are defined in Chapter 1.

In general, if there is an asymmetry in the elastic peak, then there will also be an asymmetry in the radiative tail, although the value will be different from the peak value because of the spread in energies of the incident and scattered particles contributing to the tail. To calculate the asymmetry in the elastic radiative tail, first the elastic radiative tail cross section is calculated separately for the left and right helicity electrons using the full expression, including both spin-dependent and spin-independent terms for the elastic cross section in the calculation. Then the

asymmetry is calculated in the normal manner:

$$A_{eltail} = \frac{\left(\frac{d^2\sigma}{d\Omega dE}\right)_{eltail_+} - \left(\frac{d^2\sigma}{d\Omega dE}\right)_{eltail_-}}{\left(\frac{d^2\sigma}{d\Omega dE}\right)_{eltail_+} + \left(\frac{d^2\sigma}{d\Omega dE}\right)_{eltail_-}}. \tag{4.20}$$

Fig. 4.15 shows the calculated asymmetry in the elastic radiative tail as a function of ω at the OHIPS kinematics. The elastic radiative tail contributes significantly to the experimental asymmetry in the low omega region as the size of the elastic radiative tail is comparable to that of the quasielastic cross section in this region. There is also a large systematic uncertainty in the extracted physics asymmetry in this region due to the uncertainty in the experimental quasielastic yield.

4.4.3 MEPS Quasielastic Asymmetry $A_{T'}$

The ^{3}He quasielastic asymmetry at the kinematics with the target spin direction nearly parallel to the 3-momentum transfer vector $\mathbf{q}$ ($\theta^* = 8.9°, 171.1°$), i.e., $A_{T'}$ kinematics, has been measured in the MEPS spectrometer. The raw experimental quasielastic asymmetry is calculated by

$$A_{exp} = \frac{N_+ - N_-}{N_+ + N_-}, \tag{4.21}$$

where N_+, and N_- are the normalized (w.r.t. the beam charge) good electron events (defined by the experimental cuts discussed in Section 4.1) for positive and negative electron helicities, respectively.

The physics asymmetry $A_{T'}$ is calculated from the raw experimental asymmetry as follows:

$$A_{T'} = \frac{1}{P_t P_b} A_{exp} \left(\frac{1}{1 - d_{empty} - d_{eltail}}\right) - A_{eltail} \left(\frac{d_{eltail}}{1 - d_{empty} - d_{eltail}}\right) + \Delta A_{rad}, \tag{4.22}$$

where ΔA_{rad} is the correction to the experimental asymmetry due to the quasielastic

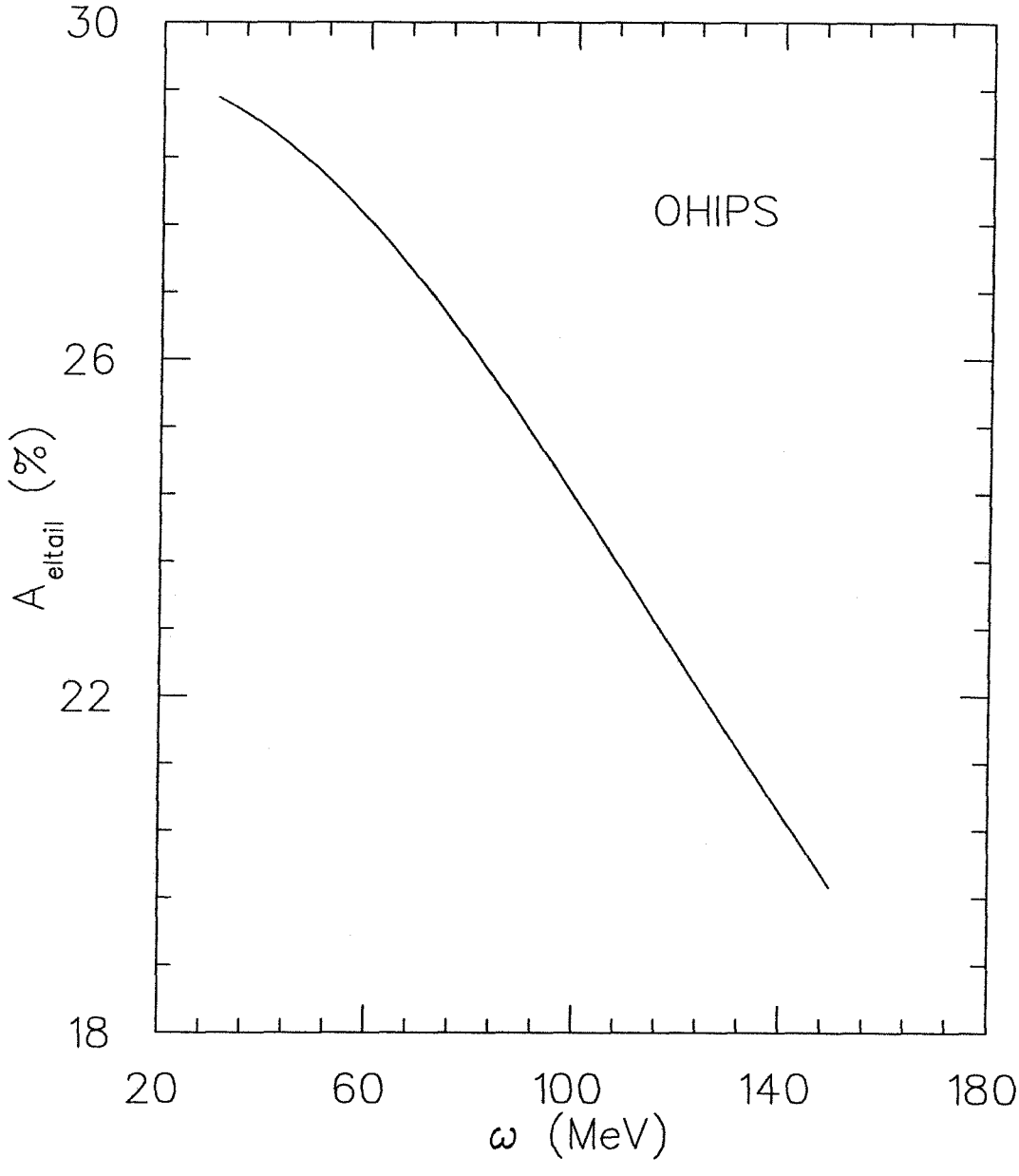

Figure 4.15: Calculated asymmetry in the elastic radiative tail as a function of ω at the OHIPS kinematics for an incident electron beam energy of 370 MeV and a target spin angle of 42.5° to the right of the electron beam.

radiative effects which is computable in quasielastic kinematics near the top of the peak. All the other terms in the above equation are the same as those in Eq. 4.16. Fig. 4.16 shows the calculated asymmetry as a function of ω in the elastic radiative tail at the MEPS kinematics.

Theoretical calculations of the helicity-dependent cross section for quasielastic scattering, from which the quasielastic asymmetry is obtained, assume single photon exchange in the scattering process. In practice, the measured cross section includes effects from higher order processes such as bremsstrahlung and energy straggling. Just as radiative corrections have to be applied to the measured cross section for comparison with theoretical calculations, so must the measured quasielastic asymmetry be corrected for radiative effects.

We will follow the notation described in [47] in calculating the asymmetry correction due to the quasielastic radiative effects, ΔA_{rad}. We will use the following shorthand notation, σ_{rad}, to denote the quasielastic cross section including radiative effects, and σ to denote the cross section assuming single photon exchange. As usual, $+$ $(-)$ refers to positive (negative) helicity electrons. The calculated asymmetry to which we wish to compare the experimental results involves single photon exchange,

$$A = \frac{\sigma_+ - \sigma_-}{\sigma_+ + \sigma_-}, \tag{4.23}$$

and the quasielastic asymmetry including radiative effects is

$$A_{rad} = \frac{\sigma_{rad+} - \sigma_{rad-}}{\sigma_{rad+} + \sigma_{rad-}}. \tag{4.24}$$

We can write

$$A = \frac{R_+\sigma_{rad+} - R_-\sigma_{rad-}}{R_+\sigma_{rad+} + R_-\sigma_{rad-}}, \tag{4.25}$$

where

$$R_{+(-)} \equiv \frac{\sigma_{+(-)}}{\sigma_{rad+(-)}}. \tag{4.26}$$

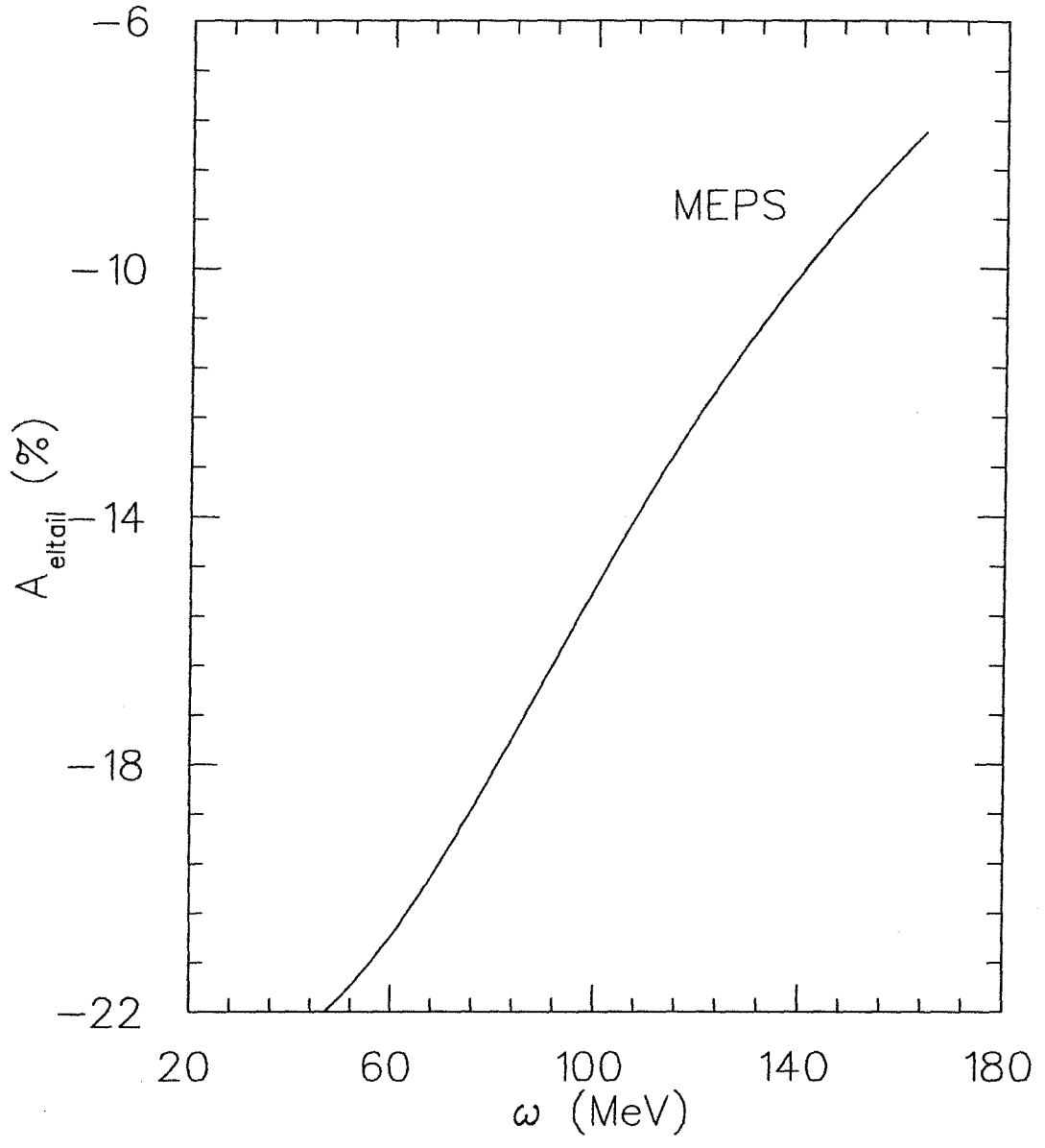

Figure 4.16: Calculated asymmetry in the elastic radiative tail as a function of ω at the MEPS kinematics for an incident electron beam energy of 370 MeV and a target spin angle of 42.5° to the right of the electron beam.

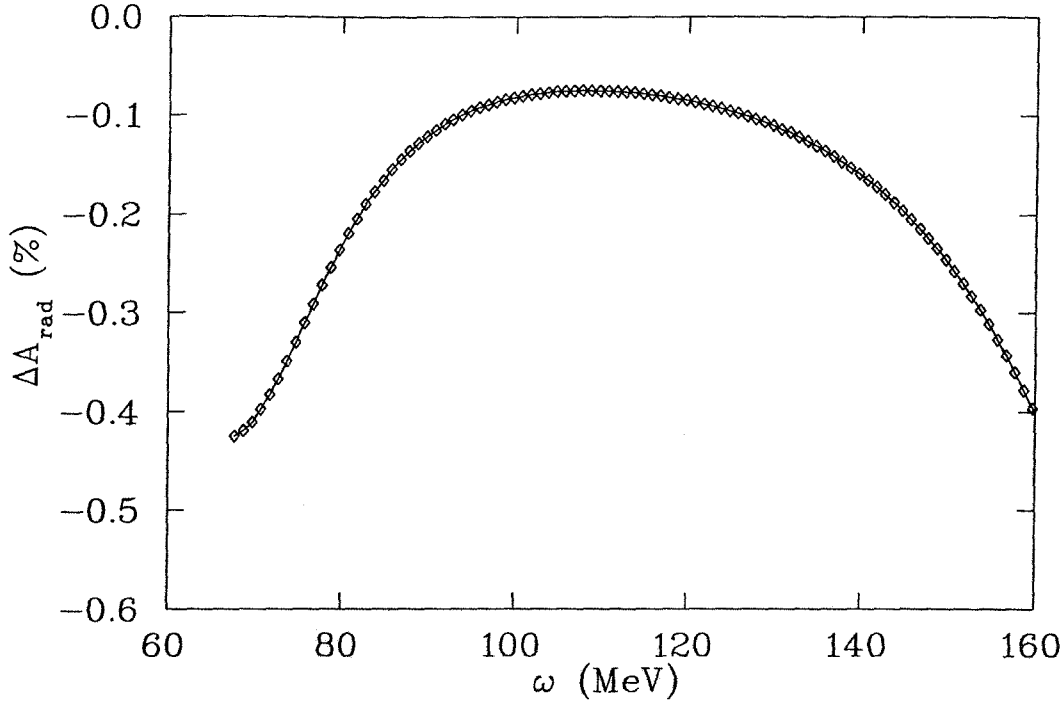

Figure 4.17: The calculated ΔA_{rad} as a function of ω at the MEPS kinematics and the electron beam energy of 370 MeV with the target spin angle being 42.5° to the right of the electron beam.

In the limit where $A \ll 1$ and the radiative correction is small, the quasielastic asymmetry can be written as

$$A = A_{rad} + \Delta A_{rad}, \tag{4.27}$$

where the asymmetry correction is

$$\Delta A_{rad} \approx \frac{1}{2}\left(\frac{R_+ - R_-}{R_+}\right). \tag{4.28}$$

The correction factors, R_+ and R_-, are calculated using the procedure of Mo and Tsai [79] for inelastic scattering, and a y-scaling calculation for the model quasielastic cross section. Fig. 4.17 shows the calculated ΔA_{rad} as a function of ω at the MEPS kinematics with target spin angle being 42.5° to the right of the electron beam. In the MEPS ω acceptance range (92 MeV $\leq \omega \leq$ 148 MeV), the asymmetry correction

due to the quasielastic radiative effects is about 1% of the size of the measured asymmetry.

Chapter 5

Systematic Uncertainties

For helicity-dependent asymmetry measurements, any helicity-correlated variation in the system will cause a systematic uncertainty in the measured asymmetry. The helicity-correlated variations must be studied carefully and their contributions to the measured asymmetry need to be estimated. In this section, we will study the helicity-correlated beam current shift, beam motion, as well as the helicity-correlated VDCX efficiency variation. The systematic uncertainties in the measured asymmetry due to the uncertainties in determining the target and beam polarizations have been addressed in the relevant chapters and will not be repeated here. The remaining systematic uncertainties in the measured asymmetry come from the empty-target background subtraction, pion contamination, the elastic radiative tail correction, and the quasielastic radiative effects. The empty-target asymmetry and the pion contamination will be discussed under the category of non-helicity-correlated systematic uncertainties.

5.1 Helicity-Correlated Beam Current Shift

The beam loading effect is a well known phenomenon associated with an accelerator for which the beam energy obtained varies slightly with the intensity of the beam

pulse. If there is a helicity-correlated beam charge difference for the beam pulse, there will be an asymmetry contribution to the experimental asymmetry from the helicity-correlated beam energy shift due to the beam loading effect, as the physical cross section is energy dependent. The single-pass beam was used for this work which corresponded to $\frac{dE}{dI} \sim 2.3$ MeV/mA for the Bates machine. The relative helicity-correlated beam current shift is calculated by

$$\frac{\Delta I}{I} = 2 \left\{ \frac{\left(\frac{\text{charge}}{\text{beam-burst}}\right)_+ - \left(\frac{\text{charge}}{\text{beam-burst}}\right)_-}{\left(\frac{\text{charge}}{\text{beam-burst}}\right)_+ + \left(\frac{\text{charge}}{\text{beam-burst}}\right)_-} \right\}, \tag{5.1}$$

where $+$ and $-$ correspond to positive and negative electron helicity states, respectively.

Fig. 5.1 shows the calculated relative current shift vs. run numbers. Runs 101, 102, 127, 217, 393 were not included in this analysis as there were significant helicity-correlated beam motions or current shifts associated with these runs and they were not used in extracting the ^{3}He asymmetries. Less than 1% of the data were thrown away by this test. The average helicity-correlated current shift weighted by the beam charge in each run from this analysis is $\frac{\Delta I}{I} = 23.3 \pm 324.6$ ppm. The total accumulated beam charge for this analysis is 26.2 Coulombs. The average beam peak current during the experiment was around 2.5 mA; the size of the contribution to the measured asymmetry from this helicity-correlated beam current variation has been estimated to be approximately four orders of magnitude smaller than the measured asymmetry.

5.2 Helicity-Correlated Beam Motion

It was mentioned earlier (Section 4.2.1) that the empty target background was dependent on the beam position on the target, even though it was not very sensitive as long as the beam position is not too far away from its nominal position. If there were helicity-correlated beam motion, then there would be an asymmetry contribution to

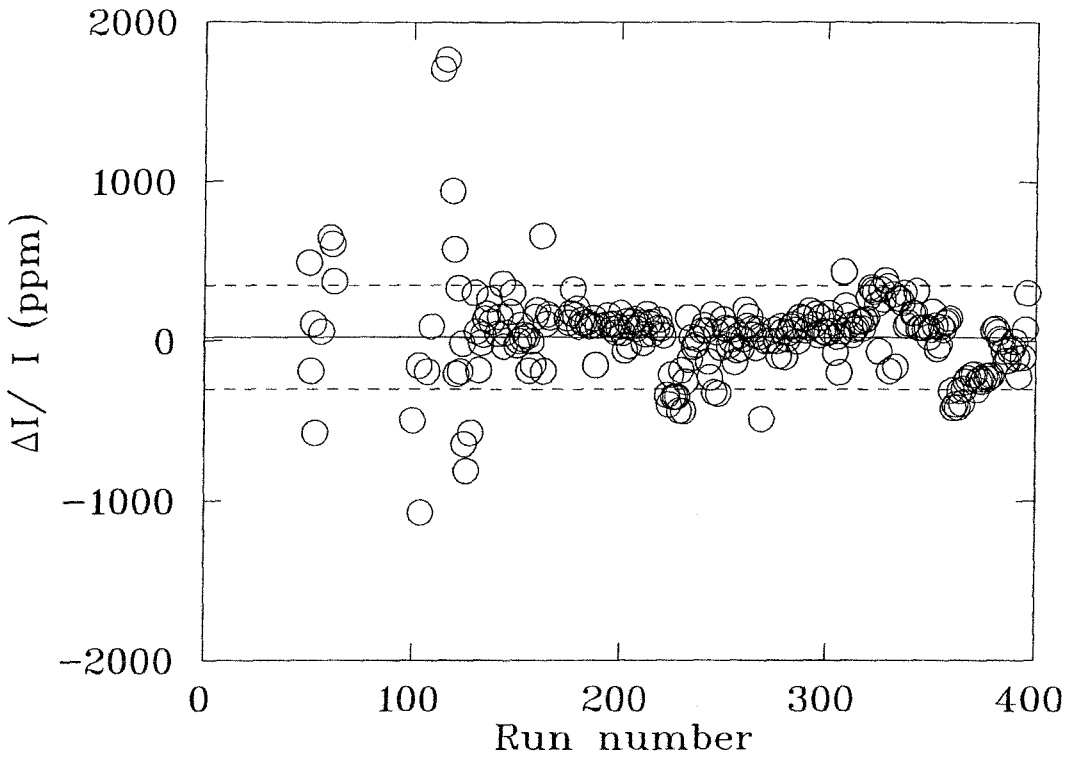

Figure 5.1: Helicity-correlated current shift.

the measured asymmetry from this beam motion as the empty target yield would be different for each of the electron helicities.

Two sets of beam position monitors (BPM) were employed to monitor the beam x and y positions with one BPM positioned upstream of the Møller target and the other one upstream of the ^{3}He target. The helicity-correlated x and y beam motions have been calculated for all the runs used in extracting the ^{3}He asymmetry (except for run 101, 102, 127, 217, 393). The BPMs were calibrated carefully during the experiment in terms of μm/channel for x and y dimensions. For calculating the helicity-correlated beam motion, the information from the target BPM has been used. Fig. 5.2 shows the calculated helicity-correlated beam x and y motions vs. run numbers for both of the target spin directions ($\beta^* = 42.5°$ to the beam right, and 137.5° to the beam left). Table 5.1 lists the helicity-correlated beam motions.

The empty target yield vs. beam position x and y was studied carefully during

Δx (μ m)	Δy (μ m)
-0.20 ± 1.06	0.08 ± 1.14

Table 5.1: Calculated average helicity-correlated beam motion.

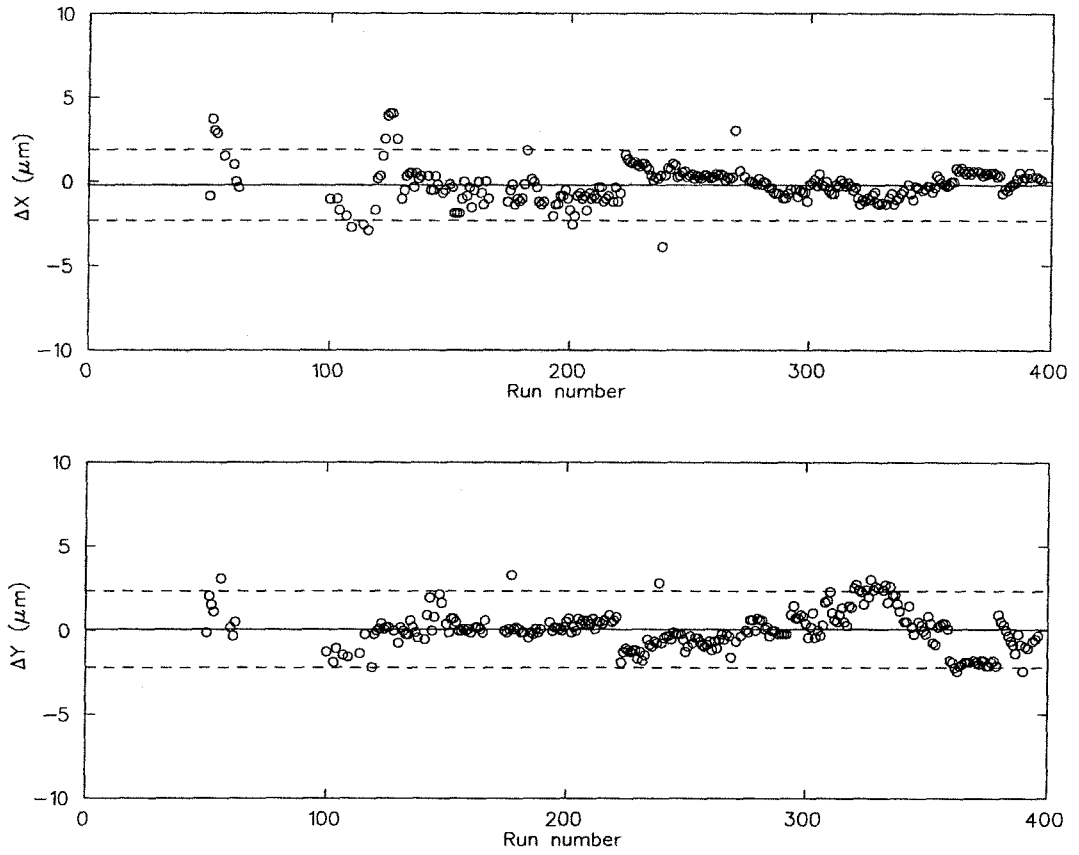

Figure 5.2: Helicity-correlated beam position shifts. The top plot is Δx and the bottom plot is Δy.

the experiment at the OHIPS and MEPS quasielastic kinematics. The measured empty target rates have been fit using a parabolic functional form with respect to either x or y. The empty target rates can be written in terms of the following fit parameters:

$$R(x) = R(x_0) + \frac{dR}{dx}\Delta x + \frac{d^2R}{dx^2}\Delta x^2, \tag{5.2}$$

$$R(y) = R(y_0) + \frac{dR}{dy}\Delta y + \frac{d^2R}{dy^2}\Delta y^2, \tag{5.3}$$

where x_0 and y_0 are the nominal beam position at which the empty target yield is at minimum; x and y denote the arbitrary beam position. Δx and Δy are the deviations of the beam position w.r.t the nominal position, and all the rest of the quantities in the above equations are the fit values. The asymmetry contribution from these helicity-correlated beam shifts to the measured asymmetry are calculated using the fit parameters described above as follows:

$$A_x = \frac{d_{empty}}{P_t P_b}\left(\frac{(\frac{dR}{dx})\Delta x + (\frac{d^2R}{dx^2})\Delta x^2}{2R(0)}\right), \tag{5.4}$$

$$A_y = \frac{d_{empty}}{P_t P_b}\left(\frac{(\frac{dR}{dy})\Delta y + (\frac{d^2R}{dy^2})\Delta y^2}{2R(0)}\right), \tag{5.5}$$

where $\frac{d_{empty}}{P_b P_t}$ is the dilution factor from the empty target yield vs. the full target yield, and P_t and P_b are the target and beam polarizations. Table 5.2 shows the calculated asymmetry contributions at the OHIPS and the MEPS quasielastic kinematics to the measured asymmetry, where MEPS (1,2) stands for the two quasielastic spectrometer settings. The calculated asymmetry contributions due to the helicity-correlated beam motion are approximately four orders of magnitude smaller than the measured asymmetry. The asymmetry contributions due to the helicity-correlated beam motion at the OHIPS elastic and elastic-threshold kinematics are expected to be negligible compared to the measured asymmetries, though there were no data taken for empty target background vs. beam position at these two kinematics.

spectrometer	A_x (%)	A_y (%)
OHIPS	$7.24E-04 \pm 3.75E-03$	$1.89E-04 \pm 2.57E-03$
MEPS (1)	$1.14E-03 \pm 1.74E-02$	$1.01E-03 \pm 4.39E-03$
MEPS (2)	$2.92E-03 \pm 1.03E-02$	$2.23E-04 \pm 6.17E-03$

Table 5.2: Calculated asymmetry contribution due to the helicity-correlated beam motion.

5.3 Helicity-Correlated VDCX Efficiency Variation

The helicity-correlated OHIPS VDCX efficiency variation has been studied for all the runs. Fig. 5.3 shows the relative helicity-correlated chamber efficiency variation vs. run numbers for all the full target runs, and empty target runs, separately. The weighted average of the relative chamber efficiency variation is $0.03 \pm 0.90\%$ for the full target runs, and $-1.34 \pm 4.82\%$ for the empty target runs. MEPS VDCX did not have the delay-line readout system, the TDC-per-wire readout system was much simpler and the overall chamber efficiency was much higher and stable than that of for OHIPS. The helicity-correlated MEPS chamber efficiency variation is expected to be smaller than that of the OHIPS.

5.4 Non-Helicity-Correlated Systematics

5.4.1 Empty Target Asymmetry

The empty target asymmetry has been calculated for all the empty target runs in the MEPS and OHIPS spectrometers using

$$A_{empty} = \frac{1}{\bar{P}_b \bar{P}_t} \left(\frac{N_+ - N_-}{N_+ + N_-} \right), \tag{5.6}$$

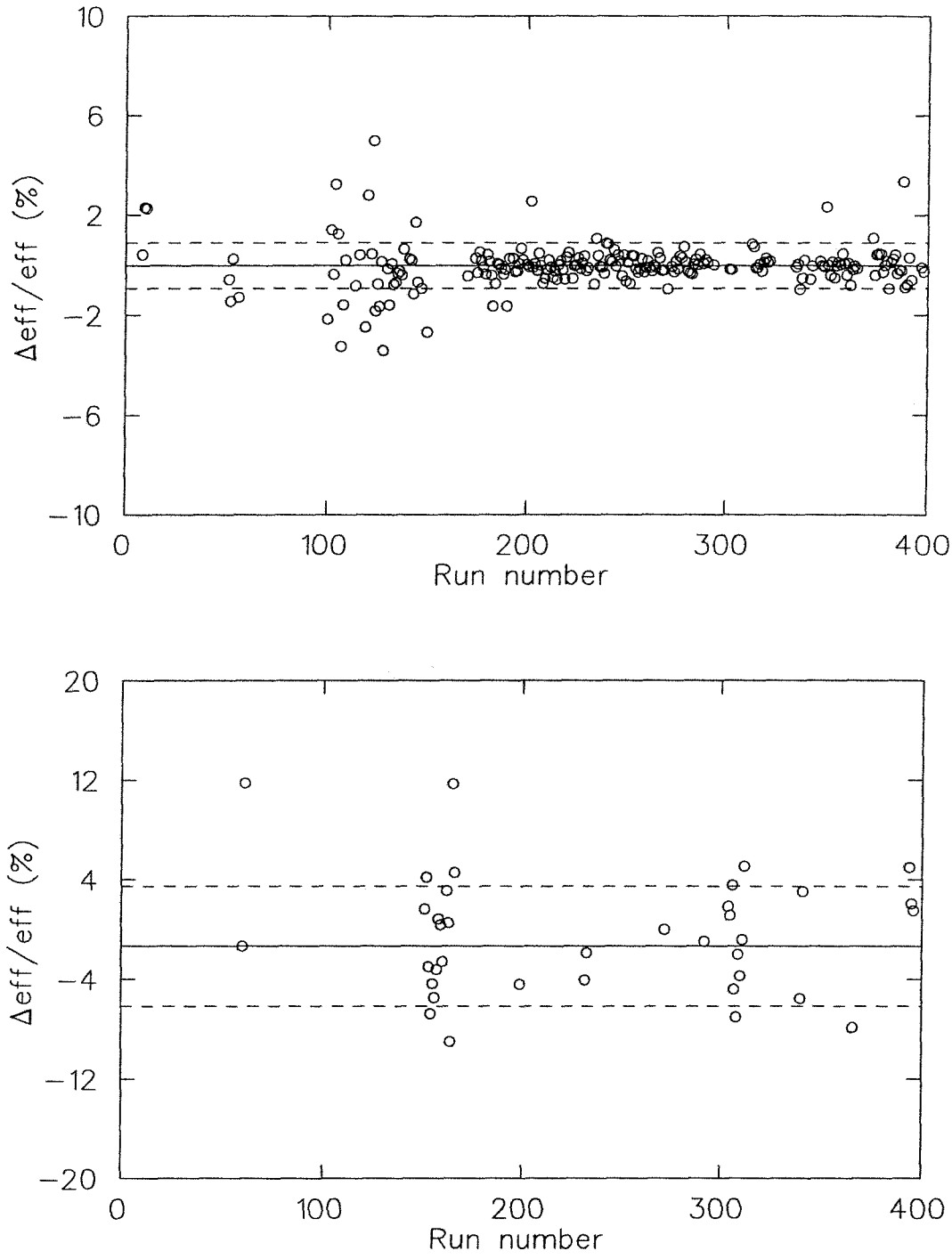

Figure 5.3: Helicity-correlated OHIPS VDCX efficiency variation. The top plot is for all the full target runs and the bottom plot is for all the empty target runs.

where $\bar{P}_b$ and $\bar{P}_t$ are the average beam and target polarizations from all the full target runs used in extracting the ^{3}He asymmetry. Fig. 5.4 shows the empty target asymmetry vs. empty target runs in the OHIPS and MEPS spectrometers. The weighted average of the empty target asymmetry in OHIPS is -2.2 ± 7.6 % and -5.6 ± 7.6 % in MEPS. No empty target asymmetries have been observed within statistical uncertainties.

5.4.2 Pion Contamination

The pion asymmetry has been extracted in both spectrometers in order to estimate the effect of the pion contamination to the measured ^{3}He asymmetry. The raw experimental pion asymmetry is calculated as

$$A_{exp} = \frac{1}{P_t P_b}\left(\frac{N_+ - N_-}{N_+ + N_-}\right), \tag{5.7}$$

where P_t and P_b are the target and beam polarization respectively. N_+, and N_- are the normalized good pion events defined by the experimental cuts described in Section 4.1 for positive and negative electron helicity, respectively.

The pion raw experimental asymmetry can be further written into

$$A_{exp} = \check{C}_{e\to\pi}\frac{\sigma_e}{\sigma_t}A_e + \check{C}_{e\to\pi}\frac{\sigma_{eltail}}{\sigma_t}A_{eltail} + \frac{\sigma_\pi}{\sigma_t}A_\pi, \tag{5.8}$$

$$\sigma_t = \check{C}_{e\to\pi}\sigma_e + \check{C}_{e\to\pi}\sigma_{eltail} + \sigma_\pi, \tag{5.9}$$

where $\check{C}_{e\to\pi}$ is the probability for an electron event to be misidentified as a pion event by the Čerenkov detector. σ_e is the electron quasielastic yield, σ_{eltail} is the electron yield from the elastic radiative tail, and σ_π is the pion yield. The electron asymmetry contribution due to the quasielastic radiative effects is not included in Eq. 5.8 as it is negligible.

The pion asymmetry can be extracted from the raw experimental asymmetry by

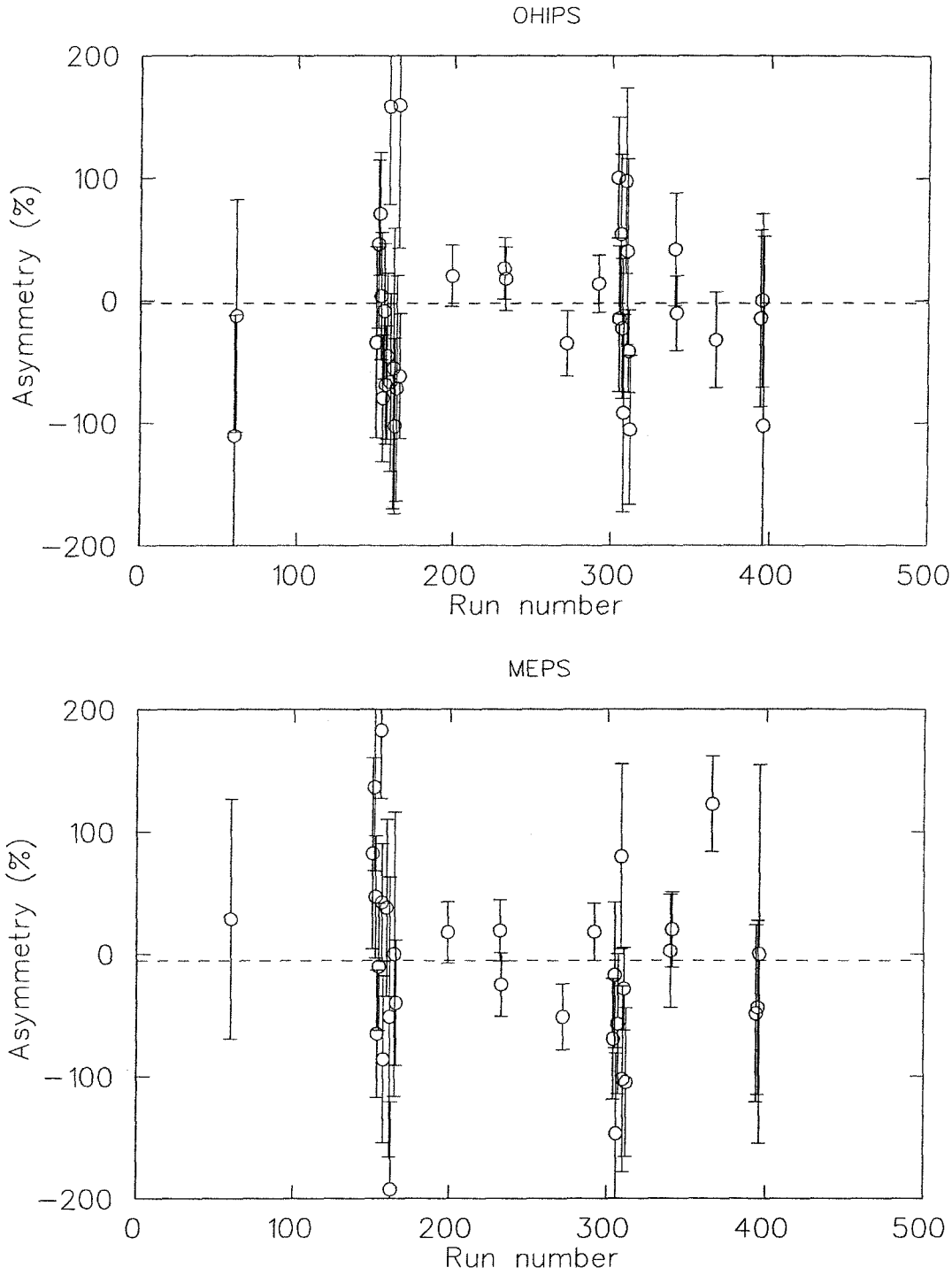

Figure 5.4: Empty target asymmetries in OHIPS and MEPS spectrometers.

inverting Eq. 5.8 as follows:

$$A_\pi = \frac{\sigma_t}{\sigma_\pi} A_{exp} - \check{C}_{e\to\pi} \frac{\sigma_e}{\sigma_\pi} A_e - \check{C}_{e\to\pi} \frac{\sigma_{eltail}}{\sigma_\pi} A_{eltail}. \tag{5.10}$$

In extracting the MEPS pion asymmetry from the measured experimental pion asymmetry, a value corresponding to 3% has been used for $\check{C}_{e\to\pi}$ and a Monte Carlo program was used to calculate the pion differential cross section at the MEPS quasielastic kinematics because of the poor statistics of the measured pion differential cross section. The measured ^{3}He quasielastic asymmetry and the cross section together with the calculated elastic radiative tail and its asymmetry have been used in Eq. 5.10 to get the pion asymmetry.

The effect of the pion contamination on the measured ^{3}He asymmetry can be calculated from the extracted pion asymmetry by:

$$A^\pi_{contam} = \check{C}_{\pi\to e} \frac{\sigma_\pi}{\sigma_t} A_\pi, \tag{5.11}$$

$$\sigma_t = \sigma_e + \sigma_{eltail} + \check{C}_{\pi\to e}\sigma_\pi, \tag{5.12}$$

where $\check{C}_{\pi\to e}$ is the probability that a pion event is misidentified as an electron event by the Čerenkov counter. It is 3% for the MEPS Čerenkov detector and 5% for the OHIPS Čerenkov counter. Fig. 5.5 shows the calculated effect of the pion contamination to the measured ^{3}He quasielastic asymmetry in the MEPS spectrometer as a function of the electron energy loss ω. The pion contamination in the MEPS spectrometer averaged over the ω acceptance is less than 0.1% of the measured ^{3}He quasielastic asymmetry. So the effect of pion contamination in the MEPS spectrometer is negligible. The effect of the pion contamination to the measured $A_{TL'}$ in the OHIPS elastic-threshold region has been found to be even more negligible.

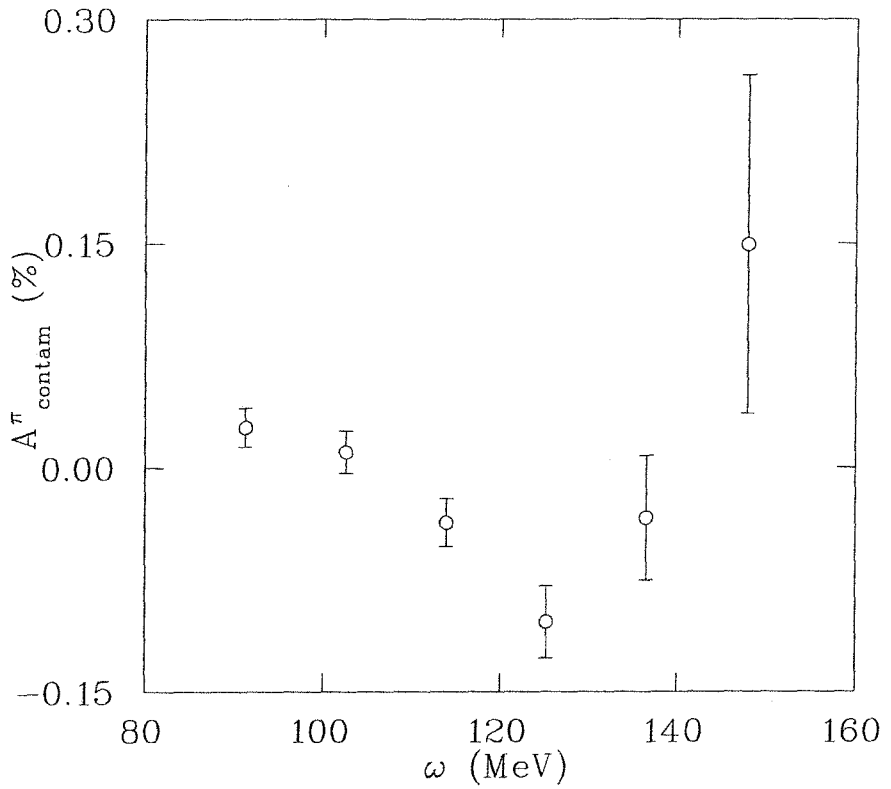

Figure 5.5: The calculated effect of the pion contamination to the measured ^{3}He quasielastic asymmetry in the MEPS spectrometer as a function of ω. The uncertainties are the statistical uncertainties only.

Chapter 6

Results

6.1 Elastic Asymmetry

The elastic asymmetry was measured in the OHIPS spectrometer as a check of the experimental procedure. The elastic asymmetry was measured in three different spectrometer central momentum settings. The measured elastic asymmetries in terms of the elastic peak positions together with the statistical uncertainties are listed in Table 6.1. The average elastic asymmetry over the three spectrometer settings gives $29.9 \pm 3.5\%$ with the uncertainty being the statistical uncertainty from the measurements.

The systematic uncertainty of the elastic asymmetry measurement is dominated

Elastic peak position $\delta(\%)$	A (%)	Δ A (%)
-1	36.45	8.03
2.5	28.74	5.81
3.3	28.04	5.12
combined	29.9	3.5

Table 6.1: Results of the OHIPS elastic asymmetry in terms of three different spectrometer settings. The measured elastic asymmetry with statistical uncertainty is listed with respect to its elastic peak position. The average asymmetry is also listed.

Sources	$\frac{\Delta A}{A}$ (%)
beam polarization	4
target polarization	3
empty target subtraction	1.5
hel-corr. efficiency variation	≤ 1
overall	5.5

Table 6.2: Systematic uncertainties of the OHIPS elastic asymmetry in terms of different sources. The overall systematic uncertainty is 5.5%.

by the uncertainties in the determination of the beam and the target polarizations. Table 6.2 lists the systematic uncertainties in terms of different sources and the overall systematic uncertainty is also listed. The measured OHIPS elastic asymmetry is $29.9 \pm 3.9\%$ with the uncertainty being the total uncertainty determined by the quadrature sum of the statistical and systematic uncertainties. The elastic asymmetry can be calculated using ^{3}He form factors measured by Rosenbluth separation (see Eq. 4.16). The calculated asymmetry is 29.2% using the ^{3}He form factors measured by McCarthy *et al.* [81] and is 32.2% using the measurement by Dunn *et al.* [84]. The measured elastic asymmetry is in excellent agreement with the calculated values.

6.2 Quasielastic Transverse Asymmetry $A_{T'}$

The ^{3}He quasielastic transverse asymmetry, $A_{T'}$, has been extracted from the MEPS spin-dependent quasielastic inclusive cross section as a function of the electron energy loss ω for a total beam charge of 6529 μA-h. Corrections have been made for the empty target background, the elastic radiative tail and the quasielastic radiative effect as discussed in Section 4.4.3. The measured quasielastic transverse asymmetry $A_{T'}(\omega)$ is shown in Fig. 6.1 along with calculations at the MEPS quasielastic kinematics by Salmè *et al.* (Gari-Krüpelmann form factor parametrization) [25] and

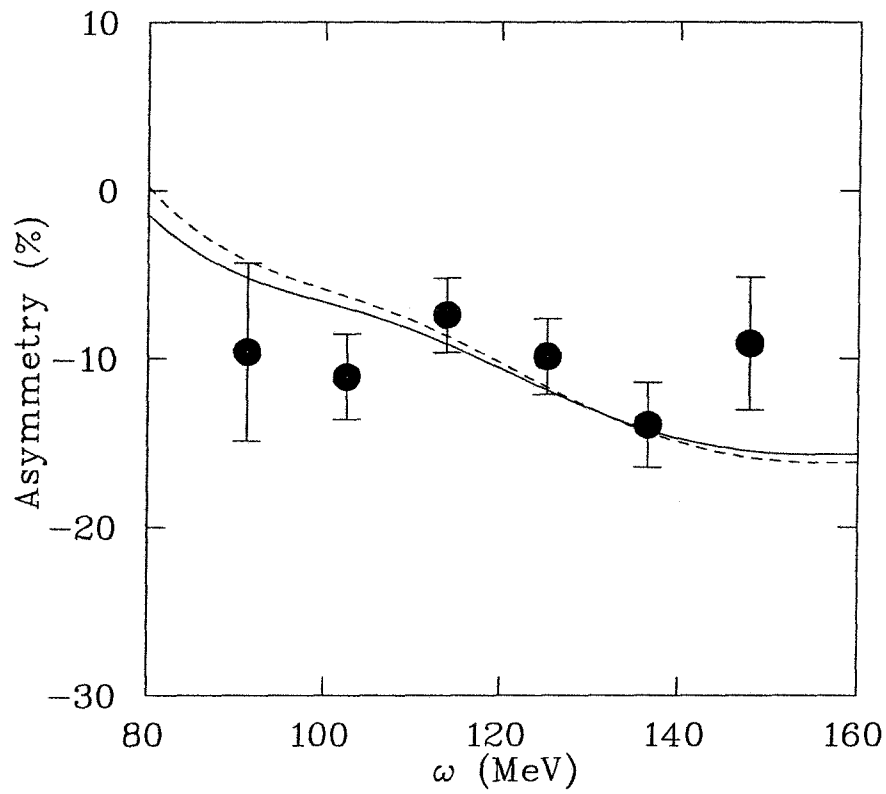

Figure 6.1: The transverse asymmetry $A_{T'}$ as a function of electron energy loss ω. The solid circles are the data points from the present work with statistical uncertainties only. The dashed line is the calculation by Salmè *et al.* [25], and the solid line is the calculation by Schulze *et al.* [23].

Sources	$\frac{\Delta A}{A}$ (%)
beam polarization	4
target polarization	3
empty target subtraction	1.5
hel-corr. efficiency variation	≤ 1
elastic radiative tail	0.4
QE radiative correction	0.2
pion contamination	0.1
overall	5.5

Table 6.3: Systematic uncertainties of the MEPS quasielastic transverse asymmetry $A_{T'}$ in terms of different sources. The overall systematic uncertainty is 5.5%.

Schulze *et al.* (Galster parametrization) [23]. It is thought that the difference between the two calculations arises from the different ^{3}He wave functions and form factor parametrizations used in the calculations. The data are in good agreement with both calculations.

The MEPS spectrometer had an electron scattering angle acceptance of 7° defined by the collimator placed in front of the first quadrupole. The effect of the spectrometer scattering angle acceptance on the calculated $A_{T'}$ averaged over the experimental ω acceptance by Salmè *et al.* [25] and Schulze *et al.* [23] have been determined to be less than 0.4% using a Monte Carlo program [85]. The target spin angle was aligned at an angle of 42.5° with respect to the electron beam line with an uncertainty of $\pm 0.5°$. The effect of this uncertainty of the target spin angle on the calculated $A_{T'}$ is negligible. Fig. 6.2 shows the dependence of $A_{T'}$ on the electron scattering angle θ and the target spin angle β using the calculation of Schulze *et al.* [23] in which the form factor parametrization of Galster is used.

Again the systematic uncertainty for the measurement of $A_{T'}$ is dominated by the uncertainties in the determination of the beam and target polarizations. Table 6.3 lists the systematic uncertainties for MEPS $A_{T'}$ in terms of the sources and the overall systematic uncertainty is also listed.

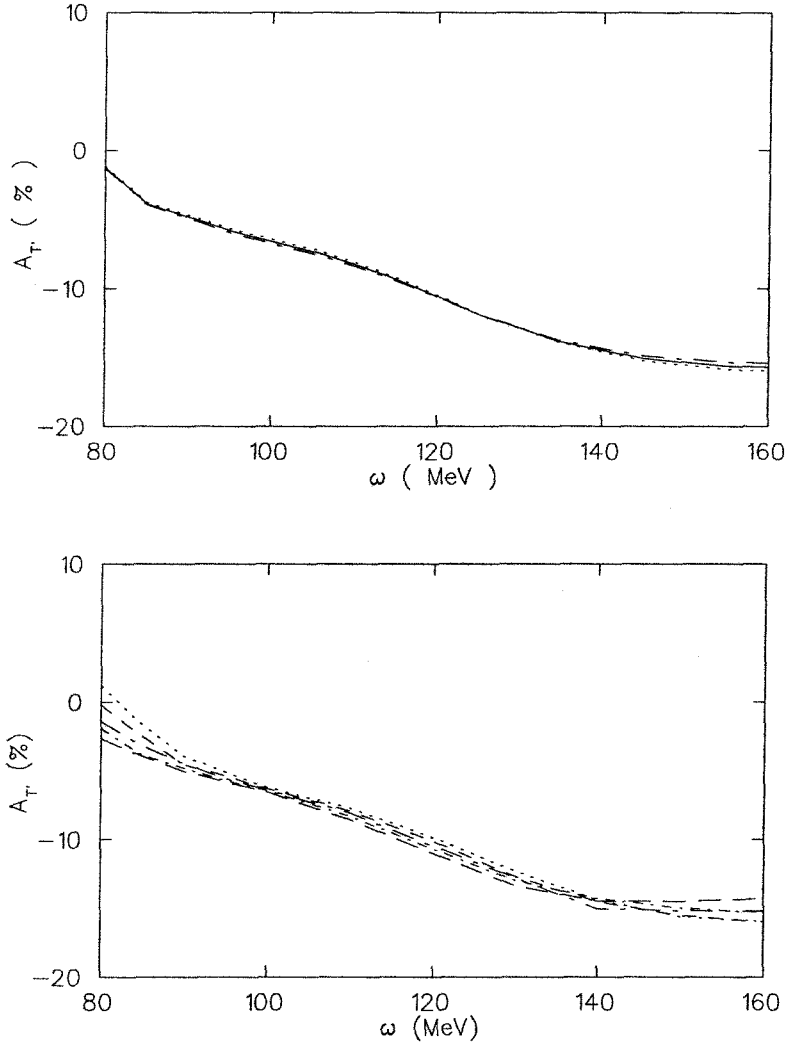

Figure 6.2: Dependence of $A_{T'}$ on scattering angle, θ and target spin angle, β using the calculation of Schulze *et al.* [23]. The dependence of $A_{T'}$ on β is plotted in the top plot in which β is 42.5° (solid line), 45° (dash-dotted line) and β is 40° (dotted line). The bottom plot shows the calculated $A_{T'}$ vs. different scattering angles. θ is from 87° to 95° in 2° steps. The dotted line corresponds to $\theta = 95°$ and the long-dashed line corresponds to $\theta = 87°$.

Charge (μA-h)	θ^* (deg)	ϕ^* (deg)	A (%)
3956	8.9	180	-10.66 ± 1.40
2573	171.1	0	9.51 ± 1.81
6529 (combined)			$-10.23 \pm 1.11 \pm 0.56$
Theory [25]	8.9	180	-9.85
Theory [23]	8.9	180	-10.09

Table 6.4: Results of MEPS quasielastic transverse asymmetry $A_{T'}$ averaged over the spectrometer acceptance. The measured asymmetries for each of the target spin direction are listed separately and the sign change corresponds to the flipping of the target spin direction.

The measured asymmetry averaged over the experimental ω acceptance corresponding to $Q^2 = 0.19(\mathrm{GeV/c})^2$, together with the calculated asymmetry averaged over the spectrometer acceptance and weighted by the quasielastic cross section from [25] [23], are listed in Table 6.4. The uncertainties listed for the measured asymmetry for each of the target spin direction are the statistical uncertainties only. The sign change in the measured asymmetry corresponds to a flip in the target spin direction. The uncertainties listed for the combined measured asymmetry are the statistical and systematic uncertainty, respectively.

6.3 Extraction of the Neutron Magnetic Form Factor G_M^n

The measured ^{3}He quasielastic transverse asymmetry at $Q^2 = 0.19$ $(\mathrm{GeV/c})^2$ is $-10.23 \pm 1.11 \pm 0.56$ % with the uncertainties being the statistical and systematic uncertainties, respectively. As we have discussed in Chapter 1, a measurement of the ^{3}He quasielastic transverse asymmetry, $A_{T'}$, can be used to extract the neutron magnetic form factor as $A_{T'}$ is very sensitive to the square of the neutron magnetic form factor, ${G_M^n}^2$. To determine ${G_M^n}^2$ from the measured asymmetry, the calculations

calculation	a	b	c
Salmè *et al.*	-752.10	99.76	2.01
Schulze *et al.*	-804.56	99.88	8.97

Table 6.5: The fit parameters for extracting ${G_M^n}^2$ using the calculations of Salmè *et al.* [25] and Schulze *et al.* [23].

of Salmè *et al.* [25] and Schulze *et al.* [23] have been used to generate $A_{T'}({G_M^n}^2)$ independently, where $A_{T'}$ has been averaged over the experimental ω acceptance and weighted by the quasielastic cross section. The calculated $A_{T'}({G_M^n}^2)$ values are then related to ${G_M^n}^2$ using the following functional form:

$$A_{T'}({G_M^n}^2) = \frac{1 + a{G_M^n}^2}{b + c{G_M^n}^2}. \tag{6.1}$$

Two fits are obtained in this way using the two calculations mentioned above and the fits are then used to extract ${G_M^n}^2$ based on the measured asymmetry. Table 6.5 lists the fit parameters obtained using the calculations of Salmè *et al.* [25] and Schulze *et al.* [23].

The extracted ${G_M^n}^2$ values at Q^2 =0.19 (GeV/c)^2 agree within 3% for the two calculations. Fig. 6.3 shows the two fits obtained together with the measured $A_{T'}$ with its statistical uncertainty plotted on each fit separately indicating the extracted ${G_M^n}^2$ value from the corresponding fit.

In units of $(\mu_n G_D)^2$, the standard dipole parametrization, the average of the two extracted ${G_M^n}^2$ values discussed above gives $(G_M^n/\mu_n G_D)^2 = 0.998 \pm 0.117 \pm 0.059 \pm 0.030$, with the uncertainties corresponding to the statistics, systematics and model dependence, respectively. The systematic uncertainty is dominated by the uncertainties in the determination of the beam polarization ($\pm$4%) and the target polarization ($\pm$3%). The uncertainty from the model dependence of the extracted ${G_M^n}^2$ arises from both the uncertainty in the ^{3}He wave function and the uncertainty in the proton electromagnetic form factors involved in the calculations. The wave

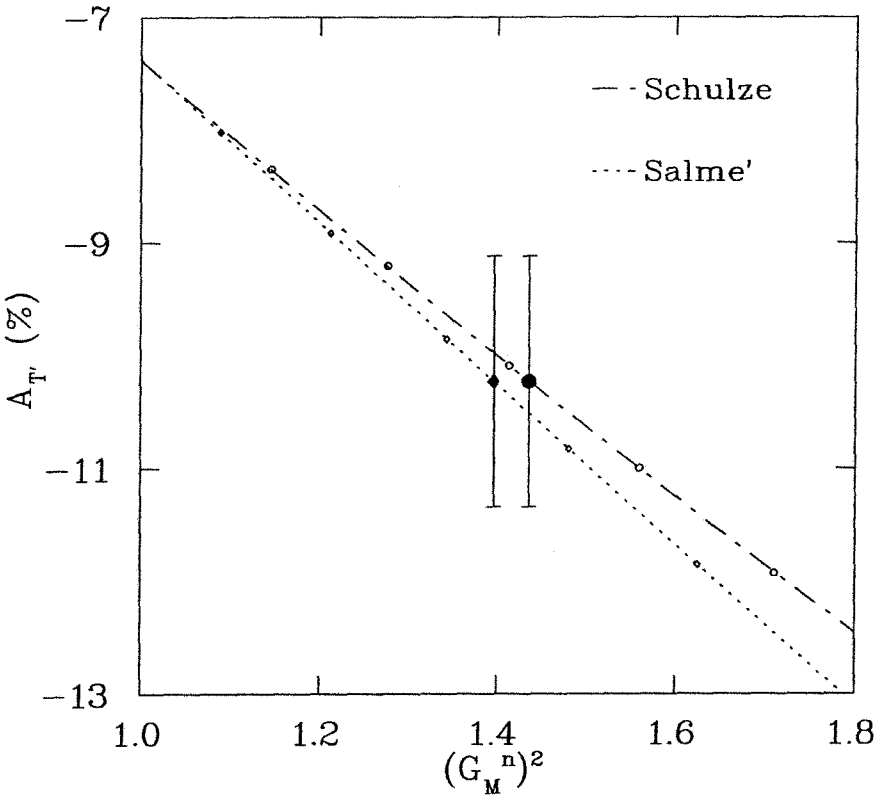

Figure 6.3: Fits of $A_{T'}$ vs. ${G_M^n}^2$ obtained using the calculations of Salmè *et al.* [25] and Schulze *et al.* [23]. The dotted line is the fit for the calculation of Salmè *et al.*, and the dash-dotted line is the fit obtained using the calculation of Schulze *et al.* The measured $A_{T'}$ is also plotted together with its statistical uncertainty on each fit separately which indicates the extracted ${G_M^n}^2$ value from the measured $A_{T'}$ using each fit.

function uncertainty was estimated from calculations by Salmè *et al.* [25] using the variational wave function from the Reid soft-core interaction and by Schulze *et al.* [23] using the Faddeev wavefunction from the Paris potential.

To estimate the uncertainty due to proton form factors, the ^{3}He quasielastic asymmetry calculation of Frair *et al.* [3] has been used for the MEPS kinematics using the form factor parametrizations of Höhler [19], Gari-Krümpelmann [20], Galster [8], and Iachello-Jackson-Lande [86]. In the model of Friar *et al.* [3], the ^{3}He quasielastic asymmetry is calculated in terms of the neutron and proton contributions:

$$A = (1 - 2\delta)\frac{\sigma_n}{\sigma_n + 2\sigma_p} A_{\vec{e}\vec{n}} - 2\delta' \frac{2\sigma_p}{\sigma_n + 2\sigma_p} A_{\vec{e}\vec{p}}, \tag{6.2}$$

$$\delta \approx 0.07 \pm 0.01, \tag{6.3}$$

$$\delta' \approx 0.014 \pm 0.002, \tag{6.4}$$

where σ_n, σ_p are the elastic electron-neutron and electron-proton cross section respectively. The same procedure as described in the beginning of this section has been used to generate $A_{T'}(G_M^n{}^2)$ at $Q^2 = 0.19$ GeV/c^2 using the calculation of Friar *et al.* [3] first and then the calculated $A_{T'}(G_M^n{}^2)$ values have been fitted to $G_M^n{}^2$ using Equation 6.1 for different form factor parametrizations as mentioned above. Table 6.6 lists the fit parameters for the calculation of Friar *et al.* [3] using the form factor parametrizations of Höhler [19], Gari-Krümpelmann [20], Galster [8], and Iachello-Jackson-Lande [86]. The form factor parametrization of Blatnik-Zovko [26] is not included in the analysis mentioned above as it does not describe the proton electric form factor data well in the low Q^2 region where this work is relevant.

Using the model of Friar *et al.* [3], the uncertainty due to the proton form factor has been found to be 3%, and it dominates the uncertainty due to model dependence. An overall 3% uncertainty due to model dependence is assigned to the extracted $G_M^n{}^2$.

The extracted $G_M^n{}^2$ value from this experiment at $Q^2 = 0.19$ (GeV/c)^2 is shown

form factor parametrization	a	b	c
Galster	-712.0	100.0	9.3
Gari-Krüpelmann	-730.6	99.9	10.0
Höhler	-734.9	99.7	10.0
Iachello-Jackson-Lande	-735.7	99.8	9.8

Table 6.6: Fit parameters vs. form factor parametrizations using the calculation of Friar *et al.*.

in Fig. 6.4 with its total uncertainty determined by adding all three uncertainties in quadrature. Plotted also are the previous published data on ${G_M^n}^2$ from the electron-deuteron experiments in the low Q^2 region. The uncertainties in the inclusive data from Hughes *et al.* [12] include a global 5% theoretical uncertainty. The uncertainties in the data from [13-18] do not include a theoretical uncertainty. The recent data of Markowitz *et al.* [9] include a theoretical uncertainty of 3%. The Gari-Krümpelmann [20] and Höhler [19] form factor parametrizations are also shown in Fig. 6.4. The extracted ${G_M^n}^2$ at $Q^2 = 0.19$ (GeV/c)^2 from the present work agrees with the dipole parametrization very well and the overall error bar indicates that this technique provides a competitive technique for measuring G_M^n.

6.4 $A_{TL'}$ in the Elastic-Threshold Region

As was mentioned earlier, data on $A_{TL'}$ have been taken in the elastic-threshold region in the OHIPS spectrometer. Fig. 6.5 shows the results of $A_{TL'}$ as a function of electron energy loss ω together with the experimental cross section in the elastic-threshold region (so-called low ω region). The energy scale is tied with the position of the elastic peak, and the beam energy determined from the spectrometer magnet settings. The uncertainties shown are the total uncertainties determined by the quadrature sum of the statistical and systematic uncertainties with the statistical uncertainties dominant. The systematic uncertainties are dominated by the uncer-

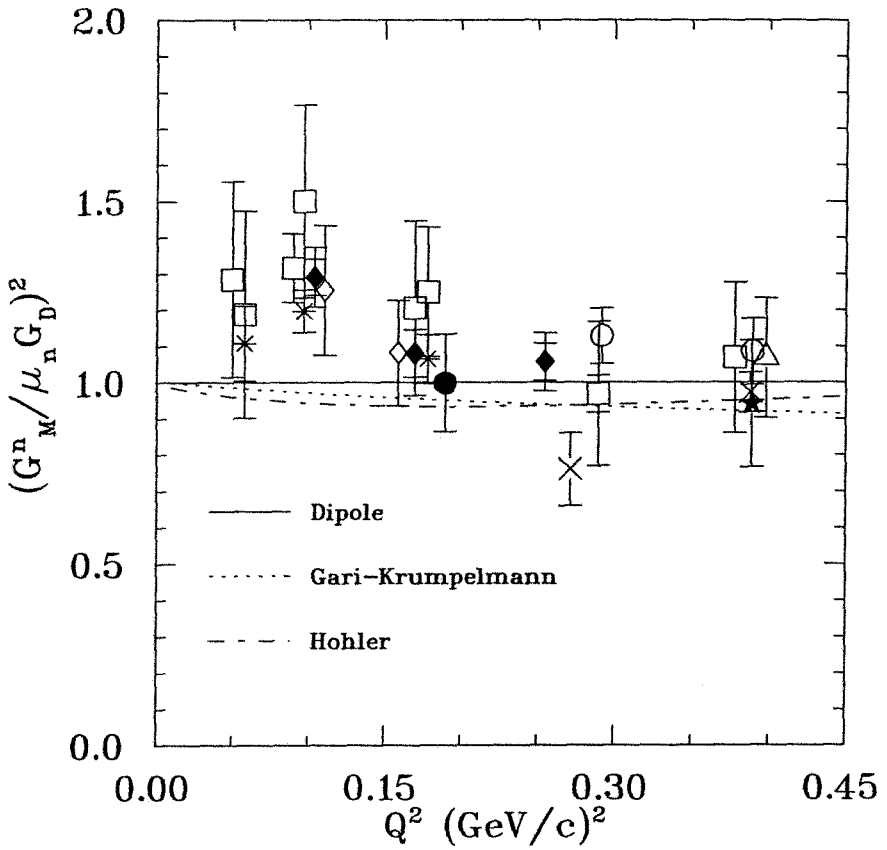

Figure 6.4: The square of the neutron magnetic form factor ${G_M^n}^2$, in units of the standard dipole parametrization, $(\mu_n G_D)^2$, in the low Q^2 region. The solid circle is from the present work shown with the total uncertainty dominated by the statistical error. The hollow squares are from Hughes *et al.* [12], the hollow diamonds are from the analysis by Kramer *et al.* [13] of the data from Grossetête *et al.* [14], the asterisks are from Braess *et al.* [13], the crosses are from Hanson *et al.* [15], the hollow circles are from Budnitz *et al.* [16], the star is from Bartel *et al.* [17], the triangle is from Stein *et al.* [18], and the solid diamonds are from Markowitz *et al.* [9] with the inner (outer) error bars being the statistical (total) uncertainties. The data of Markowitz *et al.*, Hughes *et al.*, and Stein *et al.* have been displaced slightly to improve readability.

tainties of the experimental quasielastic yield (15%), the beam polarization (4%) and the target polarization (3%), except for one point in the dip region between the elastic peak and the quasielastic tail where a 50% uncertainty has been assigned to the experimental quasielastic yield as it is most sensitive to the radiative tail subtraction.

The extraction scheme A and C [5] are indicated as solid and dotted lines in Fig. 6.5. The elastic peak position (double line), the two-body breakup threshold (dashed line) and the three-body breakup threshold (dash-dotted line) are also indicated in Fig. 6.5. The data in the tail of the quasielastic peak and away from the three-body breakup threshold agree well with the PWIA calculation using spin-dependent spectral function with extraction scheme A [5]. Scheme A is considered the favorite extraction scheme by Schulze *et al.* [5] and is agreed upon by the authors of Ref. [25]. A large positive asymmetry has been observed close to the three-body breakup threshold. There is no quantitative theoretical explanation for this. The speculation is that the large positive asymmetry is caused by the scattering of the polarized electrons from the polarized proton in the ^{3}He nucleus leaving a bound deuteron behind. While the above explanation can explain the sign and roughly the size of the observed asymmetry, it does not explain why a large asymmetry is not seen close to the two-body breakup threshold. However, the statistical precision of the data at the 2-body breakup threshold precludes a definitive statement about the physics asymmetry. On the other hand, the elastic-threshold region is a region where final state interactions and meson exchange currents could play significant roles. A more complete calculation with FSI and MEC using a spin-dependent spectral function is probably required in order to interpret these data.

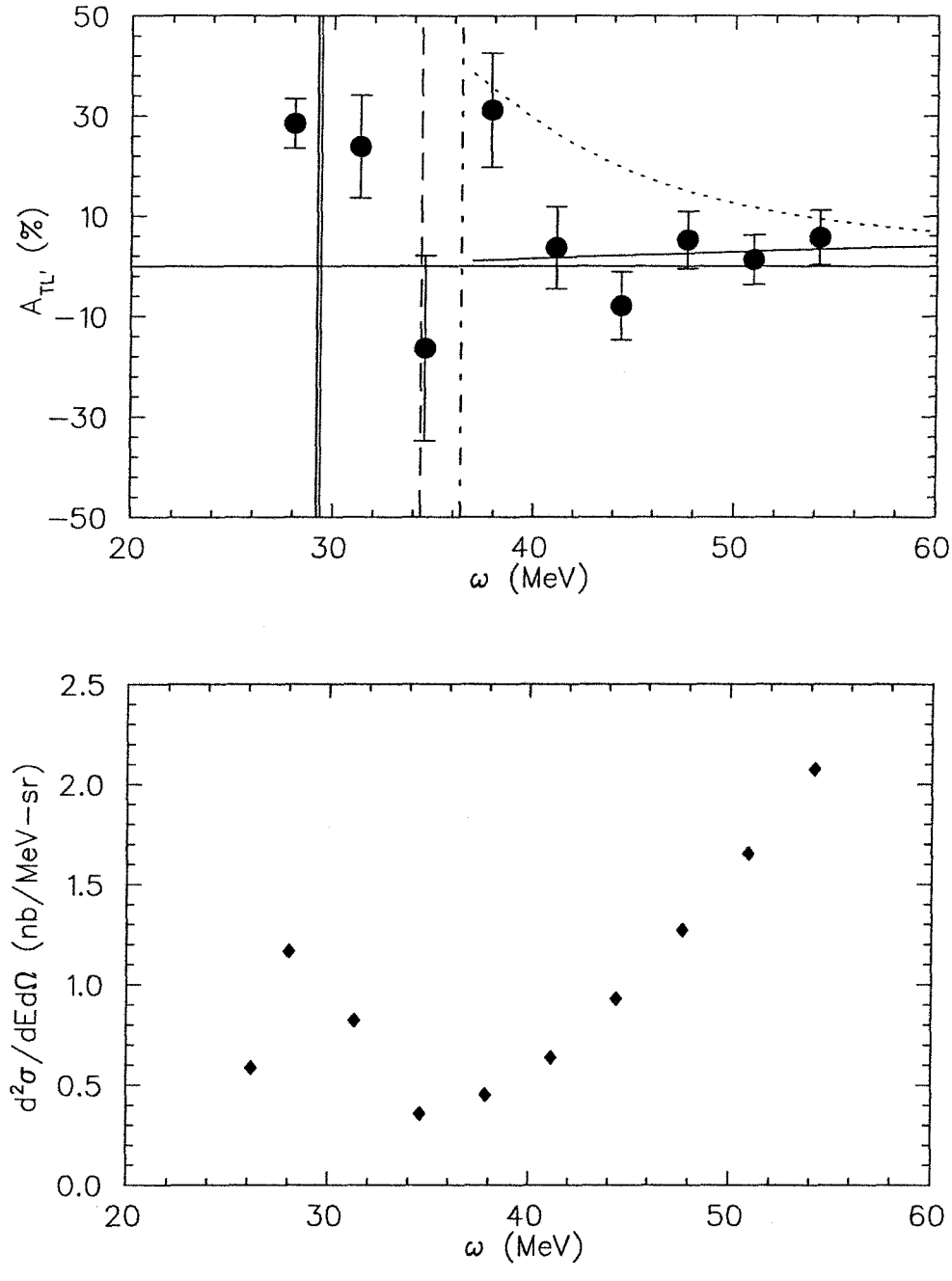

Figure 6.5: Results of $A_{TL'}$ in the elastic-threshold region. The top plot shows the measured $A_{TL'}$ as a function of ω in the elastic-threshold region. The data points are plotted together with the total uncertainties. The extraction scheme A and C [5] are plotted as solid and dotted lines. The elastic peak position (double line), the two-body breakup threshold (dashed line) and the three-body breakup threshold (dash-dotted line) are also shown. The bottom plot shows the experimental cross section vs. ω in the elastic-threshold region.

Chapter 7

Conclusion

Due to the lack of a free neutron target, the previously published data on the neutron magnetic form factor in the low Q^2 region come almost exclusively from electron-deuteron scattering experiments and thus potentially suffer from large model dependence. One feature about the previously published data is that the error bars are generally big. The most precise measurements on G_M^n at low Q^2 are the recent Bates [9] measurement, the NIKHEF/PSI data [10], and the Bonn data [11]. Unfortunately the NIKHEF measurement disagrees with the Bates measurement significantly at $Q^2 = 0.108$ $(\mathrm{GeV/c})^2$ and the Bonn measurement agrees with the Bates measurement at $Q^2 = 0.255$ $(\mathrm{GeV/c})^2$ barely within the uncertainties of the measurements. Our knowledge of the neutron magnetic form factor is rather poor in the low Q^2 region though it is much better than that of the neutron electric form factor.

The purpose of this thesis work was twofold. First, this work represented a completely new technique for measuring the neutron magnetic form factor at low Q^2, i.e., using spin-dependent electron scattering from a polarized ^{3}He target. The extracted ${G_M^n}^2$ value from this work at $Q^2 = 0.19$ $(\mathrm{GeV/c})^2$ agrees with the dipole parametrization value very well. The uncertainty of the extracted G_M^n value is dominated by the statistical uncertainty, and the uncertainty from model dependence has

been found to be comparatively small. Secondly, this was the second time that a polarized ^{3}He gas target using metastability exchange optical pumping technique was employed to measure the spin-dependent ^{3}He quasielastic asymmetry. The target performances (polarization, stability, robustness) have been improved significantly due to the implementation of the LNA laser together with various changes in the system (see Section 3.2). The target was operated a few degrees colder (13 K) than it was previously (17 K) which increased the target density by $\sim$ 30%. Using a Wien spin rotator, longitudinally polarized electrons were produced at the ^{3}He target using a single-pass beam. The polarized beam quality and beam current have also been improved significantly over that obtained in the previous experiment [6]. All the improvements mentioned above improved the statistics of this thesis work substantially. This still leaves room open for improving the statistics of the measurement, largely due to the fact that the metastability exchange optical pumping technique works only in the low pressure region. One can take two approaches to resolve this problem by either polarizing the ^{3}He gas using the metastability-exchange optical pumping technique and then increasing its density by compressing the polarized gas, or one can polarize the ^{3}He gas using spin-exchange with polarized alkali atoms which is a technique feasible for a higher pressure target.

The asymmetry results of $A_{TL'}$ in the elastic-threshold region also generate both theoretical and experimental interest. A more complete calculation using a spin-dependent spectral function with the final state interactions and meson exchange currents taken into account is probably necessary to interpret these data.

This experiment further demonstrates that polarized ^{3}He is very useful for studying the electromagnetic structure of the neutron and provides strong motivation to proceed with further experiments using polarized ^{3}He targets.

Appendix A

Cleaning the ^{3}He Target System

A.1 Copper Cell

The copper target cell must be cleaned chemically before attaching the copper foil windows to the cell and the cell to the glassware. Following is the procedure used for cleaning the copper cell.

1. Cleaning the copper cell first in warm Alconox solution to get rid of the grease. Scotch-brite pad is used for removing the grease off the copper surface.
2. Rinse the Alconox solution off the cell with water.
3. Dip the copper cell in diluted bright dip acid for 30-60 seconds. Make sure that the inner surface of the cell is totally immersed in the acid.
4. Remove the target cell from the acid. Dip it in a large container of distilled water to clean the acid off the surface.
5. Immerse the copper cell in acetone to remove the water.
6. Clean the surface with a soft tissue.

After being cleaned, the target cell was heated under vacuum in a bell jar to drive off the water. The cell was placed in the bell jar and the system roughed out; the cell was then heated to 120° C and maintained at this temperature under vacuum

(10^{-6} torr) for an hour. After the heating element was turned off, the bell jar was vented with dry nitrogen to atmosphere, and the copper cell was removed from the bell jar after it was cooled down to room temperature.

A.2 Glassware

The glassware was cleaned with alcohol first before the target cell was epoxied in place. The cleaning procedure involved baking the glassware under vacuum. Initially, the scattering chamber and the target system was pumped out using a roughing pump. Once the pressure of the system was low enough ($\leq$ 1 torr), the by-pass valve between the scattering chamber and the target system was closed and the target system was opened up to a turbo pump. The pumping cell was wrapped with heating tapes and the aluminum foils, and started baking once the vacuum was around 10^{-7} torr. The rest of the gas plumbing system was baked at the same time by wrapping heating tapes only around them. The pumping cell was heated to 300 - 400 °C, and care must be taken to avoid heating the part of the glassware close to the teflon valves too much. After baking for 36 - 48 hrs., the heating tapes wrapped around the rest of the gas plumbing system other than the pumping cell were turned off first, half an hour before turning off the heating of the glass pumping cell. A final vacuum of 5 - 8 $\times 10^{-8}$ torr was reached after the system cooled down to room temperature.

A.3 Mixing Bright Dip

Mix *in a fume hood* with proper protective wear (goggles, heavy gloves, etc.).

1. Place a beaker in an ice bath.
2. Add 20 m*l* distilled H_2O.

3. Add 120 ml 98 % H_2SO_4 slowly.
4. Add 60 ml 70 % HNO_3.
5. Cool to 0°C.
6. Add 1.7ml HCl *very slowly.*
7. Cool to 0°C.
8. Dilute to 10 × its volume before bright dipping.

Appendix B

^{3}He Quasielastic Asymmetry

The measured ^{3}He quasielastic transverse asymmetry $A_{T'}$ in the MEPS spectrometer are given in Table B.1. Corrections have been made with respect to the empty target background, the elastic radiative tail and the quasielastic radiative corrections. The asymmetries are given in terms of the positive target spin direction (R), negative target spin direction (L) and the combined data set (R+L).

Table B.2 lists the measured $A_{TL'}$ in the elastic-threshold region from the OHIPS spectrometer. The measured asymmetry numbers have been corrected with respect to the empty target background and the elastic radiative tail. The statistical and the systematic uncertainties are also listed. The systematic uncertainties were dominated by the uncertainties of the ^{3}He quasielastic yield, the beam polarization and the target polarization (see Section 6.4).

ω (MeV)	$A_{T'}$ (R) (%)	$A_{T'}$ (L) (%)	$A_{T'}$ (R+L) (%)
147.94	-12.38± 4.97	3.62 ± 6.46	-9.12 ± 3.94
136.60	-15.35 ± 3.18	11.67 ± 4.08	-13.97 ± 2.51
125.27	-11.36 ± 2.85	7.49 ± 3.67	-9.90 ± 2.25
113.93	-8.26 ± 2.80	6.06 ± 3.61	-7.44 ± 2.21
102.60	-9.05± 3.20	14.52 ± 4.12	-11.10 ± 2.52
91.26	-4.16± 6.44	20.77 ± 9.23	-9.61 ± 5.28

Table B.1: The ^{3}He quasielastic transverse asymmetry $A_{T'}$ measured from the present work as a function of electron energy loss ω. The measured asymmetry numbers have been normalized to $P_t = 100\%$, and $P_b = 100\%$. R stands for the positive target spin direction ($\theta^* = 8.9°$), L stands for the negative target spin direction ($\theta^* = 171.1°$), and R+L stands for the combined data set.

ω (MeV)	$A_{TL'}$ (%)	$\Delta A_{TL'}$ (%)	$\Delta A_{TL'}$ (%)
54.22	5.67	5.41	0.90
50.95	1.23	4.91	0.19
47.68	5.16	5.70	0.82
44.41	-7.93	6.63	1.25
41.14	3.62	8.14	0.57
37.86	31.10	10.30	4.92
34.59	-16.40	16.44	8.24
31.32	23.81	10.21	1.19
28.05	28.46	4.74	1.42

Table B.2: The ^{3}He quasielastic asymmetry $A_{TL'}$ measured from this work in the elastic-threshold region. The third column lists the statistical uncertainties and the last column lists the systematic uncertainties.

Bibliography

[1] T.W. Donnelly and A.S. Raskin, Ann. Phys. **169**, 247 (Academic Press, New York, 1986).

[2] B. Blankleider and R.M. Woloshyn, Phys. Rev. **C29**, 538 (1984).

[3] J.L. Friar *et al.*, Phys. Rev. **C42**, 2310 (1990).

[4] C. Ciofi degli Atti, E. Pace, and G. Salmè, Phys. Rev. **C46**, R1591 (1992).

[5] R.-W. Schulze and P.U. Sauer, Phys. Rev. **C48**, 38 (1993).

[6] C.E. Woodward *et al.*, Phys. Rev. Lett. **65**, 698 (1990).

[7] A.K. Thompson *et al.*, Phys. Rev. Lett. **68**, 2901 (1992).

[8] S. Galster *et al.*, Nucl. Phys. **B32**, 221 (1971).

[9] P. Markowitz *et al.*, Phys. Rev. **C48**, R5 (1993).

[10] J. Jourdan, *Contribution to the Workshop of Electron-Nucleus Scattering, Marciana Marina (Elba), July, 1993.*

[11] Hermann Reike, Preprint BONN-IR-93-72, Bonn University, December 1993.

[12] E.B. Hughes *et al.*, Phys. Rev. **139**, B458 (1965); *ibid.* **146**, 973 (1966).

[13] D. Braess and G. Kramer, Z. Phys. **189**, 242 (1966); D. Braess, D. Hasselmann and G. Kramer, Z. Phys. **198**, 527 (1967); D. Hasselmann and G. Kramer, DESY 67/21 (September 1967).

[14] B. Grossetête, S. Jullian, and P. Lehmann, Phys. Rev. **141**, 1435 (1966).

[15] K.M. Hanson *et al.*, Phys. Rev. **D8**, 753 (1973).

[16] R.J. Budnitz *et al.*, Phys. Rev. **173**, 1357 (1968).

[17] W. Bartel *et al.*, Phys. Lett. **30B**, 285 (1969); *ibid.* **39B**, 407 (1972); Nucl. Phys. **B58**, 429 (1973).

[18] P. Stein *et al.*, Phys. Rev. Lett. **16**, 592 (1966).

[19] G. Höhler *et al.*, Nucl. Phys. **B114**, 505 (1976).

[20] M. Gari and W. Krümpelmann, Z. Phys. **A322**, 689 (1985).

[21] H. Hajduk-Meier, Ch. Hajduk, P.U. Sauer, and W. Theis, Nucl. Phys. **A395**, 332 (1983).

[22] H. Hajduk-Meier, U. Oelfke and P.U. Sauer, Nucl. Phys. **A499**, 637 (1989).

[23] R.-W. Schulze, private communication.

[24] J.M. Laget, Phys. Lett. **B273**, 367 (1991).

[25] C. Ciofi degli Atti, E. Pace and G. Salmè, *Proceedings of the 6th Workshop on Perspectives in Nuclear Physics at Intermediate Energies*, ICTP, Trieste May 1993, (World Scientific); G. Salmè, private communication.

[26] S. Blatnik and N. Zovko, ACTA Phys. Austriaca **39**, 62 (1974).

[27] C.Y. Prescott *et al.*, Phys. Lett. **B77**, 347 (1978).

[28] J. Kessler, *Polarized Electrons*, 2nd ed., Springer Series on Atoms and Plasma, vol. 1 (Springer-verlag, New York, 1985).

[29] D.H. Beck, Ph.D. thesis, Massachusetts Institute of Technology (unpublished, 1986).

[30] J. Arrington *et al.*, Nucl. Instru. Meth. **A311**, 39 (1992).

[31] C. Møller, Ann. Phys. (Leipzig) **14**, 531 (1932).

[32] V.B. Berestetskii, E.M. Lifshitz and L.P. Pitaevskii. In *Quantum Electrodynamics*, Landau and Lifshitz course in Theoretical Physics, vol. 4, (Pergamon, Oxford, 1982).

[33] L.G. Levchuk, preprint, Kharkov Institute of Physics and Technology (Oct. 1992).

[34] B.W. Filippone, private communication.

[35] R.S. Turley, Ph.D. thesis, Massachusetts Institute of Technology (unpublished, 1984).

[36] C.S. Tripp, private communication.

[37] J. Nelson, Master's thesis, Massachusetts Institute of Technology (unpublished, March of 1986).

[38] MP-1 Group, *Introduction to Q*, LAMPF Document MP-1-3401-3 (1985).

[39] F.D. Colegrove, L.D. Shearer, and G.K. Walters, Phys. Rev. **132**, 2561 (1963).

[40] L.D. Shearer, Rev. Sci. Instrum. **32**, 1190 (1961).

[41] M. Onellion, M.W. Hart, F.B. Dunning, and G.K. Walters, Phys. Rev. Lett. **52**, 380 (1984).

[42] G.C. Philips, R.R. Perry, P.M. Windham, G.K. Walters, L.D. Shearer, and F.D. Colegrove, Phys. Rev. Lett, **9**, 502 (1962).

[43] S.D. Baker, E.B. Carter, D.O. Findley, L.L. Hatfield, G.C. Philips, N.D. Stockwell, and G.K. Walters, Phys. Rev. Lett. **20**, 738 (1968).

[44] *Workshop on Polarized ^3He Beams and Targets*, Princeton, N.J., 1984; AIP Conf. Proc. **131** (1985).

[45] C. Lhuillier and F. Laloe, J. Phys. (Paris) **41**, C7, 51 (1980).

[46] D.M. Hardy, S.D. Baker, and W.R. Boykin, Nucl. Instum. Meth. **98**, 141 (1972).

[47] C.E. Jones, Ph.D. thesis, Caltech, 1992 (unpublished).

[48] J.M. Daniels in *Workshop on Polarized ^3He Beams and Targets*, edited by R.W. Dunford and F.P. Calaprice (American Institute of Physics, New York, 1985), pp. 134-137.

[49] R.S. Timsit *et al.*, Can. J. Phys. **49**, 509 (1971).

[50] G. Eckert, W. Heil *et al.*, Nucl. Instr. Meth. **A320**, 53 (1992).

[51] M. Meyerhoff, Doctoral thesis, Mainz University (1994).

[52] M. Meyerhoff *et al.*, preprint (1993).

[53] K. Lee *et al.*, Phys. Rev. Lett. **70**, 738 (1993).

[54] D.S. Bett and M. Leduc, Ann. Phys. Fr. **11**, 267 (1986).

[55] T.R. Gentile and R.D. McKeown, Phys. Rev. **A47**, 456 (1993).

[56] P.J. Nacher and M. Leduc, J. Phys. **46**, 2057 (1985).

[57] F.D. Colegrove, L.D. Schearer, and G.K. Walters, Phys. Rev. **135**, A353 (1964).

[58] L. Schearer and M. Leduc, IEEE J. Quant. Electronics **QE22**, 756 (1986).

[59] C.L. Bohler *et al.*, J. Appl. Phys. **63**, 2497 (1988).

[60] L.D. Schearer, M. Leduc *et al.*, IEEE J. Quant. Electronics **QE22**, 713 (1986).

[61] J.M. Daniels, L.D. Schearer, M. Leduc, and P.J. Nacher, J. Opt. Soc. Am. **4** , 1133 (1987).

[62] H.H. Mc Adams, Phys. Rev. **170**, 276 (1968).

[63] W. Lorenzon, T.R. Gentile, H.Gao, and R.D. McKeown, Phys. Rev. **A47**, 468 (1993).

[64] C.G. Aminoff *et al.*, J. Lumin. **50**, 21 (1991).

[65] Werner Heil and Laird Schearer (private communications).

[66] C. Larat, Ph.D. thesis, L'Ecole Mormale Supérieure, 1991.

[67] M. Pinard and J. Van Der Linde, Can. J. Phys. **52**, 1615 (1974).

[68] N.P. Bigelow, P.J. Nacher, and M. Leduc, J. Phys. II France **2**, 2159 (1992).

[69] M. Santini, Suppl. Nuovo Cimento XVI-X, 680 (1960).

[70] F.J. Low and H.E. Rorschach, Phys. Rev. **120**, 1111 (1960).

[71] D. Pines and C.P. Slichter, Phys. Rev. **100**, 1014 (1955).

[72] C.P. Poole, Jr. and H.A. Farach, *Relaxation in Magnetic Resonance* (Academic, New York, 1971), p.74.

[73] H.H. Bukow, G. Heine, and M. Reinke, J. Phys. **B 10**, 2347 (1977).

[74] R.L. Brooks, V.F. Streif, and H.G. Berry, Nucl. Instrum. Methods **202**, 113 (1982).

[75] L.D. Schearer and G.K. Walters, Phys. Rev. **139**, A1398 (1965).

[76] R. Byerly, Jr., Ph.D. thesis, Rice University (unpublished, 1967).

[77] R.G. Milner, R.D. McKeown, and C.E. Woodward, Nucl. Instrum. Meth. **A257**, 286 (1987).

[78] K.D. Bonin, T.G. Walker, and W. Happer, Phys. Rev. **A37**, 3270 (1988).

[79] L.W. Mo and Y.S. Tsai, Rev. of Mod. Phy. **41**, 205 (1969).

[80] D.C. Carey, K.L. Brown and C. Iselin, *Decay TURTLE, A Computer Program For Simulating Charged Particle Beam Transport Systems, Including Decay Calculations*, SLAC-246, (March 1982).

[81] J.S. McCarthy, I. Sick, and R.R. Whitney, Phys. Rev. **C15**, 1396 (1977).

[82] G.B. West, Phys. Rep. **18C**, 264 (1975); R.D. McKeown, private communication.

[83] K. Dow *et al.*, Phys. Rev. Lett. **61**, 1706 (1988); K. Dow, MIT Ph.D. thesis (unpublished, 1987); K. Dow, private communication.

[84] P.C. Dunn *et al.*, Phys. Rev. **C27**, 71 (1983).

[85] J.-O. Hansen, private communication.

[86] F. Iachello *et al.*, Phys. Lett. **43B**, 191 (1973).